warwick.ac.uk/lib-publications

Quantitative and Holistic Views of Crystal Dissolution Processes

By

Maria Adobes Vidal

A thesis submitted for the degree of Doctor Philosophy

Department of Chemistry
April 2017

*A mi familia, especialmente a mis padres José Mª Adobes Sorando
y Mª Carmen Vidal Catalá, a quienes quiero con locura.*

Table of Contents

List of Figures

List of Tables

List of Abbreviations

Abbreviation	Meaning
API	Active pharmaceutical ingredient
AC	Alternating ion current
AFM	Atomic force microscopy
BM-SICM	Bias modulated scanning ion-conductance microscopy
BIC	Bicalutamide
BCS	Biopharmaceutics classification system
BFDH	Bravais-Friedel-Donnay-Harker
BCF	Burton-Cabrera-Frank
COM	Calcium oxalate monohydrate
CCDC	Cambridge crystallographic data center
CFMED	Channel flow method with electrochemical detection
CCD	Charge coupled device
COMPASS	Condensed-phase optimized molecular potentials for atomistic simulation studies
cvff	Consistent-valence force field
CM-AFM	Contact mode atomic force microscopy
DI	Deionized
DNA	Deoxyribonucleic acid
DC-SICM	Direct current scanning ion-conductance microscopy
DC	Direct ion current
DM-SICM	Distance modulated scanning ion-conductance microscopy
eq.	Equation
FEM	Finite element method
FPGA	Field programmable graphics array
LED	Light emitting diode
MUMPS	Multifrontal massively parallel sparse direct solver
NCM-AFM	Non-contact mode atomic force microscopy
OM	Optical microscopy
PDE	Partial differential equation
PBC	Periodic bond chain

QRCE	Quasi-reference counter electrode
ROI	Region of interest
SECCM	Scanning electrochemical cell microscopy
SECM	Scanning electrochemical microscopy
SICM	Scanning ion-conductance microscopy
SPM	Scanning probe microscopy
STM	Scanning tunneling microscopy
SAM	Self-Assembly monolayer
TM-AFM	Tapping mode atomic force microscopy
UME	Ultramicroelectrode
UV-Vis	Ultraviolet-visible
XRD	X-ray diffraction
1D	One-dimensional
2D	Two-dimensional
3D	Three-dimensional

List of Symbols

Symbol	Quantity
(hkl)	Miller indices
$(hkil)$	Miller indices in hexagonal systems
b	Burgers vector
d	Crystal largest dimension
c_i	Local concentration of species i
C, c	Concentration
C_{bulk}, c_0	Bulk concentration
C_{int}, C_{surf}	Concentration near the crystal-solution interface
C_{sat}	Saturation concentration
D	Diffusion coefficient
G	Gibbs free energy
J_i	Flux of species i
J_{MT}	Diffusive flux
J_{obs}	Overall dissolution flux
J_{SK}	Surface flux
k	Spring constant AFM cantilever
k_{diss}	Crystal dissolution rate constant
k_{growth}	Crystal growth rate constant
k_{int}, k_{surf}	Intrinsic dissolution rate constant
k_T	Transport rate constant
M	Molecular weight of the solvent
n	Reaction order
$\mathbf{n}$	Vector normal to the investigated surface
p	Pressure
r	Radial coordinate
r_{int}	Crystal radius
R	Reaction rate
t	Time
T	Temperature
t_{diff}	Diffusion time

V	Voltage
$\overline{V}$	Molar volume
v	Velocity vector
x	Spatial coordinate
δ	Diffusion boundary layer
ΔG	Change in Gibbs free energy
η	Dynamic viscosity of the solution
ρ	Density of the solution

Acknowledgements

First and foremost I would like to thank my supervisor Prof. Patrick Unwin for always believing in me and giving me the opportunity to form part of the Warwick Electrochemistry and Interfaces Group. His help, support, encouragement and enthusiasm throughout my PhD have been key to my success. Pat has constantly guided and supported me not only academically but also emotionally, even when he hated my silly ideas such as having a boxing fight for fundraising. I will never forget it, and I promise I will never do it again!

I also would like to thank Prof. Michael Ward and Dr. Alexander Shtukenberg for the amazing time I had in New York University working on the L-cystine project. They thought I was a bit crazy for studying crystal dissolution instead of growth but they always supported me and contributed enormously to the project with their immense knowledge and tough corrections of my manuscript. Besides them, I want thank my industrial advisors Dr. Leslie Hughes and Dr. Stephen Wren for their contribution to the studies of dissolution of APIs and for giving me the opportunity to get to know the world of the pharmaceutical industry.

I am forever thankful to Prof. Alison Rodger, the director of the CAS-IDP programme, for her mentorship and advice throughout all this time. I will always remember the joyful team activities and the amazing meetings she organized, which gave me the opportunity to be in Venice, the Shard or even on the top of the Volcano Etna. I am also thankful for the excellent example she has provided as a strong and successful female scientist and Professor.

I want to mention the past and present members of the Warwick Electrochemistry and Interfaces Group for providing such a great working environment, especially the *forever FYGs*, Emma Ravenhill, Faduma Maddar, Minkyung Kang, Sze-Yin Tan and Pollyana Castro for the coffee breaks, the endless talks about life and for all the fun we have had in the last four years that kept me sane. Your friendship is irreplaceable. In addition, thanks must go to Ashley Page and his Pagespeare skills for helping me in writing this thesis, free from a Spanish accent.

Declaration

The work presented in this thesis is entirely original and my own work, except where acknowledged in the text. I confirm that this thesis has not been submitted for a degree at another University. This work is being submitted for thesis by publications.

Chapter II

Maria Adobes-Vidal, Faduma M Maddar, Dmitry Momotenko, Leslie P Hughes, Stephen AC Wren, Laura N Poloni, Michael D Ward, Patrick R Unwin, Face-Discriminating Dissolution Kinetics of Furosemide Single Crystals: *In situ* Three-Dimensional Multi-Microscopy and Modeling, *Cryst. Growth Des*., **2016**, *16*, 4421-4429.

Chapter III

Faduma M. Maddar,[‡] Maria Adobes-Vidal,[‡] Leslie P. Hughes, Stephen A. C. Wren and Patrick R. Unwin, Dissolution of Bicalutamide Single Crystals in Aqueous Solution: Significance of Evolving Topography in Accelerating Face-Specific Kinetics, *Submitted as an article to Crystal Growth and Design.* [‡]These authors have contributed equally. Faduma M. Maddar performed the experiments and analyzed the AFM data and Maria Adobes-Vidal performed the FEM simulations and analyzed the kinetic regime of the dissolving crystal.

Chapter IV

Maria Adobes-Vidal, Alexander G Shtukenberg, Michael D Ward, Patrick R Unwin, Multiscale Visualization and Quantitative Analysis of L-Cystine Crystal Dissolution, *Cryst. Growth Des., * **2017**, *17*, 1766-1774.

Chapter V

Maria Adobes-Vidal, Harriet Pearce and Patrick R. Unwin, Tracking the Dissolution of Calcite Single Crystals in Acid Waters: A Simple Method for Measuring Fast Surface Kinetics, *Phys. Chem. Chem. Phys.* **2017***, 19,* 17827-17833. Some sections also feature in the MSc thesis of Harriet Pearce who jointly performed the experiments.

Additionally, I have also contributed to the following papers whose results are not presented in this thesis:

Amelia R Perry, Robert A Lazenby, <u>Maria Adobes-Vidal</u>, Massimo Peruffo, Kim McKelvey, Michael E Snowden, Patrick R Unwin, Hopping Intermittent Contact-Scanning Electrochemical Microscopy (HIC-SECM) as a New Local Dissolution Kinetic Probe: Application to Salicylic Acid Dissolution in Aqueous Solution, *CrystEngComm*, **2015**, *17*, 7835-7843.

Massimo Peruffo, Michael M Mbogoro, <u>Maria Adobes-Vidal,</u> Patrick R Unwin, Importance of Mass Transport and Spatially Heterogeneous Flux Processes for *In situ* Atomic Force Microscopy Measurements of Crystal Growth and Dissolution Kinetics, *J. Phys. Chem. C*, **2016**, *120*, 12100-12112.

Dmitry Momotenko, Ashley Page, <u>Maria Adobes-Vidal</u>, Patrick R Unwin Write–Read 3D Patterning with a Dual-Channel Nanopipette, *ACS Nano*, **2016**, *10*, 8871-8878.

Michael M. Mbogoro, Massimo Peruffo, <u>Maria Adobes-Vidal</u>, Emma L. Field, Michael A. O'Connell and Patrick R. Unwin, Quantitative 3D Visualization of the Growth of Individual Gypsum Microcrystals: Effect of Ca^{2+} : SO_4^{2-} Ratio on Kinetics and Crystal Morphology, *J. Phys. Chem. C,* **2017***, 121,* 12726–12734.

Abstract

This thesis is concerned with the development and application of novel theoretical and experimental methodologies to study crystal dissolution processes across multiple lengthscales. In particular, it presents a versatile *in situ* multimicroscopy approach, comprising atomic force microscopy (AFM), scanning ion-conductance microscopy (SICM), and optical microscopy (OM) that is readily combined with finite element method (FEM) simulations. The methodology permits the quantitative 3D visualization of microcrystal morphology during dissolution with well-defined, high mass transport rates, enabling both the measurement of face-dependent dissolution rates and the elucidation of the dissolution mechanism. The approach also allows the determination of interfacial concentrations and concentration gradients, as well as the separation of kinetic and mass transport limiting regimes. The high resolving power and versatility of this new methodology is demonstrated on four different crystalline compounds with very different characteristics.

First, the dissolution kinetics of individual faces of single furosemide microcrystals are investigated by OM-SICM and FEM modeling. It is found that the (001) face is strongly influenced by surface kinetics, while the (010) and (10$\bar{1}$) faces are dominated by mass transport. Dissolution rates are shown to vary greatly between crystals, with a strong dependence on crystal morphology and surface properties.

A similar approach is then used to investigate changes in both crystal morphology and surface processes during the dissolution of bicalutamide single crystals, achieving high resolution with *in situ* AFM. It is shown that dissolution involves roughening and pit formation on all dissolving surfaces, and that this has a strong influence on the overall dissolution rate. FEM simulations determine that mass transport contributions increase as dissolution proceeds due to a continuous increase of the intrinsic dissolution rate constant, promoted by the exposure of high index microfacets.

The methodology is further developed to show that kinetic data obtained from OM-SICM and AFM, which provide differing measures of kinetic parameters, are in good agreement when the different mass transport regimes of the two experimental configurations are accounted for. The robustness of the methodology is verified via studies of L-cystine crystals, while also providing insights into the dissolution mechanism by visualizing hexagonal spirals descending along screw dislocations.

Finally, the ability of the methodology to characterize processes with fast surface kinetics is demonstrated by the study of the proton-promoted dissolution of calcite single crystals. The approach allows the accurate determination of the near-interface concentration of all species during dissolution, as well as the intrinsic dissolution rate constant of the {104} faces, showing that surface kinetics play an important role in the dissolution process. Overall, this methodology provides a significant advance in the analysis and understanding of dissolution processes at a single crystal level, revealing the intrinsic properties of crystal faces and providing a powerful platform from which future studies can be developed.

Chapter I | Introduction

1.   Introduction to Crystals

1.1   Importance

The crystalline form is the most common state of solid matter on Earth,[1] defined by a regular arrangement of atoms, ions or molecules held together by covalent or non-covalent interactions. Bounded faces characterized by periodicity and anisotropy construct the crystal morphology, with the specific periodic structure at each face determining its fundamental physical and chemical properties. Crystalline materials appear in a diverse variety of systems, including elemental metals, rocks, pharmaceuticals, and even bones, playing a vital role in human lives.[1,2] Thus a fundamental understanding of crystal growth and dissolution processes is essential for advancing many areas of science and technology.[3,4]

In the pharmaceutical industry, crystallization is an important separation and purification method and often serves as the final step in the manufacture of active pharmaceutical ingredients (APIs). The resulting crystal form, shape and size influences many of the physicochemical properties of the API, such as stability, permeability and dissolution rate, which in turn affects the bioavailability of the drug. Consequently, significant time and effort is invested in the design of crystals with suitable dissolution rates that enhance dose-release properties and bioavailability whilst maintaining appropriate physical and chemical stability.[5-8] However, the pharmaceutical industry predominantly employs classical dissolution tests that stir crystal particles in a liquid and obtain the dissolution rate from changes in the chemical composition of the bulk solution as a function of time.[9,10] This approach allows the measurement of average rates of crystallization and dissolution, but cannot provide information about what specific relationship exists between the crystal form, shape, or size and the crystal reactivity; information crucial for crystal engineering in drug development.[4] In chapters II and III, this thesis introduces a novel approach to study the dissolution kinetics of single crystals of an API by directly visualizing the

evolution of crystal morphology in real time and in three dimensions. This method can be used to tailor crystal design to develop stable and efficient pharmaceutical products.

Crystalline materials are also widespread in biological systems. Teeth and bones are composed of inorganic crystals of hydroxyapatite (calcium phosphate, $Ca_{10}(PO_4)_6(OH)_2$),[11] and the main component of shells is calcium carbonate in the crystal forms aragonite or calcite.[12] These crystals grow in conjunction with proteins in a process known as biomineralization, and often exhibit intricate patterns that reflect complex mechanisms of formation.[13] Biominerals are optimally adapted to their function and possess unique combinations of mechanical properties such as stiffness, strength and toughness, while being lightweight, that scientists frequently attempt to replicate synthetically.[14] In contrast to these crystalline structures formed to maintain life, crystallization in biological systems can also be associated with various diseases. Cholesterol, for example, can crystallize in the arteries or within the gallbladder, leading to atherosclerotic plaques and gallstones respectively.[15,16] Gout is a consequence of the precipitation of needle-like crystals of monosodium urate on the articular cartilage of joints when the levels of uric acid in blood serum exceed the critical solubility level.[17] High levels of uric acid can also lead to crystals precipitating in the kidneys or bladder, forming uric acid kidney stones.[18] Another kind of kidney stones, the dissolution of which is studied in chapter IV, are L-cystine kidney stones, aggregates of hexagonal plates of L-cystine crystals caused by the genetic disorder cystinuria.[19] The increasing number of pathological crystals being identified has prompted the investigation of new therapeutic agents focused on inhibition and dissolution strategies to replace the inefficient existing treatments.[20-25]

Minerals are naturally occurring crystals of abiogenic origin. The majority of minerals are found in the Earth's crust, with their abundance and diversity controlled by the availability of their elemental components. The dissolution of minerals in water is a crucial process involved in many geochemical phenomena, including transport and sequestration of contaminants, soil fertility and rock porosity in both aquifers and oil reservoirs, and the global cycle of CO_2, influencing the chemical and physical characteristics of our landscape.[26] A quantitative description and understanding of these processes is imperative for earth and material scientists, and mineral dissolution

has been studied both in nature and in the lab for more than a century.[3,27] However, the complexity of geochemical processes and the inconsistencies in experimental results make difficult the establishment of reliable rate laws. Chapter V considers the dissolution of calcite crystals in acidic water, a process of great environmental and industrial significance, though one in which there are conflicting schools of thought about the kinetic regime.[28,29]

1.2 Fundamental Concepts

Single crystals are those without distortions in the structure or changes in the orientation of the crystal lattice throughout the whole crystal. Single crystals are characterized not only by the internal structure, but also by the external morphology and the perfection of the crystal faces that define it. The variety of single-crystal morphologies is demonstrated by dendritic snow crystals and polyhedral minerals, as well as sophisticated biominerals such as the spine of the sea urchin, described by a hierarchical structure of curved surfaces.[1,13] In this section, the fundamental concepts of polymorphism, external morphology, surface microtopography of crystal faces and lattice defects of single crystals are summarized.

1.2.1 Polymorphism

Numerous inorganic and organic compounds can crystallize into several crystal structures, known as polymorphs. Polymorphs are characterized by differences either in the packing of ions or molecules in the crystal lattice, or in the orientation or conformation of molecules at the lattice sites, producing a different X-ray diffraction pattern. Consequently, different polymorphs exhibit different physical and chemical properties such as thermodynamic stability, external morphology, melting point, and dissolution rates.[7,30] Only the most stable polymorph will remain over long periods of time; the others are defined as metastable polymorphs that will eventually transform into it. The Ostwald rule of stages describes that in general the polymorph that crystallizes first is the one which has the lowest energy barrier (least stable, highest energy, kinetically favorable) and that when polymorphic transformations occur, the transformation proceeds indirectly to the most stable phase via those of intermediate

stability.[31] Figure 1.1 shows a simple hypothetical free energy diagram of the thermodynamic and kinetic crystal transitions.
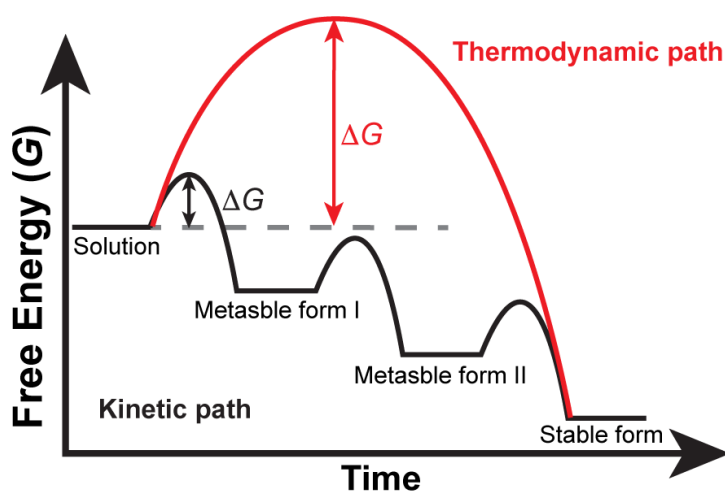
Figure 1.1. Illustration of the Ostwald rule of stages. The direct crystallization from solution to the stable form involves a large activation energy, ΔG, and may be very sluggish (thermodynamic path). Transformation via a sequence of steps (through metastable forms) involves smaller activation energies and may be kinetically more favorable.[32]

This phenomenon is of great industrial importance as different polymorphisms could severely affect the properties of the manufactured material. For example, polymorphism is very common in pharmaceutical compounds and may cause problems in the formulation, analysis and bioavailability of a compound, particularly when the drug is only sparingly soluble.[5,6] The API furosemide, for example, is a loop diuretic drug with low solubility and bioavailability. It exhibits three polymorphic forms[33] (Figure 1.2), but only the most stable polymorph (polymorph I) is present in the commercial drug.[34] The most stable polymorph usually has the lowest solubility and the slowest dissolution rate, leading to a lower bioavailability than the metastable polymorphs.[35]

Polymorph I
Triclinic P$\bar{1}$

Polymorph II
Monoclinic P2₁/n

Polymorph III
Triclinic P$\bar{1}$
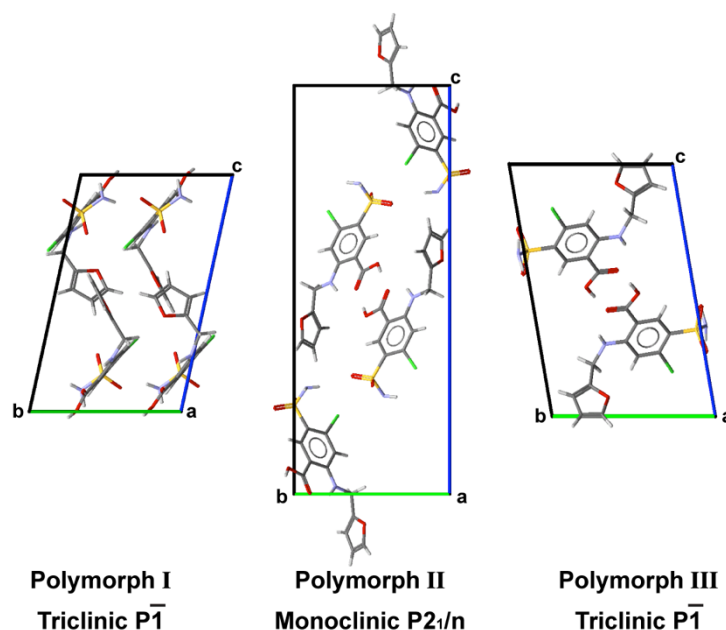
Figure 1.2. Unit cell molecular packing of the three polymorphs of the API furosemide obtained from the CCDC database.

1.2.2 Crystal Morphology

The crystal morphology, more commonly known as the crystal habit, describes the external shape of a crystal and the type of the crystallographic faces. Most organic and inorganic crystals exhibit polyhedral habits, in which faces (crystallographic faces determined by Miller indices (*hkl*)) are demarcated by edges. The final polyhedral shape is determined by the symmetry elements of the crystal group, the form and size of the unit cell, intermolecular bonds, and the density of lattice points per unit area, but most importantly, by the crystal growth conditions and the growth process.[1,36,37] Examples of two different crystal habits of furosemide polymorph I are shown in Figure 1.3.
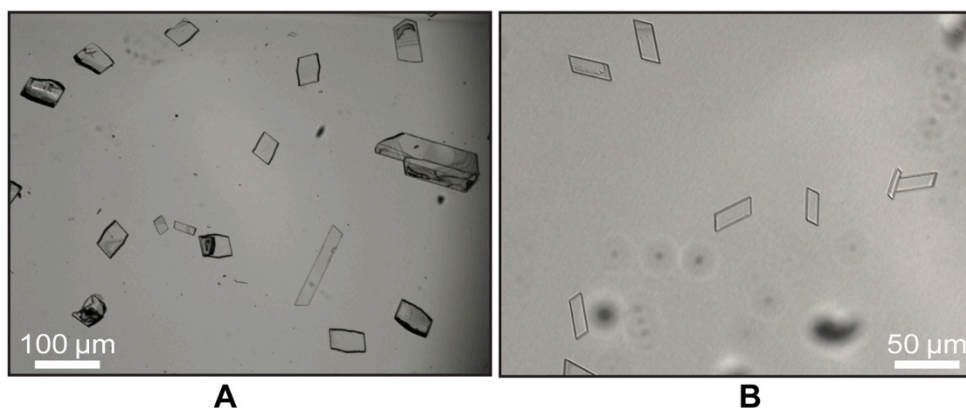
Figure 1.3. Optical micrographs of two different crystal habits of furosemide polymorph I. (a) Crystals grown in a methanol solution and (b) crystals grown in a water/ethanol mixture

Different crystallographic directions have different bonding properties that define and rule the character of the (*hkl*) faces. The crystal faces can be classified as flat (F), stepped (S) or kinked (K) depending on the number of strong interactions among molecules running uninterrupted along their plane, known as periodic bond chains (PBC). F faces contain more than one strong PBC running along their planes, S faces contain exactly one PBC and K faces do not contain any PBCs.[38] Consequently, different crystal faces have different molecular structures and surface free energies, affecting their interaction with both solute and solvent molecules and leading to different growth (and dissolution) rates at different faces. These differences are the basis for the establishment of the crystal habit. The faces with the slowest perpendicular growth rate are the largest (generally low Miller index (*hkl*) faces) and the most morphologically important, dominating the crystal habit.[38,39]

The surface properties of the crystal depend upon which crystal faces are exposed and the relative size of those faces. In turn, these surface properties influence material properties such as mechanical strength, agglomeration, bulk density, wettability and subsequent dissolution kinetics.[5] The crystal habit is also important from a technological point of view as it affects the efficiency of downstream processes such as filtering, washing, and drying, which all play a major role in the manufacture of crystalline materials,[40] and receives particular attention in the product and process design of pharmaceutical, agricultural, optoelectronic, catalytic and semiconductor constituents.[35,41,42]

6

Several methods for predicting crystal morphology based on crystal structure are used routinely to yield crystal morphologies consistent with experimental morphologies for a wide range of molecular crystals, despite a lack of consideration for the external growth environment.[43-45] These methods include (i) the Bravais−Friedel-Donnay−Harker (BFDH) method,[46-48] a geometric calculation based on crystal lattice and symmetry; (ii) the equilibrium method, based on the surface free energies of relevant crystal faces; and (iii) the growth (or "attachment energy") method, based on attachment energies corresponding to relevant crystal faces. Slightly different morphologies are often predicted by the different methods. Such discrepancies could be due to differences in the interpretation of molecular structure, bond anisotropies, and symmetry operators, as the influence of each factor varies from method to method.[45] The growth method (iii) is most effective when considering only the internal interactions of the crystal structure.[49,50] The method, developed by Hartmann and Perdok, uses the bond energy released when one building unit is attached to the surface of a crystal face to predict crystal morphology.[38,39] The growth rate normal to a particular face is proportional to the attachment energy for that surface; large attachment energies for a specific face correspond to strong out-of-plane intermolecular interactions, corresponding to faster growth normal to the plane and a lower morphological significance for the face.

One advantage of the studies presented in this thesis is the analysis of individual single crystals with a well-defined morphology using both experimental and computational methods. It becomes possible to measure face-specific dissolution kinetics that can be directly correlated with the surface chemical composition and molecular topography of the individual faces of the crystal habit and their particular interaction with the surrounding solvent molecules. This approach establishes a powerful method to quantitatively evaluate the dissolution properties of faceted crystals under certain conditions, with practical applications in the design of crystalline materials.

In addition, the surfaces of crystal faces generally exhibit stepped patterns or striations in certain crystallographic directions depending on the nature of the face. These features are directly related to the process of crystal growth and dissolution at the molecular level and the presence of defects in the crystal lattice. The

topographical features present on crystal faces are referred as the surface morphology or microtopography and receive special attention when studying dissolution processes.[27,28,51-53]

1.2.3 Crystal Defects and Surface Topography

Real single crystals are never perfect; the crystal lattice generally exhibits regions that show a discontinuity or distortion from the ideal alignment of units within the crystal, known as lattice defects. Lattice defects include: (i) point defects, such as vacancies, interstitial atoms and incorporated impurities; (ii) line defects, such as edge and screw dislocations; and (iii) surface defects, defined as surface microtopography. The number of defects depends on the growth rate of the crystal; the faster and more uncontrolled the growth, the greater the number of defects. Edge and screw dislocations are the most relevant kind of defects as they can significantly affect the thermodynamic and kinetic properties of a crystal. [51,52]

Edge dislocations can be described as a section of the crystal lattice in which the lower half has been stretched with respect to the upper half, causing the upper half to slip by a distance of one or more lattice units without losing adhesive force. *Screw dislocations* can be described as the displacement of a portion of the crystal lattice, creating a localized step on the surface that can propagate to form a helicoid structure. The *Burgers vector* of the dislocation, *b*, represents the magnitude and the direction of the lattice distortion. The Burgers vector of an edge dislocation is at right angles to the dislocation line, but that of a screw dislocation is parallel to the dislocation line.[27] A schematic representation of edge and screw dislocations in a simple cubic crystal lattice is shown in Figure 1.4.
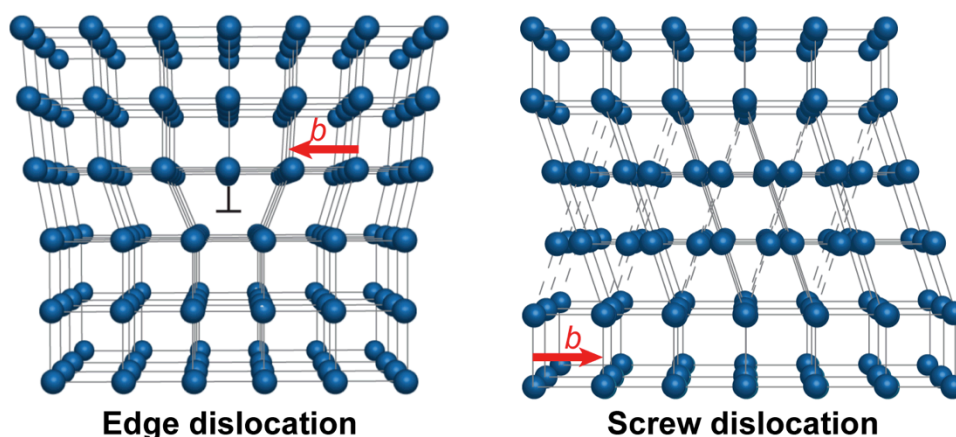
Figure 1.4. Schematic representation of edge and screw dislocations in a simple cubic crystal lattice. Red arrows depict the direction of the Burgers vector.

The presence of dislocations can affect both the kinetics and mechanism of crystal dissolution. Dislocations are thermodynamically unstable as the lattice plane around the dislocation line is distorted, introducing elastic strain energy into the crystal. This additional energy increases the free energy of the crystal above that of the defect-free state and reduces the activation energy for dissolution on the region of the surface around the dislocation core, allowing molecules to be easily removed from the surface to form a small hole. Once the hole is formed and reaches a critical size, the energy gained by the molecules going into bulk solution is higher than the increase in surface free energy from expanding the hole. Dissolution becomes thermodynamically favorable and etch pits are formed.[52,54] At the same time, when a screw dislocation is exposed to the crystal surface, it creates a step that will dissolve forming a large spiral staircase descending along the dislocation line. These spirals usually cover the entire crystal surface, providing a continuous source of steps for dissolution (*vide infra*). This dissolution mechanism is known as spiral dissolution and derives from the spiral growth mechanism of the theory described by Burton, Cabrera and Frank (BCF) in 1951.[55] Figure 1.5 illustrates both a hexagonal spiral hillock and a hexagonal spiral etch pit formed during the spiral growth and dissolution of the (0001) face of L-cystine single crystals.
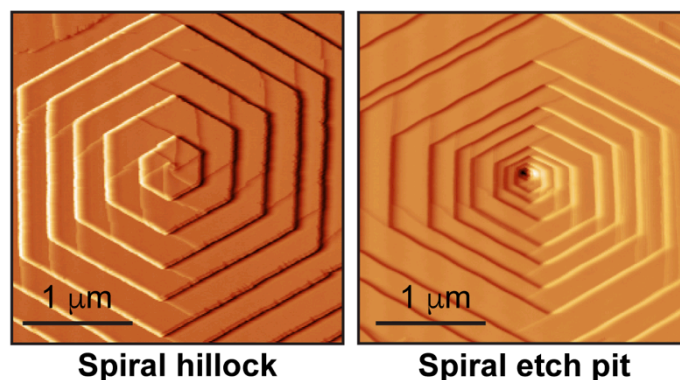
Figure 1.5. *In situ* atomic force microscopy (AFM) deflection images revealing the hexagonal spiral morphology of the (0001) face of L-cystine crystals during growth (spiral hillock) and dissolution (spiral etch pit). More information can be found in Chapter IV.

Crystal faces are also far from perfect; the surface microtopography consists of a set of steps, kink sites and vacancies separated by flat terraces.[56] A detailed representation of the microtopography of a simple cubic crystal lattice is shown in Figure 1.6. Detachment of molecules from the crystal surface during dissolution occurs preferentially from the most weakly bonded sites (high free energy sites). Steps, edges, dislocations and particularly kinks dissolve much more readily than flat surfaces. Each site contributes to the dissolution process in a different manner, and the overall kinetics and mechanism of the dissolution will depend on their relative abundance on the surface. Thus, many studies focus on visualizing changes in the crystal microtopography during dissolution in order to obtain insights into both the kinetics and the mechanism of the process.[52,57-62] Scanning probe microscopy (SPM) techniques are by far the most extensively used tools for imaging the dynamic processes occurring on crystal surfaces,[4] and thus the role of SPM techniques in the qualitative and quantitative analysis of crystal dissolution processes is reviewed in section 2 of this introduction.
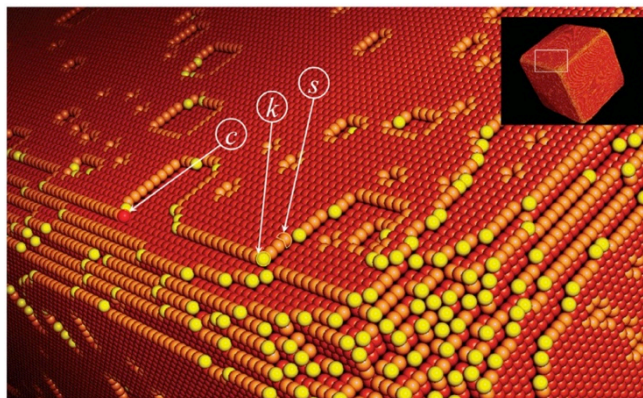
Figure 1.6 Detail of corner and monolayer pits of a 3-D Kossel-Stranski cubic crystal, showing terrace atoms in brown, step-edge (s) sites in tan, kink (k) sites in yellow, and 2-bonded chain atoms (c) in red. Reproduced with permission from reference 53. Copyright (2013) Mineralogical Society of America.

In general, dissolution occurs by the formation of etch pits and the retreat of steps on the crystal surface. The anisotropic morphology of the etch pits developed during dissolution, either from flat areas or dislocations, depends on several factors including the type of defect, symmetry of the crystal lattice, impurities, solvent, and driving force.[27,63,64] The formation of etch pits on the surface is generally accepted as an indication of surface processes controlling the dissolution regime, while smooth rounded surfaces result from dissolution being controlled by diffusion.[65] Figure 1.7 illustrates the etch pits formed on the (010) surface of acetaminophen single crystals after their partial dissolution in different solvents. It can be seen that the etch pits exhibit different morphologies depending on the solvent used.[63] Understanding the microtopographic changes of a crystal during dissolution and their effect on the dissolution kinetics is one of the main aims of this thesis.
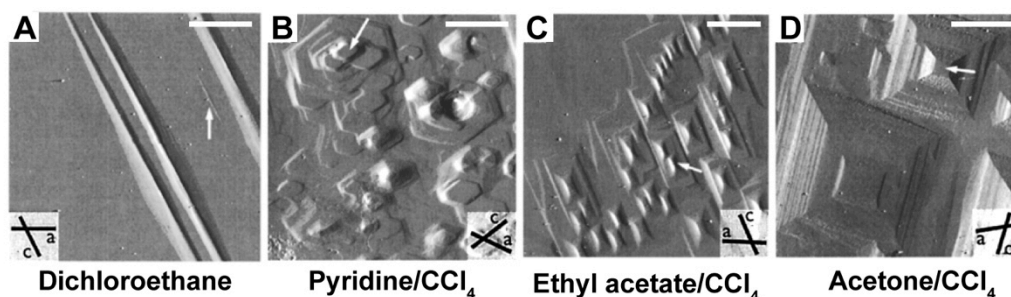
Figure 1.7. AFM images of the (010) face of acetaminophen single crystals dissolved in (a) dichloroethane, (b) pyridine/CCl_4, (c) ethyl acetate/CCl_4, and (d) acetone/CCl_4. The scale bar represents 15 μm. Adapted with permission from reference 62. Copyright (2000) American Chemical Society.

1.3   Dissolution of Crystals

Crystal dissolution is a complex reaction that involves several elementary events occurring in series. These events comprise (i) those occurring at the crystal surface, such as detachment of molecules from active sites, surface diffusion, and surface desorption; and (ii) the mass transport of detached solvated species away from the crystal to the undersaturated bulk solution. The slowest process will limit the overall dissolution rate and the dissolution kinetics can be described as *surface-kinetics-controlled* (mass transport comparatively fast), *mass-transport-controlled* (mass transport comparatively slow), or in a *mixed regime* (comparable surface and mass transport contributions). As such, it is necessary to differentiate surface processes from mass transport processes in order to determine which (if any) controls the rate of crystal dissolution. There is some experimental evidence that can be used to qualitatively interpret the dominant regime. For example, if the dissolution rate of a crystal stirred in a solution is independent of stirring rate, the process could be surface-kinetics-controlled because mass transport is strongly affected by convection. Another strategy is to monitor the morphology of the crystal; surface-kinetics-controlled dissolution rates are very sensitive to the surface properties as it reflects the energetics imposed by both the crystal structure and the surface microtopography. As a result, anisotropic dissolution and formation of etch pits can be observed. On the other hand, mass-transport-controlled processes are characterized by the formation of smooth spherical structures.[3] Additionally, under purely diffusion-controlled conditions, the radius of the resulting sphere depends on the square root of dissolution time as deduced from the solution of Fick's second law for spherical isotropic diffusion[3] (*vide infra*), which translates to an increase of dissolution rate over time. Thus, measurements of constant dissolution rates could be associated to surface-kinetics-controlled dissolution processes. However, these are extreme cases that are not always valid, since the overall dissolution rate is a complex combination of both the transport and the surface kinetics. Successful elucidation of the kinetic regime and the measurement of intrinsic dissolution rate constants requires that surface kinetics and mass transport contributions are quantified.[66]

The rate-limiting process (either mass transport or surface kinetics) typically occurs at a rate that allows the dissolution to be considered at steady state.[3] At steady state,

mass transport rates of reacting species diffusing away from the crystal surface are necessarily equal to the surface reaction rate. The concentration of species in the fluid near the crystal-solution interface will adjust itself until the rates are equal. This equality is always true, independent of the kinetic regime, but the concentration of species near the crystal-solution interface and concentration profiles will depend on whether diffusion or surface reactions control the dissolution process. In the case of slow surface kinetics, the concentration of species near the crystal-solution interface is close to that in bulk solution, and consequently the concentration gradient between the crystal surface and bulk solution is small (Figure 1.8a). On the other hand, when the surface kinetics are fast, the concentration of species near the crystal-solution interface will quickly approach the equilibrium concentration (saturation concentration), so that the concentration gradient is steeper (Figure 1.8c). In an intermediate situation, *i.e.* the kinetics are under mixed control, the near-interface concentration of species acquires an intermediate value (Figure 1.8b). In the subsequent sections, the phenomenological treatment of surface reaction and mass transport rates in terms of concentration of species is individually described.
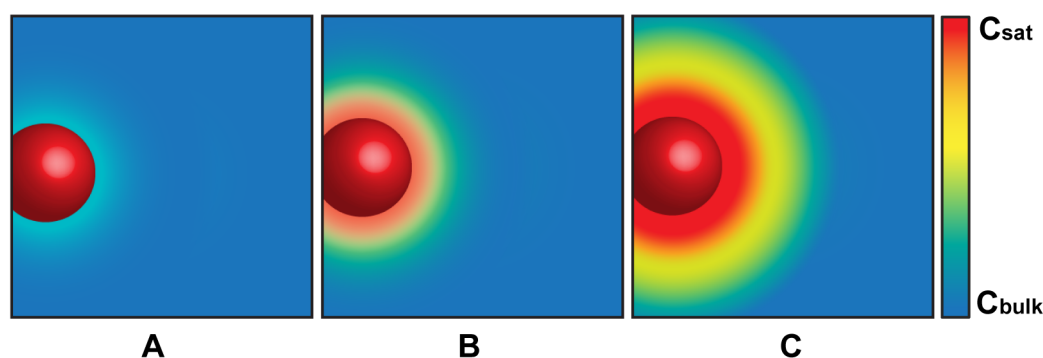
Figure 1.8. Schematic representation of steady state concentration profiles during crystal dissolution under (A) surface kinetics control, (B) mixed kinetics and (C) mass transport control regime.

1.3.1 Surface Reaction — Diffusion Theory

Surface processes occurring during the dissolution of a one component crystal (A) in aqueous solution can be treated as a heterogeneous reaction occurring at the crystal-solution interface that can be written as:

$$A_{(s)} \underset{k_{growth}}{\overset{k_{diss}}{\rightleftarrows}} A_{(aq)} \qquad (1.1)$$

where k_{diss} is the dissolution rate constant and k_{growth} is the rate constant for crystal growth. Dissolution occurs because there is a concentration difference between the crystal surface and bulk solution. The rate of surface reaction can be expressed as:

$$J_{SK} = k_{int} \left(C_{sat} - C_{int} \right)^n \qquad (1.2)$$

where J_{SK} represents the detachment rate of molecules from the surface, k_{int} is the intrinsic dissolution rate constant, which depends on the intrinsic characteristics of the crystal, C_{sat} is the concentration at the interface, C_{int} is the concentration near the crystal-solution interface and n is the order of the surface reaction. The order of the surface reaction with respect to the interfacial driving force (concentration gradient) depends on the mechanism of the reaction. BCF theory establishes that close to equilibrium conditions, $n = 2$, and that $n = 1$ for conditions far from equilibrium (high undersaturation).[55] For simplicity and because all the dissolution studies presented in this thesis have been done at sink conditions, we adopt $n = 1$. Once the molecules have detached from the crystal, they diffuse to bulk solution at a rate:

$$J_{MT} = k_T \left(C_{int} - C_{bulk} \right) \qquad (1.3)$$

where J_{MT} is the diffusive mass transport rate, k_T is the transport rate constant, which depends on the crystal size and the mass transport properties of the system (described in more detail in the next section) and C_{bulk} is the concentration in bulk solution. At the interface the concentration value is the saturation concentration, C_{sat}, because the solution in contact with the crystal is always in equilibrium with the solid. In the region near the interface, the concentration reaches a steady state, C_{int}, the value of which depends on the relative magnitude of k_{int} and k_T because at steady state:

$$J_{observed} = k_{int} \left(C_{sat} - C_{int} \right) = k_T \left(C_{int} - C_{bulk} \right) \qquad (1.4)$$

$$C_{int} = \frac{k_T C_{bulk} + k_{int} C_{sat}}{k_{int} + k_T} \qquad (1.5)$$

where $J_{observed}$ is the overall dissolution rate. When dissolution is surface-kinetics-controlled, $k_{int} << k_T$ and C_{int} is close to that in bulk solution ($C_{int} \approx C_{bulk}$):

$$C_{int} = \frac{k_T C_{bulk} + k_{int} C_{sat}}{k_{int} + k_T} \approx \frac{k_T C_{bulk} + k_{int} C_{sat}}{k_T} \approx C_{bulk} + \frac{k_{int} C_{sat}}{k_T} \approx C_{bulk}$$

(1.6)

and the overall dissolution rate measured is:

$$J_{observed} \approx J_{SK} = k_{int} \left(C_{sat} - C_{bulk} \right)$$

(1.7)

On the other hand, when dissolution is controlled by the diffusion of material away from the surface, $k_{int} >> k_T$ and C_{int} will quickly approach to the equilibrium concentration ($C_{int} \approx C_{sat}$):

$$C_{int} = \frac{k_T C_{bulk} + k_{int} C_{sat}}{k_{int} + k_T} \approx \frac{k_T C_{bulk} + k_{int} C_{sat}}{k_{int}} \approx \frac{k_T C_{bulk}}{k_{int}} + C_{sat} \approx C_{sat}$$

(1.8)

and the overall dissolution rate is:

$$J_{observed} \approx J_{MT} = k_T \left(C_{sat} - C_{bulk} \right)$$

(1.9)

When dissolution kinetics is under mixed control, $k_{int} \approx k_T$ and the overall dissolution rate is described by the equation:

$$J_{observed} = \frac{k_{int} k_T}{k_{int} + k_T} \left(C_{sat} - C_{bulk} \right) = k_{app} \left(C_{sat} - C_{bulk} \right)$$

(1.10)

where k_{app} is the apparent rate constant for dissolution.

1.3.2 Mass Transport

Assuming that the mass transport of species during crystal dissolution is governed exclusively by isotropic diffusion, the diffusion equation that describes the diffusive flux will depend on the crystal dimensions. For macroscopic crystals, semi-infinite linear diffusion propagates in one dimension perpendicular to the crystal surface (Figure 1.9a). In this case, the diffusion can be defined by Fick's second law, which for 1D is:

$$\frac{\partial C}{\partial t} = D\frac{\partial^2 C}{\partial x^2}$$

(1.11)

where C is the concentration of species, t depicts time, x denotes the distance measured perpendicular to the crystal surface and D is the diffusion coefficient. Solutions to the diffusion equation depend on both the initial and boundary conditions. For dissolution, where the initial concentration is $C = C_{bulk}$ for $x > 0$ and the boundary at $x = 0$ is maintained at C_{int}, thus the concentration profile of species follows:[67]

$$C(x,t) = C_{bulk} + (C_{int} - C_{bulk})erf\left(\frac{x}{2\sqrt{Dt}}\right)$$

(1.12)

indicating a continuous growth of the diffusion layer thickness with time. As the diffusion layer grows, the overall dissolution rate will slow down with time. The diffusive flux at the crystal surface is obtained from solution of Fick's first law, which for 1D gives:

$$J_{MT} = -D\left(\frac{\partial C}{\partial x}\right)_{x=0} = \frac{D}{\sqrt{\pi Dt}}(C_{int} - C_{bulk})$$

(1.13)
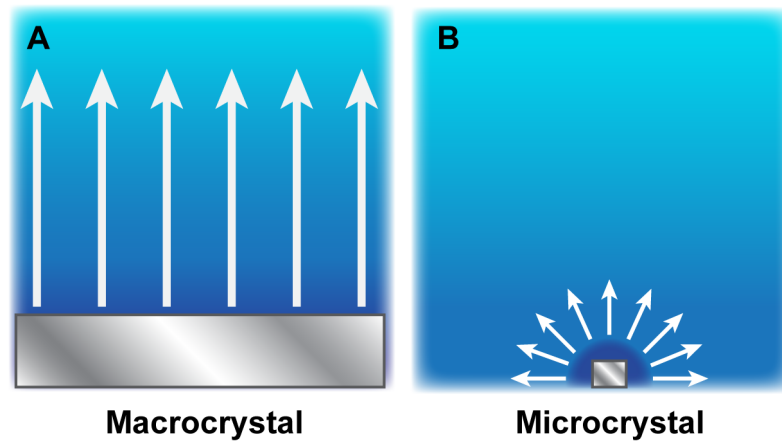
Figure 1.9. Schematic representation of (a) linear and (b) hemispherical diffusion of the crystal components during dissolution.

However, if the dissolving crystal is a few tens of micrometers in its largest dimension (*i.e.* a microcrystal), and the diffusion layer thickness becomes greater than that dimension, the diffusive flux changes drastically as the diffusion profile moves

from a linear profile to a well-defined spherical shape of finite size (Figure 1.9b).[68,69] If one considers the spherical diffusion equation and assumes that the establishment of steady state is faster than the time scale for a significant change in the crystal dimensions then:

$$\frac{\partial C}{\partial t} = D\left(\frac{\partial^2 C}{\partial r^2} + \frac{2}{r}\frac{\partial C}{\partial r}\right) = 0$$

(1.14)

where r is the radial distance. For the case in which the composition of the solution immediately adjacent to the surface of the dissolving crystal is fixed at some equilibrium value, C_{int}, then $C\ (r = r_{int}) = C_{int}$, and $C\ (r = \infty) = C_{bulk}$. Solving Fick's second law gives the concentration profile:

$$C(r) = C_{bulk} + \frac{r_{int}}{r}\left(C_{int} - C_{bulk}\right)$$

(1.15)

Solving Fick's first law gives the flux of crystal components diffusing away from the crystal surface in moles per unit area of the sphere per unit time (mol m^{-2} s^{-1}), described by:

$$J_{MT} = -D\left(\frac{\partial C}{\partial r}\right)_{r=r_{int}} = \frac{D}{r_{int}}\left(C_{int} - C_{bulk}\right)$$

(1.16)

Multiplying the flux by the molar volume of the crystal, $\overline{V}$, converts the flux to units of volume added per unit area of sphere per unit time, which is the displacement in the radius of the sphere, which in our case is the variation of the crystal size during dissolution:

$$\frac{dr_{int}}{dt} = \frac{D\overline{V}}{r_{int}}\left(C_{int} - C_{bulk}\right)$$

(1.17)

Integrating equation 1.17 provides the size of the crystal versus time:

$$r_{int} = -\sqrt{2D\overline{V}(C_{int} - C_{bulk})t}$$

(1.18)

This dependence of r_{int} on the square root of time is the typical parabolic behavior of a

kinetic process dominated by diffusion.[3]

Usually, in systems under forced convection (stirring or pumping the fluid), the section of the fluid near the crystal-solution interface has limited mobility. This restricts the ability of the fluid to maintain homogeneity by convection, and the main mode of mass transport through the stagnant liquid layer in contact with the solid becomes only diffusion. The stagnant layer is known as the *diffusion boundary layer, δ*, the structure of which is strongly dependent on the hydrodynamic conditions. The diffusive flux at the inner boundary of the layer becomes

$$J_{MT} = \frac{D}{\delta}\left(C_{int} - C_{bulk}\right) = k_T \left(C_{int} - C_{bulk}\right)$$

(1.19)

Equation 1.19 is the general expression for the mass transport rate in crystal dissolution. As highlighted above, pure mass-transport-controlled dissolution assumes that the surface kinetics are fast enough to ensure that the concentration of species in the solution immediately adjacent to the surface of the dissolving crystal is in equilibrium with the solid, such that $C_{int} = C_{sat}$, and the expression of the overall dissolution rate (measured) is:

$$J_{observed} = J_{MT} = k_T \left(C_{sat} - C_{bulk}\right)$$

(1.20)

In this thesis, overall dissolution rates of a variety of microcrystals are measured by a combination of near-field microscopy techniques including optical microscopy, scanning ion conductance microscopy and atomic force microscopy, such that the overall dissolution rate of the individual crystal faces exposed to the solvent can be obtained. The data permit the quantification of the contributions of diffusion and surface kinetics to the dissolution process via numerical simulations.

2. Scanning Probe Microscopy Techniques

Scanning probe microscopy (SPM) techniques have become an essential tool for the investigation of crystalline materials as they provide localized information about the physical and chemical characteristics of the surface at a resolution ranging from several 100 μm to individual atoms.[70] SPM has been used for the characterization of crystal surface energies, intermolecular interactions, aggregation and adhesion properties, as well as visualization of dislocations and topographical heterogeneities of crystallographic faces, local dissolution rates, and the intentional introduction of surface defects. The development of SPM techniques began with the scanning tunneling microscope (STM), invented by Binnig and Rohrer in 1982, in which a sharp metallic needle (probe) is scanned over an electrically conductive surface at a distance of less than 1 nm, creating a tunneling current between the tip and the surface when a bias voltage is applied. The tunneling current across the surface is then used by the feedback system to adjust the Z-position of the probe with piezoelectric positioners, keeping a constant tip-surface interaction. A record of the Z-position during a scan is then converted into a topographical image with tip-radius resolution by a computer system.[71] The operative principle of all SPMs is very similar; a physical probe scans a surface in a precise controlled manner at a very short surface-probe distance, reading the surface properties that depend on the nature of the probe-surface interaction. For example, electrical current, capacitance or force can be measured to build electrochemical and topographical images at a high resolution.[70] The resolution limit depends on the type and size of the probe. Each SPM requires the use of a specialized probe that can take many forms, including a tungsten wire with a single atom in the tip (atomic resolution),[72] a silicon nitride cantilever with a tip of a few nm radius,[73] ultramicroelectrodes (UMEs) of radius < 25 μm,[74] or borosilicate nanopipettes with one, two or four channels and an opening ranging from several nanometers to a few microns.[75] Figure 1.10 shows examples of different SPM probes.
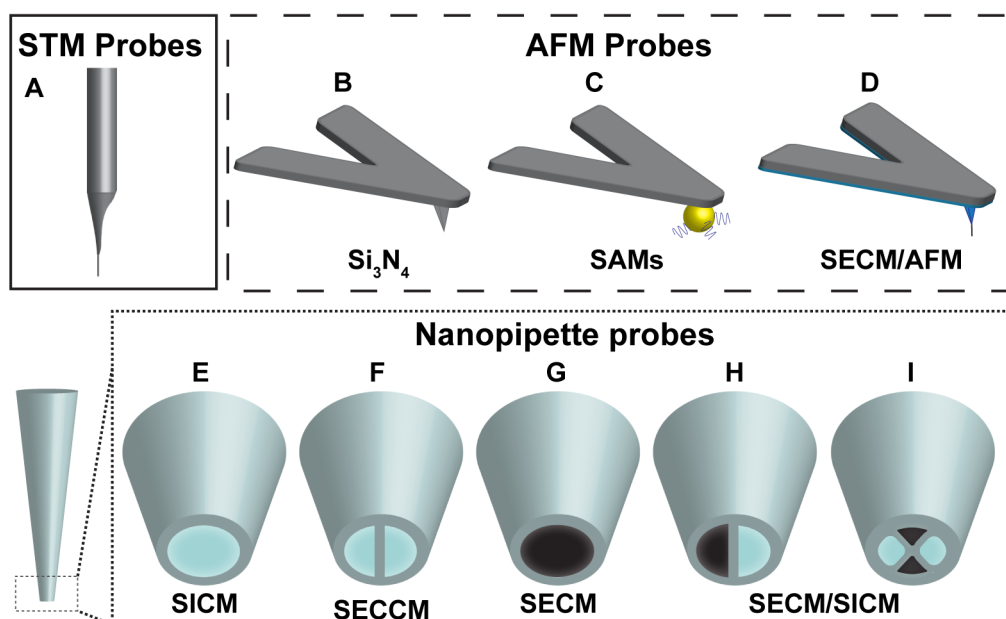
Figure 1.10. Examples of SPM probes. (A) Tungsten needle used in STM. (B) Typical silicon nitride AFM cantilever used for topographical imaging. (C) Gold-coated AFM tip functionalized with self-assembled monolayers (SAMs) for characterization of the physicochemical properties of the sample. (D) Silicon nitride cantilever with a platinum electrode at the end of the tip for electrochemical and topographical imaging (SECM-AFM). (E) Typical one-barrel nanopipette probe used in SICM. (F) Double-barrel nanopipette probe used in SECCM. (G) Ultramicroelectrode used in SECM. (H) Double-barrel nanopipette probe where one barrel is filled with pyrolitic carbon and the other with electrolyte solution for simultaneous SECM-SICM. (I) Quad-barrel nanopipette probe for simultaneous SECM-SECCM.

In the field of crystal dissolution, atomic force microscopy (AFM) and electrochemical probe microscopy (SEPM) represent powerful tools for the direct *in situ* visualization of the dynamic processes occurring at the crystal-solution interface. For instance, scanning electrochemical microscopy (SECM) employs an amperometric or potentiometric UME as scanning probe to induce and monitor dissolution from a specific region of the crystal surface. This approach permits the quantitative measurement of interfacial fluxes associated with specific features of the interface, enabling the construction of three-dimensional maps of the local surface kinetics and topography of the crystal surface. SECM has been used to characterize very fast surface kinetics of highly soluble ionic single crystals,[76-78] dissolution of biominerals,[79] and acid-induced dissolution reactions among others.[80-82] However, the spatial resolution of SECM is comparable to the diameter of the UME used, typically several micrometers.

In order to improve spatial resolution, the hybrid SECM-AFM technique was developed using electroactive AFM tips.[83] The tip functions as an electrode as well as a high-resolution topographical sensor. This approach has been used to monitor the surface processes from cleaved single crystals under electrochemical control, and to observe the first real-time *in situ* operation of the spiral dissolution mechanism described by BCF theory.[55,60] Point defects, etch pits, variations in the dissolution mechanism[84] and corrosion of metals have been also characterized by SECM-AFM.[84-87] The most critical aspect of this technique is the design and development of reliable probes, as the analytical functionality is directly integrated into the AFM tip and mounting and establishing a suitable electrical contact has proven to be challenging.[88]

Another powerful combination of individual SPM techniques to generate high-resolution topographical images with complementary chemical information is SECM-scanning ion microscopy (SECM-SICM). SECM-SICM probes consist of a double-channel nanopipette in which one barrel is filled with electrolyte and is open to the bulk solution and the other is equipped with an electrode for SECM detection. These probes have been employed for simultaneous interfacial pH and topography mapping of calcite microcrystals during dissolution in aqueous solution, also determining the dissolution kinetics.[89] A clear advantage of this technique is that nanopipette-based probes are made easily, quickly, and cheaply with reproducible, tunable characteristics.[75,90]

Nanopipette-based probes can also be used for the introduction of localized dissolution features on a crystal surface without immersing the crystal in solution.[91,92] For example, double-channel nanopipettes filled with electrolyte solution used in a scanning droplet cell regime known as scanning electrochemical cell microscopy (SECCM)[93] have been used to measure rapid dissolution kinetics of NaCl crystals in pure water via meniscus contact.[91] The acid-induced process of dental enamel dissolution and the effect of various protective treatments has also been studied by SECCM.[92] This technique permits multiple and rapid measurements (sub-millisecond resolution) of the conductance current across a crystal surface that is sensitive to the interfacial flux of ions, enabling the elucidation of the intrinsic dissolution rate constant. However, it does not allow the simultaneous characterization of the induced features at the crystal surface, failing to provide mechanistic information of the dissolution process.

SICM and AFM are the most widely used and versatile SPM techniques for *in situ* topography-functional mapping.[94-96] Fast imaging,[94] high spatial resolution[97] and extensive environmental versatility[98] are some of the advantages of these techniques. Despite this, no articles have been found in the literature describing the study of crystal dissolution by means of SICM alone, whereas crystal dissolution studies by AFM are abundant.[99-104]

2.1 Scanning Ion Conductance Microscopy

2.1.1 Principles

A single-channel nanopipette (typically 10's nm opening) filled with electrolyte and equipped with a Ag/AgCl quasi-reference counter electrode (QRCE) is approached towards a surface in a bath of electrolyte solution containing a second QRCE. Then, an ion current is generated between both electrodes when a bias voltage is applied. The magnitude of the ion current is sensitive to the probe-surface distance, the nature of the surface and the voltage applied between both QRCEs, changing from the bulk value when the probe-surface distance is less than one tip diameter.[105-107] This change in the ion current is used as the feedback signal to detect the surface, such that topographical and functional maps can be obtained without establishing physical probe-surface contact.[94,95,108,109]

2.1.2 Feedback Types and Scanning Modes

SICM can operate in various modes that use different feedback signals to probe a surface. SICM feedback modes include: (i) *direct current* (DC) mode,[105] in which a constant bias is applied between both QRCEs. The ion current decreases rapidly as a function of probe-surface distance as a result of the increased resistance in the region at the end of the nanopipette. This current drop is used as a feedback signal. (ii) *Distance modulation* (DM) mode,[110] which involves vertically oscillating the probe whilst applying a fixed bias, generating an alternating current (AC) signal upon approach to the surface. The AC signal is more stable than the DC signal and can be described by both its amplitude and phase angle component, with respect to the applied oscillation of the voltage. In this mode, an increase in the AC amplitude is used as feedback. (iii)

Bias modulation (BM) mode,[111] in which a harmonically oscillating bias between both QRCEs is applied to induce an AC signal. In this case, both a decrease in the AC amplitude and an increase in the AC phase can be used for feedback. A schematic illustration of the different feedback types used in SICM is shown in Figure 1.11. BM-SICM was first demonstrated relatively recent and has several advantages over the traditional DC-SICM and DM-SICM modes that make it more suitable for multifunctional imaging.[75,94,111]
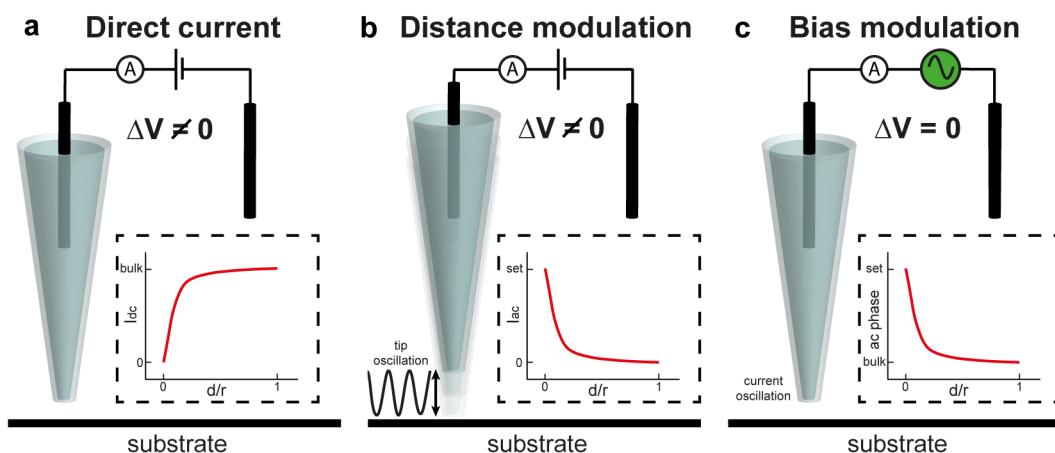
Figure 1.11 Comparison between different modes of SICM feedback. (a) Direct current mode in which the surface is detected via a drop in ionic current. (b) Distance modulation mode, in which the probe is oscillated in the vertical direction to produce an AC signal at small tip–substrate separation. (c) Bias modulation mode, in which a sinusoidal bias is applied between the two electrodes and the AC phase is monitored for feedback. Illustrative approach curves are shown in the insets on the images, revealing the feedback response as a function of the relative probe-to-substrate distance d/r (physical probe–substrate separation, d, and probe opening radius, r). In b and c, "set" indicates a set-point value for a particular quantity that is used to stop the tip moving closer to the surface and can be used for feedback during imaging. Reproduced with permission from reference 72. Copyright (2016) American Chemical Society.

SICM maps can also be acquired using different scanning modes. *Constant distance* and *hopping mode* are the most commonly used in SICM imaging. In constant distance mode, a constant DC or AC signal is maintained by a feedback loop that moves the probe vertically while it scans laterally.[105,112] By maintaining a constant DC or AC signal, a constant probe-surface distance is maintained and a topographical image is formed by tracking the *Z*-position throughout the scan (Figure 1.12a). Although constant distance mode has proven useful for a wide range of applications, it is difficult to image complex surface features of high aspect ratio.[113]

On the other hand, hopping mode consist of a series of approach curves to determine the surface topography. The probe approaches the surface to a certain probe-surface distance determined by the value of the DC or AC feedback threshold and the *Z*-position is recorded.[114] Then, the probe is withdrawn and moved to a new location before starting a new approach (Figure 1.12b). The number of data points and the retraction distance determines the image resolution and the imaging time. Generally, constant distance enables faster scan rates than hopping mode, but hopping mode allows high-resolution imaging of more complex features.
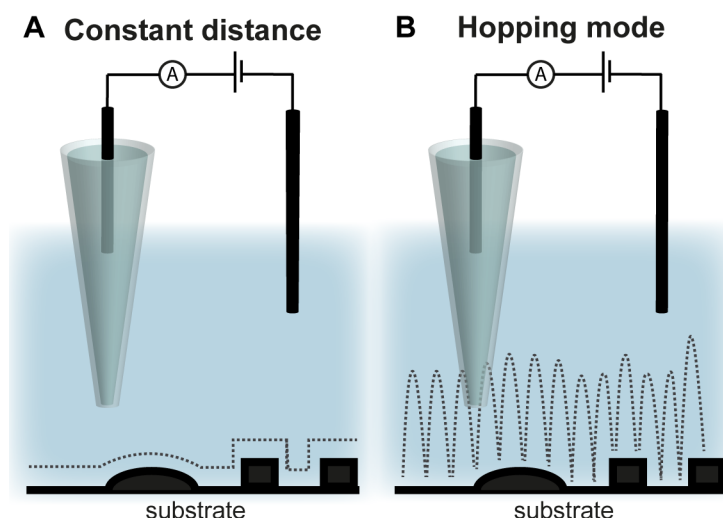
Figure 1.12. Trajectory of the SICM probe during (a) a constant distance scan and (b) a hopping mode scan.

2.1.3 Applications

Since SICM was introduced in 1989 by Hansma *et al.,*[105] it has been used primarily in molecular biology and materials science for high resolution topographical imaging of soft samples such as living cells.[113-115] An important aspect of this technique is that allows the characterization of mechanical responses or morphological transformations of cells caused by external stimuli.[110] SICM is sensitive to local heterogeneities in the ionic atmosphere, and has been used to study the transport properties of ion channels in cells and porous membranes via conductance measurements.[116] Moreover, the nanopipette probe has been used as a delivery system to introduce materials to localized areas of a substrate such as DNA[117] and fluorescent dyes[118] for further analysis.

In the last five years, the technique has gone beyond these applications as a result of a better understanding of the ion flux processes and electric effects that constitute the current response,[106,107,119] enabling the simultaneous topographical and functional analysis of surfaces.[95] This new capability has been used to establish relationships between surface structure and surface charge in cells[108,109] and obtain topography-reactivity maps of UMEs.[94]

Although it has not been practically applied to the crystal growth and dissolution field, only one study has been found in the literature,[89] there are significant prospects for this technique to constitute a suitable tool for the investigation of the mechanism and kinetics of crystal dissolution. SICM constitutes a powerful means of probing dynamic processes at interfaces, particularly when correlating changes in the local ion concentration with variations in the surface topography.

2.2. Atomic Force Microscopy

2.2.1 Principles

In AFM, a sharp tip (from a few nm to tens of nm radius), typically composed of silicon, is mounted on the end of a flexible silicon nitride cantilever, characterized by a distinct spring constant k, and scanned in a raster pattern across a defined area of a surface in either an air or a fluid environment. When the tip is brought into close proximity of the surface (below 10 nm), attractive and repulsive forces between the tip and the surface lead to the deflection of the cantilever. A laser beam reflected from the back of the cantilever into a position sensitive photodiode detector measures the cantilever deflection.[120] Depending on the imaging mode, either the cantilever deflection or the oscillation amplitude or frequency is used as the feedback signal to keep a constant tip-surface force, with the Z-position of the tip adjusting to maintain the feedback. The vertical movements of the tip trace the local height of the sample, which is plotted against the tip position in the XY-plane to create three-dimensional topographical maps at sub-nanometer resolution. A schematic of the major components of an AFM is shown in Figure 1.13a.
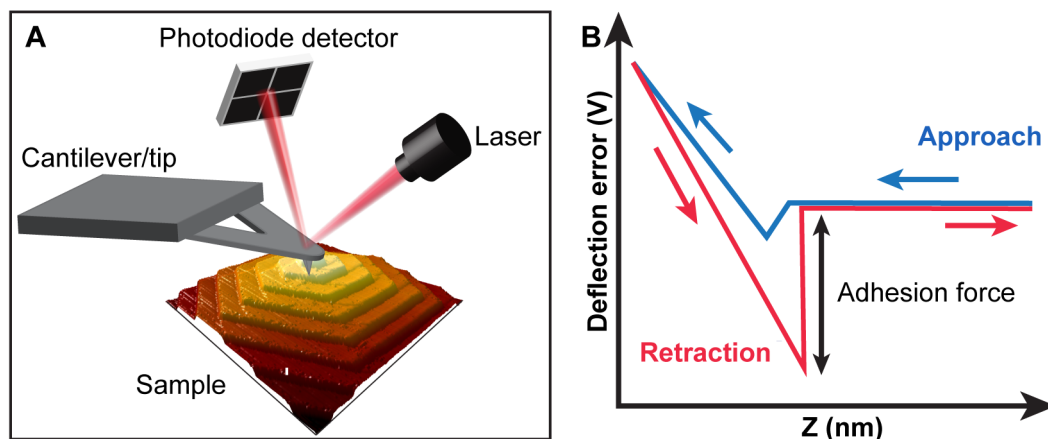
Figure 1.13. (A) Schematic of the AFM detection method. A laser is reflected from the back of the cantilever into a position sensitive photodiode detector, measuring the cantilever deflection. (B) Force curves obtained upon approach (blue line) and retraction (red line) of a cantilever from the sample surface. The appearance of the force curves (slope and deflection distance) provides an insight into the nature of the tip-surface interaction.

In addition to topographical imaging, AFM can also be used to investigate local chemical and mechanical properties of surfaces, such as elasticity and adhesion, by quantifying the force felt by the cantilever as a function of the tip-surface distance.[121] A force curve plots the deflection of the cantilever as the tip is extended toward the surface (approach curve) and retracted from the surface (retraction curve) as shown in Figure 1.13b. The hysteresis between the two force curves is due to adhesive forces arising from the contact of the tip with the surface, only noticeable during retraction. The appearance of the force curves (slope and deflection distance) provides an insight into the nature of the tip-surface interaction. Furthermore, the AFM tip can be chemically modified with molecules or biomolecules to investigate interactions between specific functional groups and the surface of interest.[122] The force between the tip and the surface (F) can be calculated according to Hooke's law (eq 1.21), where d is the measured deflection displacement.

$$F = -kd \qquad (1.21)$$

2.2.2 Feedback Types and Scanning Modes

There are three main modes of AFM imaging: (i) *contact mode* (CM), in which the tip is brought into continuous contact with the surface. The feedback system maintains a constant cantilever deflection (deflection set point), adjusting the height of the cantilever relative to the surface, which is then translated into a topographical map.

However, usually it is not possible to have the feedback signal responding instantaneously, and the deflection of the cantilever will actually vary during imaging. The amount it varies depends on the topography of the sample (higher in the regions with a great range of slope with distance) and the imaging parameters. The deflection signal represents the error signal, namely, how much the cantilever is deflecting before the deflection is corrected by the feedback system via height adjustment by the piezoelectric positioner. Generally, the AFM software can display the deflection signal as an image, with opposite contrast on regions of changing slope. Deflection images are commonly used, as it chapter IV, to provide a more photorealistic image of the sample since it shows the shape of the sample, but at the expense of height information.[121] (ii) *Tapping mode* (TM), in which the cantilever oscillates near the surface at its resonant frequency, establishing intermittent tip-surface contact. The feedback system maintains a constant amplitude of oscillation (amplitude set point) to report topographical information. (iii) *Non-contact mode* (NCM), in which the tip does not contact the surface. The cantilever oscillates at its resonant frequency, which is affected by the van der Waals and capillary forces within a 10 nm tip-surface separation. The feedback system maintains a constant oscillation amplitude or frequency (frequency set point) adjusting the average tip-surface distance.

CM-AFM is advantageous in that it is the easiest mode to operate, as the feedback is directly controlling the tip-surface interaction force, and it allows faster scan rates than TM-AFM and NCM-AFM. However, the lateral shear forces exerted by the tip on the surface can be quite high, resulting in mechanical damage, making it sometimes unsuitable for imaging soft surfaces (*e.g.* biomolecular crystals).[123] This is particularly problematic when imaging in air because van der Waals and capillary forces between the tip and the surface enhance attractive interactions, which aggravates mechanical damaging.[124] On the other hand, TM-AFM and NCM-AFM minimize the lateral force applied to the surface while preserving high lateral resolution (limited by the tip curvature). When imaging under solution, CM-AFM offers superior resolution as the solution eliminates capillary forces and reduces tip-surface forces, reducing any mechanical damage of the surface.[124] Thus, *in situ* CM-AFM studies of biological samples and crystal growth and dissolution processes are abundant.[4,124-126]

2.2.3 Applications

The applications of AFM span numerous disciplines including chemistry, physics, biology, materials science, and nanotechnology. The flexibility of AFM as a tool to image, probe and manipulate materials makes it one of the most widely used instruments for the characterization of surface properties and visualization of dynamic interfacial processes.[127-130] Consequently, AFM has proven very useful for the characterization of crystal interfaces and the investigation of crystal growth and dissolution processes.[124,125,129,131] For example, AFM has been used for the real time *in situ* visualization of growth and dissolution spirals developing from screw dislocations,[60,132] and for the elucidation of crystal structures when X-ray diffraction is not accessible via the identification of lattice parameters of biomolecular crystals in air and liquid environments.[133,134]

Both, the kinetics and the mechanism of crystal growth have been extensively investigated by *in situ* AFM.[135-139] Visualization of polygonal growth hillocks from dislocations and steps dynamics as a function of the solution supersaturation under surface-kinetics-controlled conditions enabled the determination of step edge free energies, and free energy barriers for nucleation.[140] It has also allowed near molecular-scale identification of the growth events occurring at specific crystallographic planes in the presence of additives, such that the growth mechanism and individual molecular recognition events can be deduced.[140,141] TM-AFM has been used to study the growth mechanism of different protein polymorphs and obtain insights into the origin of crystal defects.[123] Investigating the inhibition and control of crystal growth by additives or tailor-made auxiliaries using AFM has been an active area of research. Crystal habit modifications,[36,141-143] polymorphism selectivity,[37] and growth inhibition[21] could lead to the design of crystalline materials with specific functionality, a key aspect in a diversity of fields, such as geology, biomineralization, catalysis and pharmaceuticals.

On the other hand, despite its industrial and environmental importance, crystal dissolution has received relatively little attention. Examples of the most relevant AFM studies on crystal dissolution over the last two decades include: (i) the visualization of etching patterns resulting from different solvent-crystal interactions by *ex situ* CM-AFM;[63] (ii) the determination of kinetic and thermodynamic models of the dissolution process of minerals by *in situ* AFM;[144-150] and (iii) the comparison of the dissolution

rates of two different facets of aspirin crystals by measuring retreating step velocities using *in situ* AFM.[103] Additionally, dissolution mechanisms and the effect of surface adsorbates on the process have also been investigated by *in situ* CM-AFM.[98,100,151]

However, as with any imaging technique, AFM suffers from certain limitations. Tip-surface interactions can promote crystal dissolution (and growth), creating defects on the crystal surface and affecting the measurement of the intrinsic dissolution kinetics and the determination of the dissolution mechanism. The presence and the movement of the cantilever can disturb the diffusion boundary layer developed at the crystal interface, creating interfacial concentration heterogeneities across the surface, which in turns affects the dissolution kinetics. This is particularly problematic when the crystal dissolves in either the diffusion-controlled or mixed regime.[152] A solution to this problem is to force convection, by creating a laminar flow through a fluid cell; at a rate high enough to induce surface-kinetics-controlled dissolution, which is generally assumed when step velocities are independent of flow rate. However, some authors have demonstrated that this assumption is inadequate, as diffusion effects under the cantilever (*i.e.* the formation of a diffusion boundary layer) cannot be completely eliminated. Thus, a detailed analysis of the hydrodynamics and mass transport inside the cell is necessary for the correct determination of the crystal dissolution kinetics.[102,152,153]

A second drawback is that the maximum scan area for most AFMs is approximately 120×120 μm, but when imaging dynamic processes the scan area is generally reduced to $1 \times 1 - 5 \times 5$ μm. This small region of investigation may not be representative of the overall surface and important information about the interface during dissolution may be lost. For *in situ* measurements, the lateral scan rate and thus the image acquisition rate recording fast step velocities is challenging, and *in situ* AFM remains limited to reasonably slow dissolution processes.

3. Finite Element Method Modeling

With multiple variables (crystal geometry, hydrodynamics, temperature, chemical reactions, experimental setup, etc.) influencing overall dissolution rates, it becomes almost impossible to obtain insights into the kinetics and mechanism of dissolution from experimental data alone. Thus, mathematical modeling of chemical and physical phenomena is a fundamental tool for the analysis and quantification of dissolution processes. In this thesis, finite element method (FEM) modeling is used to solve the partial differential equations (PDEs) that describe mass transport processes during crystal dissolution from a phenomenological point of view (*vide supra*). FEM modeling is a numerical procedure for obtaining approximate solutions (by transforming PDEs in ordinary differential equations) with high accuracy. To solve the problem, the domain in which the numerical problem is formulated is discretized into a finite number of small regions called elements and approximated as an assembly of them. Tuning the convergence parameters allows approximations of arbitrary precision, even on geometrically complicated boundaries.[154]

A typical FEM model first involves defining the geometry that best describes the experimental system. The model geometry can be defined in one, two or three dimensions, with the higher dimensions requiring more computational effort. Despite this, through this thesis, only three-dimensional simulations are used due to the anisotropy of crystal dissolution systems. The crystal size and morphology determined experimentally are replicated in the model. Additionally, when studying dissolution in an AFM environment (chapter IV), the exact geometry and dimensions of the flow cell and components such as the AFM cantilever and tip are also simulated in order to investigate the fluid hydrodynamics and the influence of the components on the mass transport of species during dissolution. The physicochemical properties of the system such as number of species, chemical reactions occurring in bulk solution, diffusion coefficients or equilibrium constants are also defined. Finally, in order to solve the PDEs, the initial and boundary conditions must be specified, including the initial concentration and flux of individual species (overall dissolution rate measured experimentally). For steady-state problems, the model sets initial conditions as a first approximation and then estimates subsequent solutions until the calculated error is below the desired threshold.

The model simulates mass transport by diffusion and convection based on Fick's second law of diffusion, implementing the mass balance equation:

$$\frac{\partial C}{\partial t} + \mathbf{v} \cdot \nabla C = \nabla \left(D \nabla C \right) + R \tag{1.22}$$

where C is the concentration of species, t depicts time, $\mathbf{u}$ is the velocity vector, D denotes the diffusion coefficient, and R is a reaction rate expression for the species. $\mathbf{u}$ can be calculated by solving the PDEs that describe fluid flow, namely the momentum balance (eq 1.23) and continuity (eq. 1.24) Navier-Stokes equations for an incompressible fluid using a FEM model.

$$\rho \mathbf{v} \cdot \nabla \mathbf{v} = \eta \nabla^2 \mathbf{v} - \nabla p \tag{1.23}$$

$$\rho \nabla \mathbf{v} = 0 \tag{1.24}$$

where ρ and η are the solution density and dynamic viscosity respectively, and p is the pressure. Using the above equations, the model calculates the concentration of species around the dissolving crystal, most importantly near the crystal-solution interface, as C_{int} provides an insight into the kinetic regime of dissolution and allows the calculation of the intrinsic dissolution rate constant.

4. Thesis Aims

The main aim of this thesis is to develop new theoretical and experimental methodologies for the study of crystal dissolution across multiple lengthscales in order to obtain quantitative information about the relationship between crystal surface structure and reactivity, the role of mass transport, the influence of interfacial solute concentration on both the kinetics and mechanism of dissolution, and changes in the dissolution kinetics attributed to changes in crystal morphology. Each chapter is self-contained and based on submitted or published articles in scientific journals.

Chapter II focuses on the development of a multimicroscopy approach in which SICM and optical microscopy are combined with FEM simulations to study the dissolution kinetics of individual faces of furosemide single microcrystals. The dissolution rate and

the kinetic regime are obtained for all crystal faces that are exposed to the solvent, and related to the chemical composition and molecular topography of the surface.

Chapter III highlights the importance of understanding the crystal surface characteristics and the surface processes accompanying crystal dissolution when studying dissolution kinetics. The visualization of both the morphological and topographical changes during the dissolution of bicalutamide single microcrystals via *in situ* AFM, and the incorporation of experimental data into FEM models, reveal that surface effects can impact the dissolution kinetics, increasing the mass transport contribution to the overall dissolution rate.

Chapter IV directly compares *in situ* nanoscale and macroscale measurements to obtain insights into the mechanism and kinetics of the dissolution of hexagonal L-cystine single crystals. Experimental results from both OM-SICM and AFM are used to produce detailed FEM simulations that examine mass transport in both setups. Simulations demonstrate an essential link between microscopic and macroscopic behavior, as measured by *in situ* AFM and OM-SICM, respectively.

Chapter V further explores the capabilities of the methodology by studying fast dissolution kinetics. It is shown that the approach introduced in this thesis also permits the determination of the intrinsic dissolution rate constant of very fast surface processes such as the proton-promoted dissolution of rhombohedral calcite, demonstrating that surface kinetics play an important role in the dissolution of microcrystals.

Finally, chapter VI considers the significant contributions of this thesis to the field of crystal dissolution in the form of concluding remarks.

5. References

1.   Sunagawa, I. *Crystals*; Cambridge University Press, 2005.

2.   Poloni, L. N.; Ward, M. D. *Chem. Mater.* **2014**, *26*, 477-495.

3.   Lasaga, A. C. *Kinetic Theory in the Earth Sciences*; Princeton University Press, 1998.

4.   Unwin, P. R.; Macpherson, J. V. *Chem. Soc. Rev.* **1995**, *24*, 109-119.

5.   Blagden, N.; de Matas, M.; Gavan, P. T.; York, P. *Adv. Drug Delivery Rev.* **2007**, *59*, 617-630.

6.   Hörter, D.; Dressman, J. B. *Adv. Drug Delivery Rev.* **2001**, *46*, 75-87.

7.   Chen, J.; Sarma, B.; Evans, J. M. B.; Myerson, A. S. *Cryst. Growth Des.* **2011**, *11*, 887-895.

8.   Fridgeirsdottir, G. A.; Harris, R.; Fischer, P. M.; Roberts, C. J. *J. Pharm. Sci.*, *105*, 2260-2269.

9.   Dokoumetzidis, A.; Macheras, P. *Int. J. Pharm.* **2006**, *321*, 1-11.

10.   Siepmann, J.; Siepmann, F. *Int. J. Pharm.* **2013**, *453*, 12-24.

11.   Dorozhkin, S. V.; Epple, M. *Angew. Chem., Int. Ed.* **2002**, *41*, 3130-3146.

12.   Falini, G.; Albeck, S.; Weiner, S.; Addadi, L. *Science* **1996**, *271*, 67.

13.   Weiner, S.; Addadi, L. *Annu. Rev. Mater. Res.* **2011**, *41*, 21-40.

14.   Wegst, U. G. K.; Bai, H.; Saiz, E.; Tomsia, A. P.; Ritchie, R. O. *Nat Mater* **2015**, *14*, 23-36.

15.   Gollish, S. H.; Burnstein, M. J.; Ilson, R. G.; Petrunka, C. N.; Strasberg, S. M. *Gut* **1983**, *24*, 836-844.

16.   Duewell, P.; Kono, H.; Rayner, K. J.; Sirois, C. M.; Vladimer, G.; Bauernfeind, F. G.; Abela, G. S.; Franchi, L.; Nunez, G.; Schnurr, M.; Espevik, T.; Lien, E.; Fitzgerald, K. A.; Rock, K. L.; Moore, K. J.; Wright, S. D.; Hornung, V.; Latz, E. *Nature* **2010**, *464*, 1357-1361.

17.   Martinon, F.; Petrilli, V.; Mayor, A.; Tardivel, A.; Tschopp, J. *Nature* **2006**, *440*, 237-241.

18.   Sours, R. E.; Zellelow, A. Z.; Swift, J. A. *J. Phys. Chem. B* **2005**, *109*, 9989-9995.

19.   Ahmed, K.; Dasgupta, P.; Khan, M. S. *Postgrad. Med. J.* **2006**, *82*, 799-801.

20.   Rimer, J. D.; An, Z.; Zhu, Z.; Lee, M. H.; Goldfarb, D. S.; Wesson, J. A.; Ward, M. D. *Science* **2010**, *330*, 337-341.

21. Hu, L.; Yang, Y.; Aloysius, H.; Albanyan, H.; Yang, M.; Liang, J.-J.; Yu, A.; Shtukenberg, A.; Poloni, L. N.; Kholodovych, V.; Tischfield, J. A.; Goldfarb, D. S.; Ward, M. D.; Sahota, A. *J. Med. Chem.* **2016**, *59*, 7293-7298.

22. Shtukenberg, A. G.; Poloni, L. N.; Zhu, Z.; An, Z.; Bhandari, M.; Song, P.; Rohl, A. L.; Kahr, B.; Ward, M. D. *Cryst. Growth Des.* **2015**, *15*, 921-934.

23. Sahota, A.; Parihar, J. S.; Capaccione, K. M.; Yang, M.; Noll, K.; Gordon, D.; Reimer, D.; Yang, I.; Buckley, B. T.; Polunas, M.; Reuhl, K. R.; Lewis, M. R.; Ward, M. D.; Goldfarb, D. S.; Tischfield, J. A. *Urology* **2014**, *84*, 1249.e1249-1249.e1215.

24. Chung, J.; Granja, I.; Taylor, M. G.; Mpourmpakis, G.; Asplin, J. R.; Rimer, J. D. *Nature* **2016**, *536*, 446-450.

25. Abendan, R. S.; Swift, J. A. *Cryst. Growth Des.* **2005**, *5*, 2146-2153.

26. Brantley, S. L.; Kibicki, J. D.; White, A. F. *Kinetics of Water-rock Interaction*; Springer Science: New York, US, 2008.

27. Sangwal, K. *Etching of Crystals: Theory, experiment, and application*; North-Holland Amsterdam: Amsterdam, NL, 1987; Vol. 497.

28. Compton, R. G.; Unwin, P. R. *Philos. Trans. R. Soc., A* **1990**, *330*, 1-45.

29. Colombani, J. *J. Phys. Chem. Lett.* **2016**, *7*, 2376-2380.

30. Perkins, M. C.; Bunker, M.; James, J.; Rigby-Singleton, S.; Ledru, J.; Madden-Smith, C.; Luk, S.; Patel, N.; Roberts, C. J. *Eur. J. Pharm. Sci.* **2009**, *38*, 1-8.

31. Ostwald, W. *Z. Phys. Chem* **1897**, *22*, 289-330.

32. Putnis, A. *An introduction to mineral sciences*; Cambridge University Press, 1992.

33. Babu, N. J.; Cherukuvada, S.; Thakuria, R.; Nangia, A. *Cryst. Growth Des.* **2010**, *10*, 1979-1989.

34. Goud, N. R.; Gangavaram, S.; Suresh, K.; Pal, S.; Manjunatha, S. G.; Nambiar, S.; Nangia, A. *J. Pharm. Sci.* **2012**, *101*, 664-680.

35. Florence, A. T.; Attwood, D. *Physicochemical principles of pharmacy*; Pharmaceutical Press, 2011.

36. Thompson, C.; Davies, M. C.; Roberts, C. J.; Tendler, S. J. B.; Wilkinson, M. J. *Int. J. Pharm.* **2004**, *280*, 137-150.

37. Weissbuch, I.; Popovitz-Biro, R.; Lahav, M.; Leiserowitz, L.; Rehovot. *Acta Crystallogr., Sect. B: Struct. Crystallogr. Cryst. Chem.* **1995**, *51*, 115-148.

38. Hartman, P.; Perdok, W. G. *Acta Crystallogr.* **1955**, *8*, 49-52.

39. Hartman, P.; Perdok, W. G. *Acta Crystallogr.* **1955**, *8*, 521-524.

40. Snyder, R. C.; Doherty, M. F. *AIChE J.* **2007**, *53*, 1337-1348.

41. Lovette, M. A.; Browning, A. R.; Griffin, D. W.; Sizemore, J. P.; Snyder, R. C.; Doherty, M. F. *Ind. Eng. Chem. Res.* **2008**, *47*, 9812-9833.

42. Massaro, F. R.; Moret, M.; Bruno, M.; Aquilano, D. *Cryst. Growth Des.* **2013**, *13*, 1334-1341.

43. Docherty, R.; Clydesdale, G.; Roberts, K. J.; Bennema, P. *J. Phys. D: Appl. Phys.* **1991**, *24*, 89.

44. Hod, I.; Mastai, Y.; Medina, D. D. *CrystEngComm* **2011**, *13*, 502-509.

45. Punzo, F. *Cryst. Growth Des.* **2011**, *11*, 3512-3521.

46. Bravais, A. *Etudes Crystallographiques*, 1913.

47. Friedel, G. *Bull. Soc. Fr. Mineral.* **1907**, *30*, 326.

48. Donnay, J. D. H.; Harker, D. *Am. Mineral.* **1937**, *22*, 463.

49. Berkovitch-Yellin, Z. *J. Am. Chem. Soc.* **1985**, *107*, 8239.

50. Hartman, P.; Bennema, P. *J. Cryst. Growth* **1980**, *49*, 145.

51. Burt, H. M.; Mitchell, A. G. *Int. J. Pharm.* **1981**, *9*, 137-152.

52. Blum, A. E.; Yund, R. A.; Lasaga, A. C. *Geochim. Cosmochim. Acta* **1990**, *54*, 283-297.

53. Lasaga, A. C.; Luttge, A. *Science* **2001**, *291*, 2400-2404.

54. Frank, F. C. *J. Cryst. Growth* **1981**, *51*, 367-368.

55. Burton, W. K.; Cabrera, N.; Frank, F. C. *Philos. Trans. R. Soc., A* **1951**, *243*, 299-358.

56. Lüttge, A.; Arvidson, R. S.; Fischer, C. *Elements* **2013**, *9*, 183-188.

57. Beig, M. S.; Lüttge, A. *Geochim. Cosmochim. Acta* **2006**, *70*, 1402-1420.

58. Tang, R.; Nancollas, G. H.; Orme, C. A. *J. Am. Chem. Soc.* **2001**, *123*, 5437-5443.

59. Wang, Y.; Zhang, H.; Han, Y.; Liu, P.; Yao, X.; Zhao, H. *Chem. Commun.* **2011**, *47*, 2829-2831.

60. Macpherson, J. V.; Unwin, P. R.; Hillier, A. C.; Bard, A. J. *J. Am. Chem. Soc.* **1996**, *118*, 6445-6452.

61. Spruzeniece, L.; Piazolo, S.; Maynard-Casely, H. E. *Nature Communications* **2017**, *8*, 14032.

62. Clark, J. N.; Ihli, J.; Schenk, A. S.; Kim, Y.-Y.; Kulak, A. N.; Campbell, J. M.; Nisbet, G.; Meldrum, F. C.; Robinson, I. K. *Nat Mater* **2015**, *14*, 780-784.

63. Li, T.; Morris, K. R.; Park, K. *J. Phys. Chem. B* **2000**, *104*, 2019-2032.

64. Godinho, J. R. A.; Stack, A. G. *Cryst. Growth Des.* **2015**, *15*, 2064-2071.

65. MacInnis, I. N.; Brantley, S. L. *Geochim. Cosmochim. Acta* **1992**, *56*, 1113-1126.

66. Colombani, J. *Geochim. Cosmochim. Acta* **2008**, *72*, 5634-5640.

67. Lasaga, A. C. *J. Geophys. Res.: Solid Earth* **1984**, *89*, 4009-4025.

68. Bard, A. J.; Faulkner, L. R.; Leddy, J.; Zoski, C. G. *Electrochemical methods: fundamentals and applications*; wiley New York, 1980; Vol. 2.

69. Heinze, J. *Angew Chem Int Ed Engl* **1991**, *30*, 170-171.

70. Meyer, E.; Hug, H. J.; Bennewitz, R. *Scanning probe microscopy: the lab on a tip*; Springer Science & Business Media, 2013.

71. Binnig, G.; Rohrer, H.; Gerber, C.; Weibel, E. *Phys. Rev. Lett.* **1982**, *49*, 57-61.

72. Oliva, A.; Romero G, A.; Pena, J.; Anguiano, E.; Aguilar, M. *Rev. Sci. Instrum.* **1996**, *67*, 1917-1921.

73. Zhong, Q.; Inniss, D.; Kjoller, K.; Elings, V. *Surf. Sci.* **1993**, *290*, L688-L692.

74. Mirkin, M. V.; Horrocks, B. R. *Anal. Chim. Acta* **2000**, *406*, 119-146.

75. Kang, M.; Momotenko, D.; Page, A.; Perry, D.; Unwin, P. R. *Langmuir* **2016**, *32*, 7993-8008.

76. Macpherson, J. V.; Unwin, P. R. *J. Phys. Chem.* **1994**, *98*, 1704-1713.

77. Macpherson, J. V.; Unwin, P. R. *J. Phys. Chem.* **1994**, *98*, 11764-11770.

78. Macpherson, J. V.; Unwin, P. R. *J. Phys. Chem.* **1995**, *99*, 3338-3351.

79. Etienne, M.; Schulte, A.; Mann, S.; Jordan, G.; Dietzel, I. D.; Schuhmann, W. *Anal. Chem.* **2004**, *76*, 3682-3688.

80. Perry, A. R.; Lazenby, R. A.; Adobes-Vidal, M.; Peruffo, M.; McKelvey, K.; Snowden, M. E.; Unwin, P. R. *CrystEngComm* **2015**, *17*, 7835-7843.

81. McGeouch, C.-A.; Peruffo, M.; Edwards, M. A.; Bindley, L. A.; Lazenby, R. A.; Mbogoro, M. M.; McKelvey, K.; Unwin, P. R. *J. Phys. Chem. C* **2012**, *116*, 14892-14899.

82. McGeouch, C.-A.; Edwards, M. A.; Mbogoro, M. M.; Parkinson, C.; Unwin, P. R. *Anal. Chem.* **2010**, *82*, 9322-9328.

83. Macpherson, J. V.; Unwin, P. R. *Anal. Chem.* **2000**, *72*, 276-285.

84. Jones, C. E.; Unwin, P. R.; Macpherson, J. V. *ChemPhysChem* **2003**, *4*, 139-146.

85. Jones, C. E.; Macpherson, J. V.; Unwin, P. R. *J. Phys. Chem. B* **2000**, *104*, 2351-2359.

86. Izquierdo, J.; Eifert, A.; Souto, R. M.; Kranz, C. *Electrochem. Commun.* **2015**, *51*, 15-18.

87. Izquierdo, J.; Fernández-Pérez, B. M.; Eifert, A.; Souto, R. M.; Kranz, C. *Electrochim. Acta* **2016**, *201*, 320-332.

88. Kranz, C. *Analyst* **2014**, *139*, 336-352.

89. Nadappuram, B. P.; McKelvey, K.; Al Botros, R.; Colburn, A. W.; Unwin, P. R. *Anal. Chem.* **2013**, *85*, 8070-8074.

90. Perry, D.; Momotenko, D.; Lazenby, R. A.; Kang, M.; Unwin, P. R. *Anal. Chem.* **2016**, *88*, 5523-5530.

91. Kinnear, S. L.; McKelvey, K.; Snowden, M. E.; Peruffo, M.; Colburn, A. W.; Unwin, P. R. *Langmuir* **2013**, *29*, 15565-15572.

92. Parker, A. S.; Al Botros, R.; Kinnear, S. L.; Snowden, M. E.; McKelvey, K.; Ashcroft, A. T.; Carvell, M.; Joiner, A.; Peruffo, M.; Philpotts, C.; Unwin, P. R. *J. Colloid Interface Sci.* **2016**, *476*, 94-102.

93. Ebejer, N.; Schnippering, M.; Colburn, A. W.; Edwards, M. A.; Unwin, P. R. *Anal. Chem.* **2010**, *82*, 9141-9145.

94. Momotenko, D.; McKelvey, K.; Kang, M.; Meloni, G. N.; Unwin, P. R. *Anal. Chem.* **2016**, *88*, 2838-2846.

95. Perry, D.; Al Botros, R.; Momotenko, D.; Kinnear, S. L.; Unwin, P. R. *ACS Nano* **2015**, *9*, 7266-7276.

96. Ozgur, S.; Natalia, E. *Nanotechnology* **2008**, *19*, 445717.

97. Rheinlaender, J.; Geisse, N. A.; Proksch, R.; Schäffer, T. E. *Langmuir* **2011**, *27*, 697-704.

98. Guo, S.; Ward, M. D.; Wesson, J. A. *Langmuir* **2002**, *18*, 4284-4291.

99. Hillner, P. E.; Gratz, A. J.; Manne, S.; Hansma, P. K. *Geology* **1992**, *20*, 359-362.

100. Yamamoto, S.; Sugiyama, S.; Matsuoka, O.; Kohmura, K.; Honda, T.; Banno, Y.; Nozoye, H. *J. Phys. Chem.* **1996**, *100*, 18474-18482.

101. A. Coles, B.; G. Compton, R.; Booth, J.; Hong, Q.; H. W. Sanders, G. *Chem. Commun.* **1997**, 619-620.

102. Coles, B. A.; Compton, R. G.; Suárez, M.; Booth, J.; Hong, Q.; Sanders, G. H. W. *Langmuir* **1998**, *14*, 218-225.

103. Danesh, A.; Connell, S. D.; Davies, M. C.; Roberts, C. J.; Tendler, S. J. B.; Williams, P. M.; Wilkins, M. J. *Pharm Res* **2001**, *18*, 299-303.

104. Onuma, K.; Iijima, M. *J. Cryst. Process Technol.* **2015**, *5*, 1-8.

105. Hansma, P. K.; Drake, B.; Marti, O.; Gould, S. A.; Prater, C. B. *Science* **1989**, *243*, 641-643.

106. McKelvey, K.; Kinnear, S. L.; Perry, D.; Momotenko, D.; Unwin, P. R. *J. Am. Chem. Soc.* **2014**, *136*, 13735-13744.

107. Edwards, M. A.; Williams, C. G.; Whitworth, A. L.; Unwin, P. R. *Anal. Chem.* **2009**, *81*, 4482-4492.

108. Page, A.; Perry, D.; Young, P.; Mitchell, D.; Frenguelli, B. G.; Unwin, P. R. *Anal. Chem.* **2016**, *88*, 10854-10859.

109. Perry, D.; Paulose Nadappuram, B.; Momotenko, D.; Voyias, P. D.; Page, A.; Tripathi, G.; Frenguelli, B. G.; Unwin, P. R. *J. Am. Chem. Soc.* **2016**, *138*, 3152-3160.

110. Shevchuk, A. I.; Gorelik, J.; Harding, S. E.; Lab, M. J.; Klenerman, D.; Korchev, Y. E. *Biophys. J.* **2001**, *81*, 1759-1764.

111. McKelvey, K.; Perry, D.; Byers, J. C.; Colburn, A. W.; Unwin, P. R. *Anal. Chem.* **2014**, *86*, 3639-3646.

112. Li, C.; Johnson, N.; Ostanin, V.; Shevchuk, A.; Ying, L.; Korchev, Y.; Klenerman, D. *Prog. Nat. Sci.* **2008**, *18*, 671-677.

113. Chen, C.-C.; Zhou, Y.; Baker, L. A. *Annu. Rev. Anal. Chem.* **2012**, *5*, 207-228.

114. Novak, P.; Li, C.; Shevchuk, A. I.; Stepanyan, R.; Caldwell, M.; Hughes, S.; Smart, T. G.; Gorelik, J.; Ostanin, V. P.; Lab, M. J.; Moss, G. W. J.; Frolenkov, G. I.; Klenerman, D.; Korchev, Y. E. *Nat. Methods* **2009**, *6*, 279-281.

115. Korchev, Y. E.; Bashford, C. L.; Milovanovic, M.; Vodyanoy, I.; Lab, M. J. *Biophys. J.* **1997**, *73*, 653-658.

116. Chen, C.-C.; Derylo, M. A.; Baker, L. A. *Anal. Chem.* **2009**, *81*, 4742-4751.

117. Ying, L.; Bruckbauer, A.; Rothery, A. M.; Korchev, Y. E.; Klenerman, D. *Anal. Chem.* **2002**, *74*, 1380-1385.

118. Bruckbauer, A.; James, P.; Zhou, D.; Yoon, J. W.; Excell, D.; Korchev, Y.; Jones, R.; Klenerman, D. *Biophys. J.* **2007**, *93*, 3120-3131.

119. Sa, N.; Lan, W.-J.; Shi, W.; Baker, L. A. *ACS Nano* **2013**, *7*, 11272.

120. Binnig, G.; Quate, C. F.; Gerber, C. *Phys. Rev. Lett.* **1986**, *56*, 930.

121. Eaton, P.; West, P. *Atomic force microscopy*; Oxford University Press, 2010.

122. Noy, A.; Vezenov, D. V.; Lieber, C. M. *Annu. Rev. Mater. Sci.* **1997**, *27*, 381-421.

123. Yip, C. M.; Ward, M. D. *Biophys. J.* **1996**, *71*, 1071-1078.

124. Ward, M. D. *Chem. Rev.* **2001**, *101*, 1697-1726.

125. Poloni, L. N.; Zhong, X.; Ward, M. D.; Mandal, T. *Chem. Mater.* **2017**, *29*, 331-345.

126. Fotiadis, D.; Scheuring, S.; Müller, S. A.; Engel, A.; Müller, D. J. *Micron* **2002**, *33*, 385-397.

127. Dufrene, Y. F.; Ando, T.; Garcia, R.; Alsteens, D.; Martinez-Martin, D.; Engel, A.; Gerber, C.; Muller, D. J. *Nat Nano* **2017**, *12*, 295-307.

128. Gerber, C.; Lang, H. P. *Nat Nano* **2006**, *1*, 3-5.

129. Turner, Y. T. A.; Roberts, C. J.; Davies, M. C. *Adv. Drug Delivery Rev.* **2007**, *59*, 1453-1473.

130. Andrea, A.; Paolo, F. *Meas. Sci. Technol.* **2005**, *16*, R65.

131. Hillner, P. E.; Manne, S.; Gratz, A. J.; Hansma, P. K. *Ultramicroscopy* **1992**, *42*, 1387-1393.

132. Hillner, P. E.; Gratz, A. J.; Hansma, P. K., 1992, pp 160-170.

133. Manne, S.; Cleveland, J. P.; Stucky, G. D.; Hansma, P. K. *J. Cryst. Growth* **1993**, *130*, 333-340.

134. Hillier, A. C.; Ward, M. D. *Science* **1994**, *263*, 1261-1264.

135. Land, T. A.; De Yoreo, J. J.; Lee, J. D. *Surf. Sci.* **1997**, *384*, 136-155.

136. De Yoreo, J.; Land, T.; Rashkovich, L.; Onischenko, T.; Lee, J.; Monovskii, O.; Zaitseva, N. *J. Cryst. Growth* **1997**, *182*, 442-460.

137. Orme, C. A.; Noy, A.; Wierzbicki, A.; McBride, M. T.; Grantham, M.; Teng, H. H.; Dove, P. M.; DeYoreo, J. J. *Nature* **2001**, *411*, 775-779.

138. Dandekar, P.; Doherty, M. F. *Science* **2014**, *344*, 705-706.

139. Lupulescu, A. I.; Rimer, J. D. *Science* **2014**, *344*, 729-732.

140. Teng, H. H.; Dove, P. M.; Orme, C. A.; De Yoreo, J. J. *Science* **1998**, *282*, 724-727.

141. Mao, G.; Lobo, L.; Scaringe, R.; Ward, M. D. *Chem. Mater.* **1997**, *9*, 773-783.

142. Keel, T. R.; Thompson, C.; Davies, M. C.; Tendler, S. J. B.; Roberts, C. J. *Int. J. Pharm.* **2004**, *280*, 185-198.

143. Qiu, S. R.; Wierzbicki, A.; Orme, C. A.; Cody, A. M.; Hoyer, J. R.; Nancollas, G. H.; Zepeda, S.; De Yoreo, J. J. *Proc. Natl. Acad. Sci. U. S. A.* **2004**, *101*, 1811-1815.

144. Bosbach, D.; Jordan, D. G.; Rammensee, W. *Eur. J. Mineral.* **1995**, *7*, 267-276.

145. Jordan, G.; Rammensee, W. *Geochim. Cosmochim. Acta* **1996**, *60*, 5055-5062.

146. Bosbach, D.; Hall, C.; Putnis, A. *Chem. Geol.* **1998**, *151*, 143-160.

147. Higgins, S. R.; Jordan, G.; Eggleston, C. M.; Knauss, K. G. *Langmuir* **1998**, *14*, 4967-4971.

148. Jordan, G.; Rammensee, W. *Geochim. Cosmochim. Acta* **1998**, *62*, 941-947.

149. Higgins, S. R.; Jordan, G.; Eggleston, C. M. *Geochim. Cosmochim. Acta* **2002**, *66*, 3201-3210.

150. Godinho, J. R. A.; Putnis, C. V.; Piazolo, S. *Cryst. Growth Des.* **2014**, *14*, 69-77.

151. Ricci, M.; Segura, J. J.; Erickson, B.; Fantner, G.; Stellacci, F.; Voïtchovsky, K. *Langmuir.* **2015**, *31*, 7563-7571.

152. Peruffo, M.; Mbogoro, M. M.; Adobes-Vidal, M.; Unwin, P. R. *J. Phys. Chem. C* **2016**, *120*, 12100-12112.

153. Gasperino, D.; Yeckel, A.; Olmsted, B. K.; Ward, M. D.; Derby, J. J. *Langmuir* **2006**, *22*, 6578-6586.

154. Dhatt, G.; Lefrançois, E.; Touzot, G. *Finite element method*; John Wiley & Sons, 2012.

Chapter II	**Face-Discriminating Dissolution Kinetics of Furosemide Single Crystals: In Situ Three-Dimensional Multi-Microscopy and Modeling**

Abstract

A versatile in situ multi-microscopy approach to study the dissolution kinetics of single crystals is described, using the loop diuretic drug furosemide as a testbed to demonstrate the utility of the approach. Using optical microscopy and scanning ion-conductance microscopy in combination, the dissolution rate of individual crystallo- graphically independent crystal faces can be measured quantitatively while providing a direct visualization of the evolution of crystal morphology in real time in three dimensions. Finite element method models using experimental data enables quantitative analysis of dissolution fluxes for individual faces and determination of the limiting process ⸺mass transport or interfacial kinetics⸺ that regulates dis- solution. A key feature of the approach is that isolated crystals (typically <60 μm largest characteristic dimension) in solution during dissolution experience high and well-defined diffusion rates. The ability to obtain this quantitative information for individual crystal faces suggests a pathway to understanding crystal dissolution at the molecular level and regulating bioavailability, for example, through manipulation of crystal morphology.

1. Introduction

The majority of active pharmaceutical ingredients (APIs) are small-molecule organic crystals.[1,2] Crystallization is an essential step in their production, wherein the form (i.e. polymorph), crystal morphology, and crystal size impacts processing as well as other important physicochemical properties, including solubility and dissolution rate.[3-5] Dissolution is the first step in drug absorption from the solid form, and it plays a critical role in drug bioavailability.[6,7] Crystals are bounded by faces that are truncations of the three-dimensional lattice along specific crystallographic directions. As such, crystallographically unique faces are expected to exhibit different growth and dissolution behavior. Growth morphologies and kinetics of well-defined crystal faces have been explored using methods such as in situ scanning probe and interferometric microscopies,[8-13] often providing more insightful and accurate measurements of crystal growth than statistical sampling of bulk crystal morphologies.[14] Likewise, measurements of the dissolution kinetics of crystal suspensions that provide average rates of a population of crystals are common,[15-17] but measurements of dissolution of individual crystal faces of single crystals are rare. Mass transport conditions in such systems depend on several parameters that are not easily quantified, including type and speed of the stirrer, vessel and baffle geometry,[18,19] solution density and viscosity, diffusion, crystal morphology, and the quantity and size distribution of the solid particles.[18,20] Mass transport typically is not well defined, to the extent that deducing the kinetic regime can be difficult. Ideally, experimental studies should be configured to allow quantitative local mass transport, from which local undersaturation at the solid/liquid interface and the relationship between surface structure and reactivity can be obtained. Flow cell techniques overcome some of the limitations,[21,22] but typically these are limited to large macroscopic sample areas and particular crystal faces.

These approaches often are not ideal for the dissymmetric character of organic crystal surfaces, which typically are decorated with various crystallographically unique faces, edges, corners and defects that contribute differently to the dissolution process (mechanism and rate). In this respect, near-field microscopies are proving valuable for the study of the dissolution of individual crystals, including atomic force microscopy (AFM),[23-26] optical microscopy,[27,28] and scanning electrochemical microscopy

(SECM).[29] Rapid interfacial dissolution kinetics of crystals have been determined by SECM[30] and scanning electrochemical cell microscopy (SECCM).[31] *In situ* interferometry[32] can be useful for determining concentration gradients at crystal/solution interfaces by monitoring changes in the refractive index of the solution, although the minimum detectable concentration difference depends on the minimum fringe shift (ca. 10% of the total concentration change in solution)[33] and interferometric data tend to represent the average across the studied area. As such, they usually are not suitable for high resolution measurements of heterogeneous reactivity or concentration gradients.

New approaches for assessing dissolution kinetics are essential for the optimization of drug formulations, particular methodologies that permit facile and quantitative characterization of dissolution at a microscopic level that will fill knowledge gaps at the molecular level. Herein we describe a comprehensive approach to real-time characterization of the dissolution of individual faces of single crystals using optical microscopy, scanning ion-conductance microscopy (SICM) and finite element method modeling. SICM is a powerful non-contact method that makes use of a nanopipette for high resolution topographical imaging,[34-36] with the potential to map the dissolution behavior of individual topographical features on crystal surfaces. Collectively, these enable determination of concentration gradients, interfacial concentrations, and separation of kinetic and mass transport limiting regimes. This approach is demonstrated here for the API furosemide (Scheme 2.1), a loop diuretic drug marketed under the brand name Lasix.[37] Furosemide is a weak acid, classified as a BCS Class IV drug because of its low permeability and poor solubility.[38] Consequently, the bioavailability of furosemide from oral dosage is low (60%) and the rate and extent of absorption varies between and within individuals.[39] It is reasonable to suggest that understanding the dissolution kinetics of furosemide crystals at the microscopic level could lead to strategies for improving its bioavailability and its optimum solid-state form.[3,40-43]
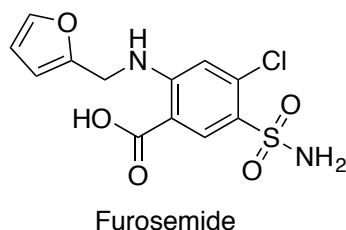
Furosemide

Scheme 2.1. The molecular structure of furosemide

2. Experimental

2.1 Samples and Solutions

Furosemide was purchased from Sigma-Aldrich (>98%, St. Louis, MO) and used as obtained without further purification. Crystals of furosemide were prepared by mixing 0.5 mL of a 10 mM solution of furosemide in ethanol (Sigma-Aldrich, >99.5%) with 3.5 mL deionized (DI) water produced by Purite Select HP with resistivity 18.2 MΩ cm (25 °C) to create a supersaturated solution. The mixture was added by pipette to a 47 mm diameter circular glass microscope slide (Thermo Scientific, Inc., Waltham, MA) previously mounted into a 47 mm diameter Petri dish (Willco Wells, Netherlands) with a Plexiglas rim, covered, and allowed to stand at room temperature for 15 minutes. The supernatant solution was then removed to reveal small raft-shaped crystals of furosemide, typically < 60 μm long, attached to the glass slide, which was then rinsed with water and dried with a nitrogen stream. All dissolution studies were performed at 25 °C and pH 6.5 in 50 mM KCl (Sigma-Aldrich, AR grade) in ultrapure water. Solution pH was measured with a pH meter (Metler Toledo, Switzerland)).

2.2 X-ray Characterization

Single crystal X-ray diffraction analysis of furosemide was performed using a suitably large crystal of furosemide (>100 μm) that was mounted on a Mitegen loop with silicon oil and placed on an Oxford Diffraction Xcalibur Gemini diffractometer equipped with a Ruby CCD area detector. The crystal temperature was maintained at 150(2) K during data collection. The crystal structure was solved using Olex2[44] with the ShelXS-2013[45] structure solution program using Direct Methods and refined with the XL refinement package using Least Squares minimization. Powder X-ray diffraction measurements were performed using a Panalytical X'Pert Pro MRD

equipped with a hybrid monochromator for CuKα_1 radiation (l = 1.541 Å). The glass slide on which the furosemide crystals were grown was mounted on the sample holder. A Pixcel detector was used in scanning mode over the range 5° < 2θ < 30°, stepping 0.025° over a period of 45 minutes.

2.3 Morphology Prediction

To identify the exposed crystal faces, the furosemide crystal morphology was calculated based on the growth morphology method using the Morphology module in Materials Studio (Materials Studio 8.0.100.21, Accelrys, San Diego, CA). The growth morphology method takes into account the energetics of the system and requires the selection of an appropriate forcefield. The geometry of the furosemide unit cell obtained from single crystal CCD X-ray diffraction experiments was optimized using the COMPASS, consistent-valence forcefield (cvff), and Dreiding forcefields and the optimized unit cell with lowest lattice energy and lattice parameters best matching the experimental unit cell was selected for morphology predictions. Geometry optimizations were conducted using the Forcite molecular mechanics tool. The Quasi-Newtown algorithm was used with a convergence tolerance of 2.0×10^{-5} kcal/mol for the energy, 0.001 kcal/mol/Å for the force, and 1.0×10^{-5} Å for the displacement. The Ewald summation method was chosen for the evaluation of van der Waals and electrostatic terms to an accuracy of 0.0001 kcal/mol with a buffer width of 0.5 Å. Forcefield-assigned partial charges were used with the COMPASS and cvff forcefields and the QEq method was used to calculate and assign partial charges with the Dreiding forcefield. The furosemide unit cell optimized with COMPASS was used for the morphology predictions, conducted with a minimum interplanar distance d_{hkl} of 1.300 Å and a maximum Miller Index value (hkl) of (333). The maximum number of faces was limited to 200.

2.4 Scanning Ion-Conductance Microscopy

Dissolution investigations were performed by combining optical microscopy and SICM by mounting an SICM system on an inverted optical microscope (Axiovert 40 CFL, Zeiss, Germany). The optical microscope was equipped with an LED light source to reduce sample heating and a video camera (B700, PixeLINK) to assist the selection and monitoring of the crystal. SICM probes (ca. 100 nm diameter) were

fabricated from borosilicate glass capillaries (1.2 mm o.d., 0.69 mm i.d., Harvard Apparatus, Holliston, MA) using a laser puller (P-2000, Sutter Instruments, Novato, CA) and optimized pulling parameters (Line 1: Heat 350, Fil 3, Vel 30, Del 220, Line 2: Heat 350, Fil 3, Vel 40, Del 180, Pul 120). The nanopipettes were filled with the same electrolyte solution (50 mM KCl) as the aforementioned solution used for dissolution studies. An Ag/AgCl quasi-reference counter electrode (QRCE) was inserted into the nanopipette and another was submerged in the petri dish bulk solution. The nanopipettes were mounted on a 38 μm – travel range single axis (Z) piezoelectric positioner (P-753-3CD, PhysikInstrumente, Germany) to control the height of the probe and oriented normal to the surface of interest, as previously described.[46] The petri dish containing the furosemide crystals was mounted on a two-axis (XY) piezoelectric positioner system (Nano-BioS300, Mad City Labs Inc., Madison, WI) for lateral positioning. The SICM was operated in bias modulated (BM) mode,[47] in which there was zero net bias between the two QRCEs. A lock-in amplifier (SR830, Stanford Research Systems, Sunnyvale, CA) was used to generate an oscillating bias (38 mV amplitude, 357 Hz frequency) applied to the bulk QRCE, and the resulting current was measured at the QRCE in the nanopipette using a custom-built wideband current-to-voltage converter. The instrument was controlled and data collected with a programmed FPGA card (7852R, National Instruments, Austin, TX) using LabVIEW (2013, National Instruments, Austin TX).

The experimental configuration for optical and SICM dissolution measurements is illustrated in Figure 2.1. Furosemide crystals, typically with the longest dimension ranging from 30 - 60 μm and various length-width-height ratios, were selected. Some crystals were removed to create separations greater than 40× times their largest dimension to ensure high undersaturation (sink conditions) and avoid overlap of diffusion profiles among neighboring crystals. Following addition of 4 mL of a 50 mM aqueous solution of KCl to the Petri dish, time-lapse sequence of optical images (400× magnification, every 30 s) and line traces along the crystal in an SICM hopping mode[48,49] were acquired. The nanopipette probe was lowered toward the surface at a rate of 1 μm s^{-1} at each position. When the surface was detected by the probe as a change in the phase of the AC current to a defined set point (typically 0.1° change from the bulk phase value), the Z position was recorded and the nanopipette was retracted 5 μm at a rate of 10 μm s^{-1}, after which it was moved laterally to a new

location, typically 3-6 μm from the previous position. This process was then repeated at a minimum of 10 lateral positions, which enabled acquisition of line profile and measurement of crystal height in approximately 60 seconds. Crystal dimensions were determined from the optical microscope images using ImageJ (version 1.45, NIH).
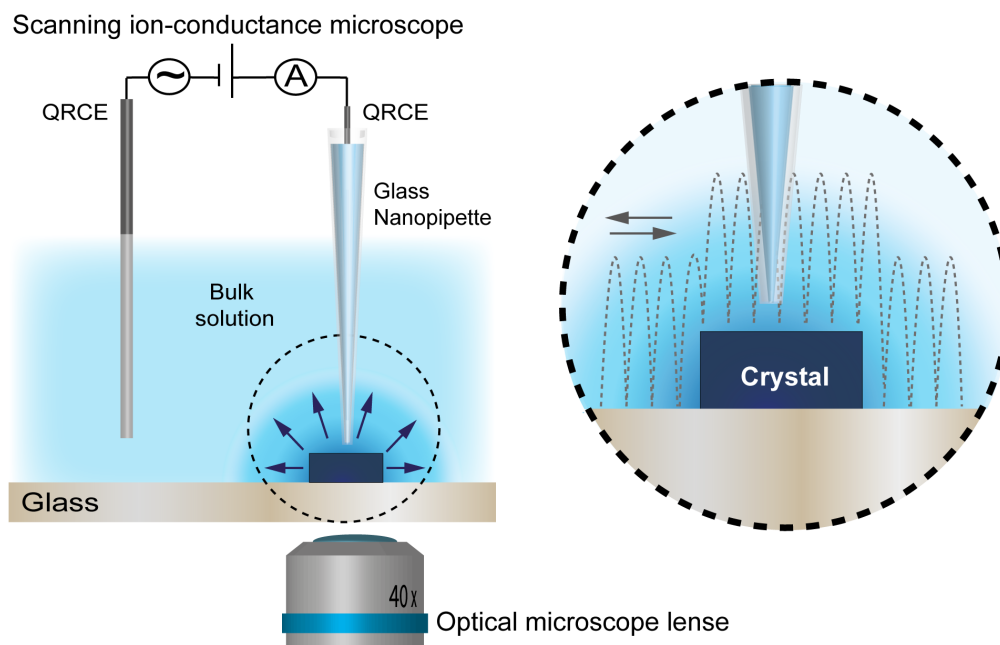
Figure 2.1. Optical microscopy–SICM configuration. The SICM system was mounted on an inverted optical microscope for the simultaneous tracing of the dissolution process by optical microscopy and SICM. The petri dish containing the crystals was positioned on the microscope stage and the nanopipette for SICM scans was submerged normal to the surface. Line traces of the local height along the crystal were generated in hopping mode BM-SICM, with the probe scanned forward and backward over the same line along the crystal (right).

2.5 Atomic Force Microscopy

AFM images of furosemide crystals mounted on the glass slide in the Petri crystallization dish were acquired in air before and after partial dissolution using a BioScope Catalyst microscope (Bruker, Billerica, MA). Crystals separated by >10 times the largest crystal dimension were allowed to dissolve partially after addition of 4 mL of 50 mM aqueous solution of KCl to the petri dish for 10 minutes. The electrolyte solution was then removed and the partially dissolved crystals were rinsed quickly with DI water and dried with a nitrogen stream. AFM images were acquired in the *ScanAsyst mode* using triangular-shaped silicon nitride cantilevers (SNL-10, Bruker, Billerica, MA) with a resonant frequency of ~65 kHz and ~0.35 N/m spring

constant and a data collection resolution of 512 points per raster line. The images were analyzed with SPIP software (6.0.14, Image Metrology, Denmark).

2.6 Simulations

Numerical simulations were performed using the commercial finite element method package Comsol Multiphysics 4.4 (Comsol AB, Sweden) installed on a Dell Intel Core 7i Quad 2.93 GHz computer equipped with 16 GB of RAM running Windows 7 Professional 64 bit. The "mass transport of diluted species" module was used in the 3D domain illustrated in Figure 2.2.
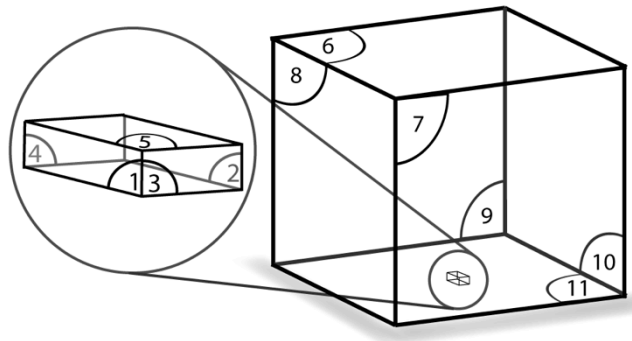
Figure 2.2. Three-dimensional domain used for FEM simulations (not drawn to scale). The numbers correspond to the boundaries described in Table 2.1.

The maximum characteristic diffusional time for mass transport from microscopic surfaces to bulk solution can be estimated using a semi-infinite diffusion model according to equation 2.1, where t_{diff} is the steady-state diffusion time, d is crystal largest dimension size and D denotes diffusion coefficient.

$$t_{diff} \approx d^2 / D \tag{2.1}$$

The diffusion coefficient of furosemide (6.15×10^{-6} cm^2/s) was estimated from the Wilke-Chang correlation[50] (equation 2.2):

$$D = 7.4 \times 10^{-8} \frac{(xM)^{1/2} T}{\eta \overline{V}^{0.6}} \tag{2.2}$$

where D is the diffusion coefficient, x is the association parameter of the solvent, M is the molecular weight of the solvent, T is temperature, η denotes the viscosity of the

solution and $\overline{V}$ is the molar volume of solute at normal boiling point. The diffusion coefficient was assumed constant over the entire domain. The diffusion time for a dissolving crystal of $d \sim 45$ μm is about 3 seconds, three orders of magnitude faster than the duration of a typical crystal dissolution experiment (30 minutes for the complete dissolution of a crystal). The influence of convection was neglected due to the small nature of the studied crystals (largest dimension < 60 μm).[51] Mass transport by diffusion was therefore assumed to be effectively at a steady-state, such that the flux conservation relation in equation 2.3 was valid, where J is the flux and c is the concentration of the furosemide solute

$$\nabla J = -D\nabla^2 c = 0 \qquad\qquad (2.3)$$

The model, denoted here M1, was developed by applying a flux (per unit area) for each crystal face (observed dissolution rate, $J_{(hkl)}^{Obs}$) measured experimentally. Using the appropriate boundary conditions (Table 2.1) the concentration of furosemide in the solution around the dissolving crystal could be simulated, from which it was possible to distinguish the dissolution regime, i.e., mass transport *vs.* kinetic control; *vide infra*. In order to deduce the relative importance of mass transport and surface kinetics, a model (M2) with the same geometry but different boundary conditions was employed (Table 2.1), such that dissolution was controlled by diffusion (crystal/solution interface saturated). Solution of the partial differential equations for both models (M1 and M2) was achieved using the direct solver MUMPS in the COMSOL environment, with a relative error tolerance of 10^{-6}. Simulations were carried out with >7,500,000 tetrahedral mesh elements. The mesh resolution was refined to be the finest, down to a value of 0.1 nm, at the surfaces of the crystal.

Table 2.1. Boundary conditions for numerical simulations of furosemide crystal dissolution

Boundary	Characteristics	Boundary conditions M1	Boundary conditions M2
1, 2	Crystal faces {010}	$J^{Obs}_{(hkl)} = -\mathbf{n} \cdot (D\nabla c)$	$c = c_s$
3, 4	Crystal faces {101}	$J^{Obs}_{(hkl)} = -\mathbf{n} \cdot (D\nabla c)$	$c = c_s$
5	Crystal face (001)	$J^{Obs}_{(hkl)} = -\mathbf{n} \cdot (D\nabla c)$	$c = c_s$
6, 7, 8, 9, 10	Bulk solution	$c = c_0 = 0$	$c = c_0 = 0$
11	Glass slide	$0 = -\mathbf{n} \cdot (D\nabla c)$	$0 = -\mathbf{n} \cdot (D\nabla c)$

The boundary numbers are for the planes labeled in Figure 2.2
$\mathbf{n}$ denotes the vector normal to the surface
c_s is the solubility concentration of furosemide (0.2 mM)

3. Results and Discussion

3.1 Furosemide Crystals

Four polymorphic forms and two solvates of furosemide have been reported previously.[37,52,53] The investigation described herein focused on Polymorph I, which is the only polymorph present in the commercial drug.[53] Single crystal CCD X-ray diffraction confirmed that recrystallized furosemide crystals were polymorph I, which crystallizes in the triclinic P-1 space group (see Supporting Information Table 2.5).[37] Powder X-ray diffraction of furosemide crystals grown on a glass slide from ethanol/water solutions supersaturated with furosemide revealed only peaks corresponding to the (*00l*) reflections (*l* = 1 - 3), confirming that the crystals were oriented with the (001) face parallel to the glass slide (Supporting Information, Figure 2.8). Optical microscopy revealed a raft-like habit with a triclinic morphology (Figure 2.3A, B).
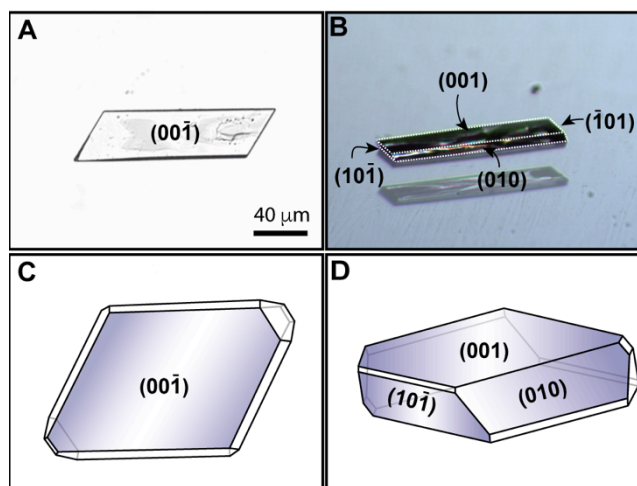
Figure 2.3. Morphology of a typical recrystallized furosemide crystal (Polymorph I). The different faces that can be seen are labeled. (A) Image acquired with an optical microscope, normal to the $(00\bar{1})$ face. (B) Optical image acquired with a magnifying CCD camera in an SICM experiment (the lighter image is the reflection of the actual crystal in the glass slide). (C) Habit of furosemide Polymorph I calculated using the growth morphology method, viewed normal to the $(00\bar{1})$ face. (D) Calculated habit of furosemide Polymorph I oriented to reveal other major crystal faces.

Crystal morphology prediction can serve as a useful aid in identifying relevant crystal faces when crystal dimensions are less than those required for indexing by X-ray diffraction. Methods for predicting crystal morphology based on crystal structure have become routine and yield crystal morphologies that are consistent with experimental morphologies for a wide range of molecular crystals despite a lack of consideration for the external growth environment.[54] These methods include (*i*) the Bravais-Friedel Donnay-Harker (BFDH), a geometric calculation based on crystal lattice and symmetry; (*ii*) the equilibrium method, based on the surface free energies of relevant crystal faces; and (*iii*) the growth (or "attachment energy") method, based on attachment energies corresponding to relevant crystal faces. The growth method (*iii*) is most effective when considering only the internal interactions of the crystal structure.[55-56] The growth method, developed by Hartmann and Perdok, relies on the bond energy released when one building unit is attached to the surface of a crystal face to predict crystal morphology.[57,58] The growth rate normal to a particular face is proportional to the attachment energy for that surface — large attachment energies (*i.e.* more negative values) for a specific face correspond to strong out-of-plane intermolecular interactions, corresponding to faster growth normal to the plane and a lower morphological significance for the face.

Three force fields that have been used often for the prediction of organic crystals habits[59-61] were evaluated for predicting the morphology of furosemide Polymorph I. The molecular geometries and lattice parameters of the furosemide unit cell were optimized using the COMPASS, Dreiding, and cvff forcefields (see Supporting Information Table 2.6). The COMPASS forcefield was chosen for morphology calculations because it provided the lowest lattice energy and the lattice parameters best matched those of the experimental unit cell. The furosemide morphology predicted from the COMPASS forcefield reveals that three crystal faces — (001), (010) and ($10\bar{1}$) — contribute to 90% of the predicted total area of the crystal (Figure 2.3C, D; Table 2.2). Crystal faces with a calculated area of <5% were not observed in the experimental morphology, which is not surprising given that experimental crystal habit is strongly affected by many environmental factors, including solvent, supersaturation, pH, and temperature,[59,62] which are not captured in the morphology prediction calculations. These crystal faces, if present, cannot be studied by the measurements conducted in our experiments and are not addressed here.

Table 2.2. Morphology predictions for the optimized structure of furosemide (Polymorph I) by growth morphology calculations using COMPASS force field.

Face (*hkl*)	d_{hkl} (Å)	E_{att} (kcal mol^{-1})	Total facet area (%)
(0 0 1)	13.854	-33.917	53.16
(0 1 0)	9.021	-78.355	18.15
(1 0 $\bar{1}$)	8.613	-79.740	18.82
(0 1 $\bar{1}$)	8.469	-87.333	3.44
(1 0 0)	8.411	-94.402	1.81
(1 $\bar{1}$ 0)	8.365	-124.774	4.02
(1 $\bar{1}$ $\bar{1}$)	7.626	-124.298	0.59

3.2 Determination of Dissolution Rates and Interfacial Concentrations

Since the introduction of SICM,[34] different modes such as constant distance,[35] hopping approach,[49] and hybrid[63] have been used to acquire images of the topography of soft surfaces[36, 64] and for local ion current measurements.[65-67] Most recently, a new method based on the application of an oscillating bias between both QRCEs to generate an alternating ion current (AC) feedback signal, bias modulated SICM (BM−SICM),[47] has been introduced. This approach has several advantages over the traditional nanopipette oscillation SICM method, including minimization of perturbations of the local ionic atmosphere and from effects of convection (stirring) and electro-osmosis. Moreover, it offers opportunities for faster imaging.[67]

The dissolution rate is expected to be determined by a combination of (*i*) interfacial (intrinsic) dissolution kinetics, which are governed by energetics of the surface and solvation effects, and (*ii*) mass transport of dissolved species from the crystal surface to the bulk solution.[18] Consequently, dissolution kinetics reflects a competition between these two processes, with the slowest governing the overall rate, leading to either kinetic (interfacial) control, mass transport (diffusion) control, or a mixed regime where both contributions are comparable. The measurement of intrinsic dissolution kinetics requires the mass transport rates to be comparable to or greater than surface kinetics, which in turn requires that mass transport is well defined and calculable.

The temporal change in the lateral dimensions of furosemide crystals (i.e. the size of the (001) face) was recorded by measurement of the retreat of the {010} and {101} faces using optical microscopy (Figure 2.4A). The changes in crystal height (normal to the (001) face) were obtained by BM-SICM for the (001) face (Figure 2.4B, D). Collectively, these measurements identify the change in crystal size for all three dimensions. The dissolution rate was effectively constant for all three faces during the first ten minutes, but at longer times the dissolution rate increased. The faster dissolution rate was accompanied by surface roughening and the formation of pits on the (001) surface (*vide infra*), which were evident even in optical images. It is reasonable to suggest that the roughened surfaces and pits would result in higher index microfacets in the crystal surface, leading to enhanced dissolution kinetics (Figure 2.4A). Under these conditions, it is anticipated that crystal dissolution

becomes increasingly limited by mass transport.[28,68-70] This is consistent with our recent observation of the dissolution kinetics of the (110) face of salicylic acid in aqueous solution using hopping intermittent contact-scanning electrochemical microscopy,[70] where we found a strong influence of surface roughness on the dissolution kinetics.
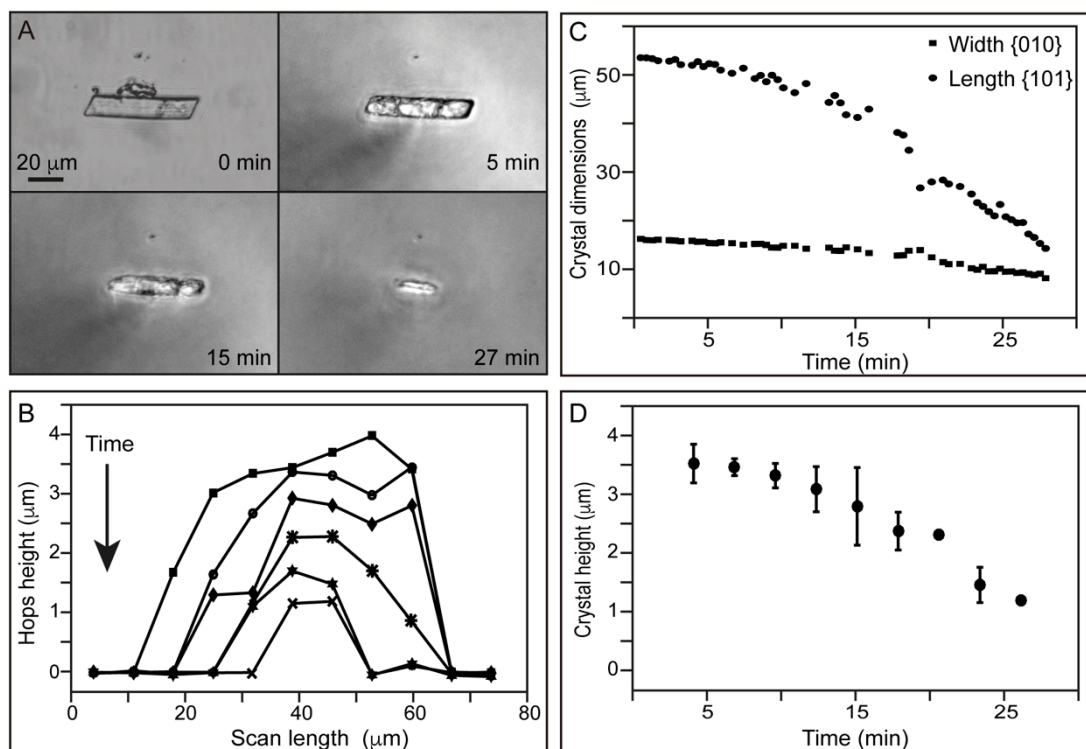
Figure 2.4. (A) Representative time-lapse optical microscopy images of the dissolution of a furosemide crystal. (B) BM-SICM line scans recorded at: 4 (■), 10 (•), 15 (♦), 20 (✱), 23 (✦) and 26 (✗) minutes after the beginning of dissolution. (C) Retreat of the {010} and {101} faces (length and width dimensions) over time. (D) Reduction of the crystal height during dissolution, plotted as an average value of all the hops landed on the crystal surface in a SICM line scan.

The early stage of dissolution, where the rate was constant, was investigated for nine furosemide crystals in order to compare the initial dissolution rates for the three crystallographically unique crystal faces. In this regime the dissolution rates likely correspond to the kinetic processes at the low index faces rather than the higher index microfacets that define the pitted surface. The rates of dissolution ($J_{(hkl)}^{Obs}$) were determined using equation 2.4, where $v_{(hkl)}$ is the dissolution velocity of face *hkl* and $\overline{V}_{crystal}$ is the molar volume of furosemide (200.692 cm^3/mol, calculated from the

density of polymorph I, 1.648 g/cm^3). The standard deviation of the $J_{(hkl)}^{Obs}$ values is rather large, which can be attributed to the small sample size, the use of crystals with slightly different dimensions, and mixed kinetic-mass transport control (*vide infra*). Nonetheless, it is evident that the different faces exhibit different dissolution rates, with $J_{(hkl)}^{Obs}$ increasing in the order $(001) < (010) < (10\bar{1})$, inversely proportional to the areas of the faces.

$$J_{(hkl)}^{Obs} = v_{(hkl)} / \overline{V}_{crystal} \qquad\qquad (2.4)$$

Table 2.3. Average face-resolved initial dissolution rates of 9 furosemide crystals.

Face (*hkl*)	J_{Obs} (mol m^{-2} s^{-1})
$(10\bar{1})$	$(16.1 \pm 6.7) \times 10^{-6}$
(010)	$(12.6 \pm 6.9) \times 10^{-6}$
(001)	$(2.8 \pm 1.4) \times 10^{-6}$

Crystallographically unique faces of a molecular crystal will have different chemical compositions and molecular topography. Consequently, different interactions with the external environment can be expected for these faces,[71] as well as different step/kink energetics. The dissolution rates of crystal faces depend on the energetics associated with each surface. The lowest energy surfaces are those in which the weakest bonds are truncated. In the furosemide crystal, each molecule participates in six hydrogen bonds with five neighboring furosemide molecules — one O···HO, one OH···O, two NH···O, and two O···HN (Scheme 2.2), forming a complex hydrogen-bonding network that is truncated differently at each of the morphologically significant (001), (010), and $(10\bar{1})$ faces (Figure 2.5). The (001) face presents furanyl rings, which do not form hydrogen bonds with other furosemide molecules, to the external environment. Moreover, the hydrogen bonding network is contained within the (001) plane such that hydrogen bonds are not truncated at the surface and in-plane interactions are strong, characteristic of a face with low surface energy, slow growth, and a large morphological importance (Figure 2.5A). In contrast, the (010) and $(10\bar{1})$ surfaces expose aminosulfonyl and carboxyl groups at the surface, thereby truncating

the hydrogen-bonding network (Figure 2.5B, C). Based on this structural inspection alone, the (001) face would be expected to have a lower attachment energy than the (010) and ($10\bar{1}$) faces and should have the slowest growth rate normal to the surface, and be the slowest dissolving crystal face as well. This is consistent with the observed and calculated crystal morphology (Figure 2.3 and Table 2.2), as well as the measured dissolution rates (Table 2.3). The comparable morphological significance of (010) and ($10\bar{1}$) suggests that these surfaces have comparable growth and dissolution rates. The ($10\bar{1}$) face, however, exhibits a somewhat higher dissolution rate compared to (010), although the two are comparable within error. The corrugation of the (010) face suggests that solvent ordering or surface reconstruction may be likely, which would stabilize this face and slow its dissolution rate compared to the relatively flat ($10\bar{1}$) face.[72] Nonetheless, the order of the observed dissolution rates of the different furosemide crystal faces (001) < (010) < ($10\bar{1}$) agrees with the hydrogen bonding model as well as the attachment energy calculations. This trend becomes even clearer when mass-transport corrections are introduced (*vide infra*).
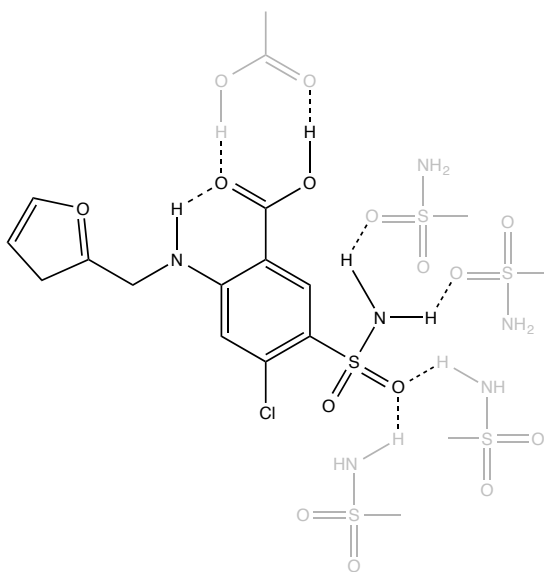
Scheme 2.2. The molecular structure of furosemide (black) and hydrogen bonds formed by each molecule with neighboring furosemide molecules (grey) in the crystal structure.
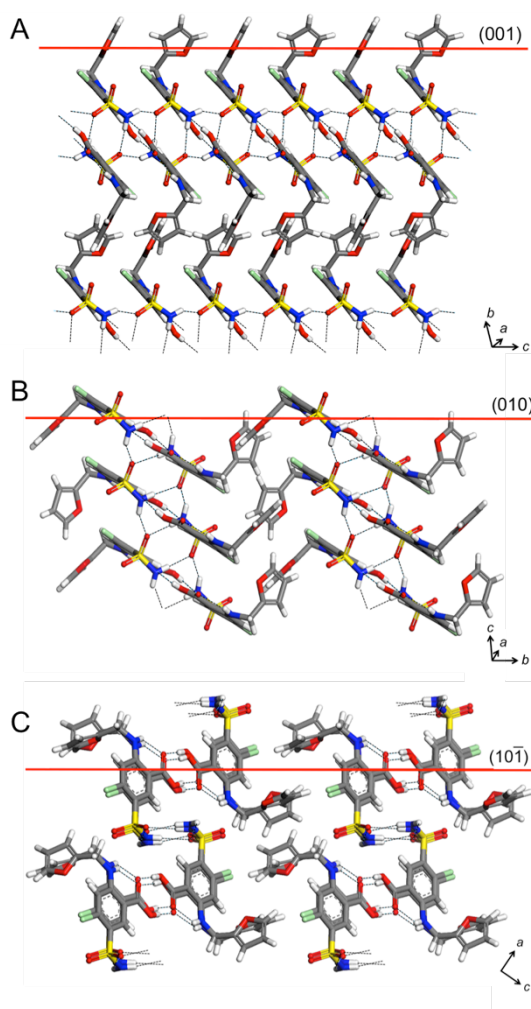
Figure 2.5. Structure of furosemide crystal faces: (A) (001), (B) (010), and (C) (10$\bar{1}$). Black dotted lines represent hydrogen bonds.

3.3 Mass Transport-Corrected Intrinsic Dissolution Kinetics

FEM models were formulated for each of the nine crystals studied to obtain more insight into the dissolution kinetics, particularly the role of mass transport. These computations accounted for the experimental dissolution rate ($J_{(hkl)}^{Obs}$) obtained for each individual crystal face, crystal size and crystal morphology, thereby producing the concentration distribution and diffusive flux of furosemide. The results from FEM modeling of the dissolution of four representative furosemide crystals are provided in Figure 2.6. The calculations reveal that the concentration of furosemide at the solid/liquid interface is higher than in the bulk solution (0 mM), with large concentration gradients (diffusion layer) between the crystal and the bulk solution, consistent with significant contributions from mass transport. Notably, the calculated

concentration in the vicinity of each crystal face differs, demonstrating that the balance between mass transport and surface kinetics for each crystal face during the dissolution process is different. The calculated surface concentrations increase in the order $C_{(001)} = 0.12 \pm 0.04$ mM $< C_{(010)} = 0.15 \pm 0.04$ mM $< C_{(10\bar{1})} = 0.17 \pm 0.03$ mM, consistent with the order of faster kinetics expected and a trend towards an increased degree of mass transport control. The contribution of surface kinetics is important on those faces where the interfacial concentration is less than the solubility of furosemide (0.2 mM),[73] a value that was confirmed by UV–Vis absorption (Supporting Information, Figure 2.9). The interfacial concentration alone, however, is not indicative of dissolution kinetics due to the possible redistribution of the solute between the different crystal faces, which depends on the direction and magnitude of the diffusive flux of material, crystal size and morphology. A more accurate quantitative determination of the contribution of the surface kinetics ($J_{(hkl)}^{SK}$) can be obtained for each crystal face by comparing the experimental flux ($J_{(hkl)}^{Obs}$) determined in model M1 (see Experimental Section), with the value of the theoretical diffusive flux on each crystal face predicted from simulations for a pure mass transport controlled system ($J_{(hkl)}^{MT}$) parameterized with the same crystal geometry (model M2). The overall flux involves mass transport and surface kinetics in series, according to equation 2.5,

$$\frac{1}{J_{(hkl)}^{Obs}} = \frac{1}{J_{(hkl)}^{MT}} + \frac{1}{J_{(hkl)}^{SK}} \tag{2.5}$$

$J_{(hkl)}^{Obs}$ for (010) and (10$\bar{1}$) was very close to $J_{(hkl)}^{MT}$ ($J_{(hkl)}^{Obs} \approx J_{(hkl)}^{MT}$), consistent with fast surface dissolution kinetics ($J_{(hkl)}^{SK} >> J_{(hkl)}^{MT}$). Conversely, for the (001) face, except for one crystal (among the nine) that could not be distinguished from mass-transport control, $J_{(hkl)}^{Obs}$ was always much smaller than $J_{(hkl)}^{MT}$ ($J_{(hkl)}^{Obs} << J_{(hkl)}^{MT}$), consistent with mixed kinetic control ($J_{(hkl)}^{SK} \approx J_{(hkl)}^{MT}$). For the (001) face, the average value of $J_{(hkl)}^{MT}$ for the range of crystals shown (7.35×10^{-6} mol m^{-2} s^{-1}) is about twice the size of the average value of $J_{(hkl)}^{SK}$ (4.39×10^{-6} mol m^{-2} s^{-1}). It is important to note,

however, that a range in values was obtained for $J_{(hkl)}^{Obs}$, $J_{(hkl)}^{MT}$ and $J_{(hkl)}^{SK}$ across the different crystals studied. This is attributed to the different numbers of defects in each crystal and the different crystal sizes. The average values for each flux contribution for each crystal face are provided in Table 2.4 (more detail is provided in Supporting Information, Table 2.7).
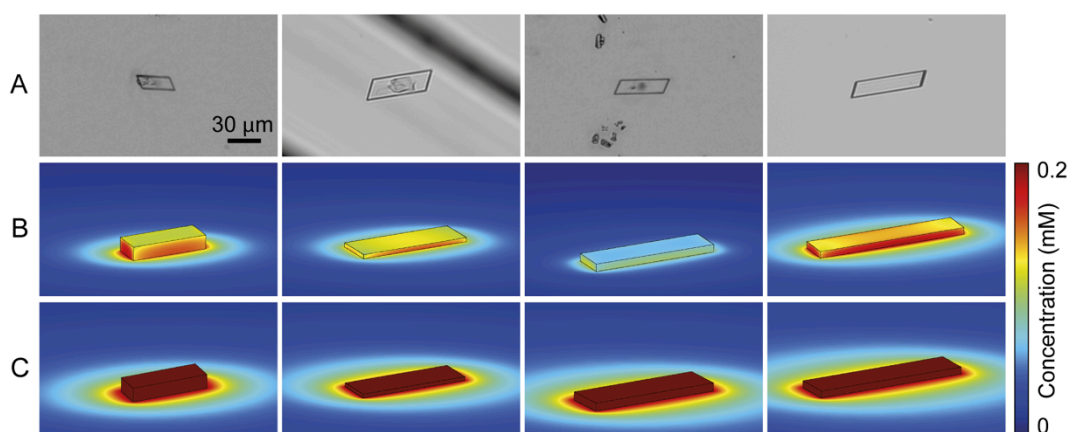
Figure 2.6. (A) Optical microscopy images of single furosemide crystals. (B) Results of FEM simulations (M1) for the concentration distribution of furosemide during the dissolution. (C) Concentration distribution of furosemide in the solid/liquid interface in a mass transport controlled dissolution process (M2).

Table 2.4. Average diffusive fluxes per unit area for each crystal face calculated from FEM simulations of eight furosemide crystals.

Face (*hkl*)	J_{Obs} (mol m^{-2} s^{-1})	J_{MT} (mol m^{-2} s^{-1})	J_{SK} (mol m^{-2} s^{-1})
(10$\bar{1}$)	$(16.1 \pm 6.7) \times 10^{-6}$	$(15.0 \pm 4.9) \times 10^{-6}$	Near diffusion control
(010)	$(12.6 \pm 6.9) \times 10^{-6}$	$(11.7 \pm 3.6) \times 10^{-6}$	Near diffusion control
(001)	$(2.8 \pm 1.4) \times 10^{-6}$	$(7.4 \pm 1.8) \times 10^{-6}$	$(4.4 \pm 2.7) \times 10^{-6}$

Dislocations are recognized to be important for etch pit formation during dissolution.[74] Pitting leads to both an increase in the specific surface area and the formation of microdomains (pit walls) of higher surface energy that produces an increased dissolution rate.[70] In the case of furosemide crystals, a collection of crystals

was examined by AFM before and after their immersion in aqueous solution for 10 minutes (Figure 2.7).
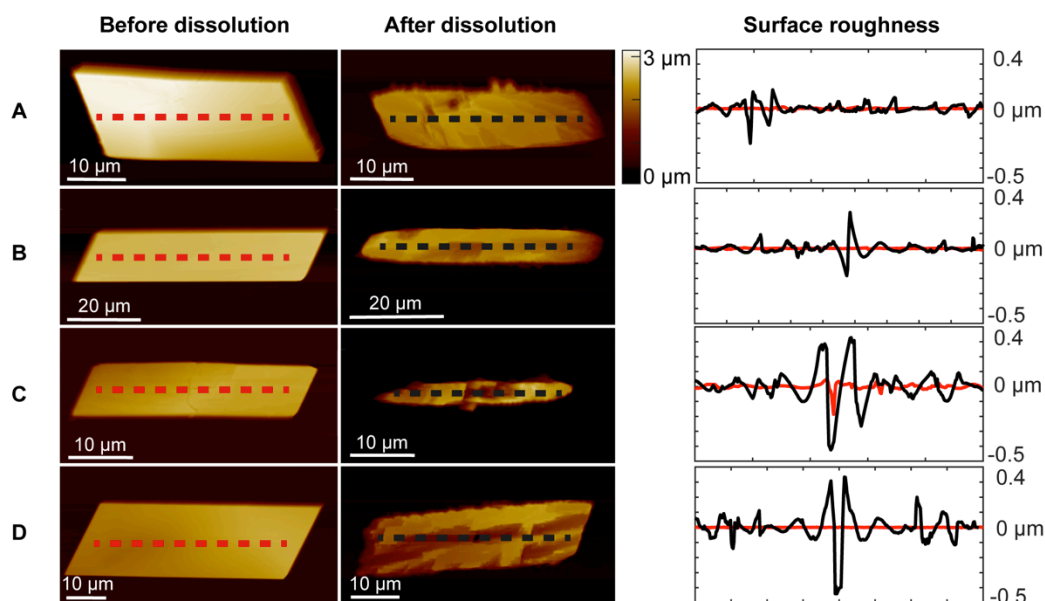
Figure 2.7. AFM images of single furosemide crystals before dissolution and after partial dissolution for 10 minutes. The dashed red and black lines indicate the line profile used to measure the surface roughness before and after dissolution respectively (left). Surface roughness (right) of the (001) face in each of the four crystals before dissolution (red) and after partial dissolution (black).

Prior to dissolution the (001) surfaces are largely free of defects, except for crystal C, which appears to be somewhat rough based on an AFM line profile (red line in Figure 2.7C). After simultaneous immersion for 10 minutes, the crystals have dissolved, although to different extents. Moreover, the number and depth of pits on the (001) face differ for each crystal. It can be appreciated in the images that the extent of dissolution depends on the initial crystal size, the ratio of the size of the (010) and $(10\bar{1})$ faces, and the initial surface roughness. Overall, the smaller the crystal, and the smaller the size of the $(10\bar{1})$ face in relation to the (010) face, and the rougher the crystal surface, the faster the dissolution. All these characteristics are united in crystal C which is the smallest crystal (37 μm length), has a small $(10\bar{1})$ face and the clear presence of a defect on the (001) surface (surface roughness profile in red in Figure 2.7) prior to dissolution. After 10 minutes, crystal C has dissolved by *ca.* 70 % from its initial volume, while the other crystals have dissolved by between 45 % and 60 %. Differences in the pitting density (surface area and roughness) are evident in the

images after dissolution and the surface roughness plot in Figure 2.7. The (001) surface of the dissolved crystals A and B is characterized by a smaller proportion of pits than crystals C and D. After the 10 minute dissolution period, the decrease in crystal size, as well as the roughening of the crystal faces exposed to the solvent by the formation of pits and exposure of high index faces, explains the increased dissolution kinetics at longer times (Figure 2.4).

4. Conclusions

The dissolution kinetics of the individual faces of single furosemide crystals (polymorph I) have been investigated by a versatile *in situ* multimicroscopy approach, comprising SICM and optical microscopy combined with finite element method (FEM) modeling. The experimental approach allowed 3D visualization of crystal morphology during dissolution, from which a numerical model was developed to calculate the concentration distribution around the crystal and dissolution flux of furosemide at the solid/liquid interface. This allowed the quantitative comparison of mass transport and surface kinetics. It has been shown that the (001) face is strongly influenced by surface kinetics (mixed kinetic control), while the (010) and $(10\bar{1})$ faces are dominated by mass transport. Our findings have important consequences for the reporting of dissolution kinetics: dissolution rates vary considerably from crystal to crystal and are time dependent at large dissolution times (>10 minutes). This is due to the impact of a range of factors, including subtle effects from crystal size, shape and the apparent number of defects (pits) in a particular crystal, and as shown by complementary AFM measurements. By studying individual microscale crystals within a population, we have been able to identify kinetic distributions for individual faces and rationalize the results in terms of crystal structure and surface properties. The ability to obtain this quantitative information for individual crystal faces suggests a pathway to understanding crystal dissolution at the molecular level that can be used to tailor crystal morphology to enhance dose-release properties and regulating bioavailability. More generally, the proposed approach should be widely applicable to a range of crystal types, encompassing organic and ionic crystals.

5. Supporting Information

Table 2.5. Crystallographic parameters for furosemide Polymorph I compared with literature.

	This study	Babu *et al.*[37]
Empirical formula	$C_{12}H_{11}ClN_2O_5S$	$C_{12}H_{11}ClN_2O_5S$
Formula weight	330.74	330.74
Temperature/K	150(2)	100(2)
Crystal system	triclinic	triclinic
Space group	$P\bar{1}$	$P\bar{1}$
a/Å	9.5355(5)	9.5150(9)
b/Å	10.4627(5)	10.4476(10)
c/Å	15.6209(7)	15.5826(16)
α/°	92.936(4)	92.839(2)
β/°	107.105(5)	107.088(2)
γ/°	116.498(5)	116.7470(10)
Volume/Å^3	1302.36(10)	1291.9(2)
Z	4	4
ρ_{calc} g/cm^3	1.648	1.700
m/mm^{-1}	0.425	0.482
Reflections collected	9208	13411
Independent reflections	5166	5061
Goodness-of-fit on F^2	1.045	1.050
Final R indexes [I>=2σ (I)]	$R_1 = 0.0502$	$R_1 = 0.0668$
Final R indexes [all data]	$wR_2 = 0.1069$	$wR_2 = 0.1258$
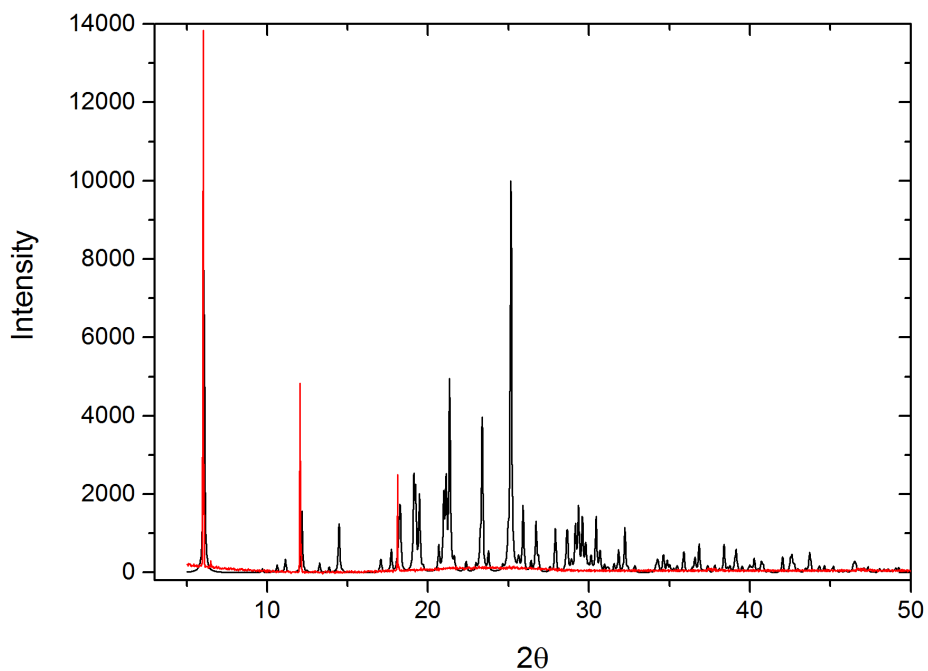
Figure 2.8. Calculated powder X-ray diffraction pattern of furosemide form I (black) and experimental (red) obtained for furosemide crystals mounted on a glass slide (λ = Cu-Kα, 0.1541 nm). The experimentally observed peaks at 2θ = 6.04°, 12.15° and 18.17° correspond to the (001), (002) and (003) reflections of polymorph I respectively, confirming the orientation of the raft-like crystals parallel to the glass slide.

Table 2.6. Comparison of the optimized furosemide unit cell parameters calculated using the COMPASS, Dreiding and cvff force fields and the experimental data obtained by single crystal CCD X-ray diffraction.

	Energy	*Unit cell parameters*					
	(kcal mol^{-1})	a (Å)	b (Å)	c (Å)	A (°)	β (°)	γ (°)
Experimental		9.5355	10.4627	15.6209	92.9360	107.1050	116.4980
COMPASS	-508.1135	9.8589	10.1926	14.7867	94.4689	106.0592	114.7914
Dreiding	-222.3405	9.7441	10.6284	15.6670	96.8028	108.2709	114.6225
cvff	-8.6023	10.3754	10.9100	15.8328	85.1591	110.7729	127.0457
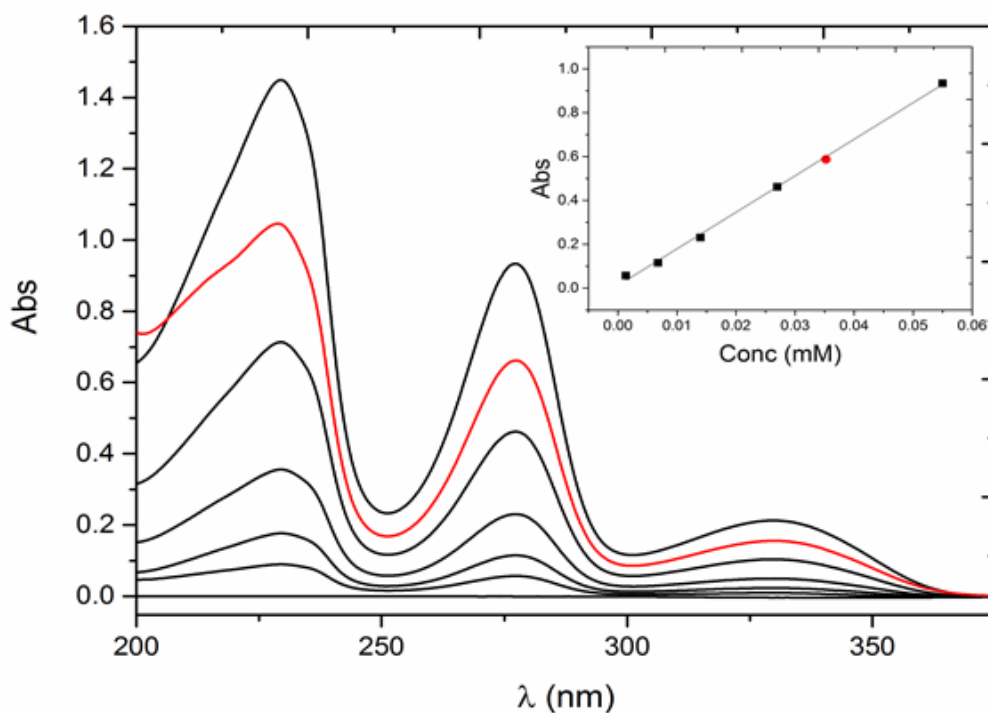
Figure 2.9. UV–Vis spectra of furosemide dissolved in water at different concentrations. Black lines show the UV–Vis spectra of furosemide in water at 0 mM, 0.0034 mM, 0.0068 mM, 0.014 mM, 0.027 mM and 0.055 mM used for calibration. The red line shows the UV–Vis spectra of a saturated solution of furosemide in water diluted 5 times. The inset shows the linear relationship between the absorbance and the concentration of furosemide at 277 nm. Black squares correspond to the calibration data and the red circle to the 5 times diluted saturated solution of furosemide in water.

Table 2.7. Diffusive fluxes per unit area for each crystal face calculated from finite element simulation of each studied crystal.

Face (hkl)	J_{Obs} (mol m^{-2}s^{-1})	J_{MT} (mol m^{-2}s^{-1})	J_{SK} (mol m^{-2}s^{-1})
($10\bar{1}$)	5.2×10^{-6}	6.3×10^{-6}	Close to diffusion control
(010)	1.5×10^{-6}	5.1×10^{-6}	2.1×10^{-6}
(001)	0.6×10^{-6}	4.1×10^{-6}	0.7×10^{-6}
($10\bar{1}$)	9.2×10^{-6}	8.9×10^{-6}	Close to diffusion control
(010)	7.7×10^{-6}	7.3×10^{-6}	Close to diffusion control
(001)	4.4×10^{-6}	5.7×10^{-6}	Close to diffusion control
($10\bar{1}$)	13.6×10^{-6}	15.9×10^{-6}	Close to diffusion control
(010)	8.9×10^{-6}	12.3×10^{-6}	32.2×10^{-6}
(001)	0.9×10^{-6}	7.3×10^{-6}	1.0×10^{-6}
($10\bar{1}$)	14.5×10^{-6}	12.7×10^{-6}	Close to diffusion control
(010)	9.7×10^{-6}	10.6×10^{-6}	Close to diffusion control
(001)	2.1×10^{-6}	8.3×10^{-6}	2.8×10^{-6}
($10\bar{1}$)	20.3×10^{-6}	15.2×10^{-6}	Close to diffusion control
(010)	6.5×10^{-6}	10.8×10^{-6}	16.3×10^{-6}
(001)	3.6×10^{-6}	7.7×10^{-6}	6.7×10^{-6}
($10\bar{1}$)	15.3×10^{-6}	17.3×10^{-6}	Close to diffusion control
(010)	22.2×10^{-6}	14.3×10^{-6}	Close to diffusion control
(001)	3.7×10^{-6}	8.4×10^{-6}	6.6×10^{-6}

$(10\bar{1})$	18.8×10^{-6}	16.4×10^{-6}	Close to diffusion control
(010)	16.6×10^{-6}	12.0×10^{-6}	Close to diffusion control
(001)	2.4×10^{-6}	6.7×10^{-6}	3.7×10^{-6}
$(10\bar{1})$	17.4×10^{-6}	19.2×10^{-6}	Close to diffusion control
(010)	17.9×10^{-6}	15.5×10^{-6}	Close to diffusion control
(001)	2.8×10^{-6}	6.8×10^{-6}	4.8×10^{-6}
$(10\bar{1})$	30.2×10^{-6}	23.3×10^{-6}	Close to diffusion control
(010)	22.4×10^{-6}	17.0×10^{-6}	Close to diffusion control
(001)	4.9×10^{-6}	11.0×10^{-6}	8.8×10^{-6}

6. References

1.	Chen, J.; Sarma, B.; Evans, J. M. B.; Myerson, A. S. *Cryst. Growth Des.* **2011**, *11*, 887-895.

2.	Vippagunta, S. R.; Brittain, H. G.; Grant, D. J. W. *Adv. Drug Delivery Rev.* **2001**, *48*, 3-26.

3.	Blagden, N.; de Matas, M.; Gavan, P. T.; York, P. *Adv. Drug Delivery Rev.* **2007**, *59*, 617-630.

4.	Fan, C.; Chen, J.; Chen, Y.; Ji, J.; Teng, H. H. *Geochim. Cosmochim. Acta* **2006**, *70*, 3820-3829.

5.	York, P. *Int. J. Pharm.* **1983**, *14*, 1-28.

6.	Hörter, D.; Dressman, J. B. *Adv. Drug Delivery Rev.* **2001**, *46*, 75-87.

7.	Byrn, S. R.; Pfeiffer, R. R.; Stowell, J. G. *Solid-state chemistry of drugs*; SSCI, Inc.: West Lafayette, Ind., 1999.

8.	Carter, P. W.; Ward, M. D. *J. Am. Chem. Soc.* **1993**, *115*, 11521-11535.

9.	Carter, P. W.; Hillier, A. C.; Ward, M. D. *J. Am. Chem. Soc.* **1994**, *116*, 944-953.

10.	Vekilov, P. G.; Monaco, L. A.; Rosenberger, F. *J. Cryst. Growth* **1995**, *148*, 289-296.

11.	Vekilov, P. G.; Ataka, M.; Katsura, T. *J. Cryst. Growth* **1993**, *130*, 317-320.

12.	Malkin, A. J.; Kuznetsov, Y. G.; McPherson, A. *J. Cryst. Growth* **1999**, *196*, 471-488.

13.	Van Driessche, A. E. S.; Otálora, F.; Sazaki, G.; Sleutel, M.; Tsukamoto, K.; Gavira, J. A. *Cryst. Growth Des.* **2008**, *8*, 4316-4323.

14.	Michaels, A. S.; Colville, A. R. *J. Phys. Chem.* **1960**, *64*, 13-19.

15.	Jouyban-Gharamaleki, A.; Dastmalchi, S.; Chan, H.-K.; Hanaee, J.; Javanmard, A.; Barzegar-Jalali, M. *Drug Dev. Ind. Pharm.* **2001**, *27*, 577-583.

16.	Pabla, D.; Akhlaghi, F.; Zia, H. *Eur. J. Pharm. Biopharm.* **2009**, *72*, 105-110.

17.	Jeschke, A. A.; Vosbeck, K.; Dreybrodt, W. *Geochim. Cosmochim. Acta* **2001**, *65*, 27-34.

18.	Unwin, P. R.; Macpherson, J. V. *Chem. Soc. Rev.* **1995**, *24*, 109-119.

19.	Sjöberg, E. L.; Rickard, D. *Geochim. Cosmochim. Acta* **1983**, *47*, 2281-2285.

20.	Sherwood, T. K.; Pigford, R. L.; Wilke, C. R. *Mass transfer*; McGraw-Hill, 1975.

21.   Unwin, P. R.; Barwise, A. J.; Compton, R. G. *J. Colloid Interface Sci.* **1989**, *128*, 208-222.

22.   Mbogoro, M. M.; Snowden, M. E.; Edwards, M. A.; Peruffo, M.; Unwin, P. R. *J. Phys. Chem. C* **2011**, *115*, 10147-10154.

23.   Danesh, A.; Connell, S. D.; Davies, M. C.; Roberts, C. J.; Tendler, S. J. B.; Williams, P. M.; Wilkins, M. J. *Pharm Res* **2001**, *18*, 299-303.

24.   Guo, S.; Ward, M. D.; Wesson, J. A. *Langmuir* **2002**, *18*, 4284-4291.

25.   Li, T.; Morris, K. R.; Park, K. *J. Phys. Chem. B* **2000**, *104*, 2019-2032.

26.   Abendan, R. S.; Swift, J. A. *Cryst. Growth Des.* **2005**, *5*, 2146-2153.

27.   Perry, A. R.; Peruffo, M.; Unwin, P. R. *Cryst. Growth Des.* **2013**, *13*, 614-622.

28.   Prasad, K. V. R.; Ristic, R. I.; Sheen, D. B.; Sherwood, J. N. *Int. J. Pharm.* **2002**, *238*, 29-41.

29.   Macpherson, J. V.; Unwin, P. R. *Prog. React. Kinet.* **1995**, *20*, 185-244.

30.   Macpherson, J. V.; Unwin, P. R. *J. Phys. Chem.* **1994**, *98*, 1704-1713.

31.   Kinnear, S. L.; McKelvey, K.; Snowden, M. E.; Peruffo, M.; Colburn, A. W.; Unwin, P. R. *Langmuir* **2013**, *29*, 15565-15572.

32.   Shekunov, B. Y.; Grant, D. J. W. *J. Phys. Chem. B* **1997**, *101*, 3973-3979.

33.   Hiroshi, K.; Satoru, M.; Yoshihisa, S. *Jpn. J. Appl. Phys.* **1993**, *32*, L1855.

34.   Hansma, P. K.; Drake, B.; Marti, O.; Gould, S. A.; Prater, C. B. *Science* **1989**, *243*, 641-643.

35.   Shevchuk, A. I.; Frolenkov, G. I.; Sanchez, D.; James, P. S.; Freedman, N. *Angew. Chem. Int. Ed. Engl.* **2006**, *45*, 2212-2216.

36.   Chen, C.-C.; Zhou, Y.; Baker, L. A. *Annu. Rev. Anal. Chem.* **2012**, *5*, 207-228.

37.   Babu, N. J.; Cherukuvada, S.; Thakuria, R.; Nangia, A. *Cryst. Growth Des.* **2010**, *10*, 1979-1989.

38.   Nielsen, L. H.; Gordon, S.; Holm, R.; Selen, A.; Rades, T.; Müllertz, A. *Eur. J. Pharm. Biopharm.* **2013**, *85*, 942-951.

39.   Murray, M. D.; Haag, K. M.; black, P. K.; Hall, S. D.; Brater, D. C. *Pharmacotherapy* **1997**, *17*, 98-106.

40.   Pudipeddi, M.; Serajuddin, A. T. M. *J. Pharm. Sci.* **2005**, *94*, 929-939.

41.   Ai, H.; Jones, S. A.; de Villiers, M. M.; Lvov, Y. M. *J. Controlled Release* **2003**, *86*, 59-68.

42.   Garnero, C.; Chattah, A. K.; Longhi, M. *Carbohydr. Polym.* **2013**, *94*, 292-300.

43. Menon, A.; Ritschel, W. A.; Sakr, A. *J. Pharm. Sci.* **1994**, *83*, 239-245.

44. Dolomanov, O. V.; Bourhis, L. J.; Gildea, R. J.; Howard, J. A. K.; Puschmann, H. *J. Appl. Crystallogr.* **2009**, *42*, 339-341.

45. Sheldrick, G. *Acta Crystallogr., Sect. A: Found. Adv.* **2008**, *64*, 112-122.

46. Nadappuram, B. P.; McKelvey, K.; Al Botros, R.; Colburn, A. W.; Unwin, P. R. *Anal. Chem.* **2013**, *85*, 8070-8074.

47. McKelvey, K.; Perry, D.; Byers, J. C.; Colburn, A. W.; Unwin, P. R. *Anal. Chem.* **2014**, *86*, 3639-3646.

48. Novak, P.; Li, C.; Shevchuk, A. I.; Stepanyan, R.; Caldwell, M.; Hughes, S.; Smart, T. G.; Gorelik, J.; Ostanin, V. P.; Lab, M. J.; Moss, G. W. J.; Frolenkov, G. I.; Klenerman, D.; Korchev, Y. E. *Nat. Methods* **2009**, *6*, 279-281.

49. Yang, X.; Liu, X.; Zhang, X.; Lu, H.; Zhang, J.; Zhang, Y. *Ultramicroscopy* **2011**, *111*, 1417-1422.

50. Wilke, C. R.; Chang, P. *AIChE J.* **1955**, *1*, 264-270.

51. Amatore, C.; Pebay, C.; Thouin, L.; Wang, A.; Warkocz, J. S. *Anal. Chem.* **2010**, *82*, 6933-6939.

52. Matsuda, Y.; Tatsumi, E. *Int. J. Pharm.* **1990**, *60*, 11-26.

53. Goud, N. R.; Gangavaram, S.; Suresh, K.; Pal, S.; Manjunatha, S. G.; Nambiar, S.; Nangia, A. *J. Pharm. Sci.* **2012**, *101*, 664-680.

54. Docherty, R.; Clydesdale, G.; Roberts, K. J.; Bennema, P. *J. Phys. D: Appl. Phys.* **1991**, *24*, 89.

55. Berkovitch-Yellin, Z. *J. Am. Chem. Soc.* **1985**, *107*, 8239.

56. Hartman, P.; Bennema, P. *J. Cryst. Growth* **1980**, *49*, 145.

57. Hartman, P.; Perdok, W. G. *Acta Crystallogr.* **1955**, *8*, 521-524.

58. Hartman, P.; Perdok, W. G. *Acta Crystallogr.* **1955**, *8*, 49-52.

59. Punzo, F. *Cryst. Growth Des.* **2011**, *11*, 3512-3521.

60. Hod, I.; Mastai, Y.; Medina, D. D. *CrystEngComm* **2011**, *13*, 502-509.

61. Zhang, C.; Ji, C.; Li, H.; Zhou, Y.; Xu, J.; Xu, R.; Li, J.; Luo, Y. *Cryst. Growth Des.* **2013**, *13*, 282-290.

62. Singh, M. K.; Banerjee, A. *Cryst. Growth Des.* **2013**, *13*, 2413-2425.

63. Zhukov, A.; Richards, O.; Ostanin, V.; Korchev, Y.; Klenerman, D. *Ultramicroscopy* **2012**, *121*, 1-7.

64. Happel, P.; Thatenhorst, D.; Dietzel, I. D. *Sens. Actuators, A* **2012**, *12*, 14983-15008.

65. Chen, C.-C.; Zhou, Y.; Baker, L. A. *ACS Nano* **2011**, *5*, 8404-8411.

66. Chen, C.-C.; Derylo, M. A.; Baker, L. A. *Anal. Chem.* **2009**, *81*, 4742-4751.

67. Momotenko, D.; McKelvey, K.; Kang, M.; Meloni, G. N.; Unwin, P. R. *Anal. Chem.* **2016**, *88*, 2838-2846.

68. Burt, H. M.; Mitchell, A. G. *Int. J. Pharm.* **1981**, *9*, 137-152.

69. Chernov, A. A. *Contemp. Phys.* **1989**, *30*, 251-276.

70. Perry, A. R.; Lazenby, R. A.; Adobes-Vidal, M.; Peruffo, M.; McKelvey, K.; Snowden, M. E.; Unwin, P. R. *CrystEngComm* **2015**, *17*, 7835-7843.

71. Ward, M. D. *Chem. Rev.* **2001**, *101*, 1697-1726.

72. Buller, R.; Peterson, M. L.; Almarsson, Ö.; Leiserowitz, L. *Cryst. Growth Des.* **2002**, *2*, 553-562.

73. Ran, Y.; He, Y.; Yang, G.; Johnson, J. L. H.; Yalkowsky, S. H. *Chemosphere* **2002**, *48*, 487-509.

74. Sangwal, K. *Etching of Crystals: Theory, experiment, and application*; North-Holland Amsterdam: Amsterdam, NL, 1987; Vol. 497.

	Dissolution of Bicalutamide Single Crystals in Aqueous Solution: Significance of Evolving Topography in Accelerating Face-Specific Kinetics
Chapter III	**Dissolution of Bicalutamide Single Crystals in Aqueous Solution: Significance of Evolving Topography in Accelerating Face-Specific Kinetics**

Submitted as an article to Crystal Growth and Design

Abstract

The dissolution kinetics of individual microscale bicalutamide (BIC) form-I crystals are tracked over time using *in situ* atomic force microscopy (AFM), with the evolution of crystal morphology used to obtain quantitative data on dissolution kinetics via finite element method (FEM) modeling of the dissolution reaction-diffusion problem. Dissolution is found to involve pit formation, and roughening on all dissolving surfaces of the BIC crystal and this has a strong influence on the overall dissolution process and kinetics. While all of the exposed faces {100}, {051} and {$\bar{1}$02} show dissolution kinetics that are largely surface-kinetic controlled, each face has an intrinsic dissolution characteristic that depends on the degree of hydrogen bonding with aqueous solution, with hydrogen bonding promoting faster dissolution. Moreover, as dissolution proceeds with pitting and roughening, the rate accelerates considerably, so that there is an increasing diffusion contribution. Such insight is important in understanding the oral administration of poorly soluble active pharmaceutical ingredients (APIs) in crystal form. Evidently, surface roughening and defects greatly enhances dissolution kinetics, but the evolving crystal topography during dissolution leads to complex time-dependent kinetics that are important for modeling and understanding API release rates.

1. Introduction

Many active pharmaceutical ingredients (APIs) are administered as solid oral formulations,[1] and the resulting *in vivo* bioavailability is governed by properties such as solubility, permeability, and formulation components, as well as physiological variables. As formulations often include APIs in microcrystalline format, strong dependency of API bioavailability on the dissolution rates of the API crystals has been recognized[2-4] and, consequently, dissolution measurements are a key procedure in drug testing and quality control of pharmaceutical products.[5,6] Interestingly, there is an increasing trend towards the use of poorly water soluble compounds as candidates for the development of new drugs,[7] and a comprehensive understanding of the dissolution process of these crystalline APIs is thus of fundamental importance.

The dissolution of a crystal is a complex physicochemical process driven by local undersaturation at the crystal/solution interface, and consisting of a series of elementary steps involving various surface reactions and mass transport.[8] The slowest step(s) governs the overall rate and at the simplest level dissolution kinetics can be classified as either surface-controlled (surface processes limit the rate), mass transport-controlled (surface processes are faster compared to diffusion of API molecules from the crystal to bulk solution) or under a mixed regime system, where surface processes and mass transport contributions to the kinetics are comparable. The dissolution process is further complicated when the nature of a molecular crystal surface is considered in more detail. The different arrangement of molecules at different exposed crystal faces and the surface microstructure of those faces (steps, terraces and kinks) make crystal surfaces energetically heterogeneous.[9,10] The dissolution rate will depend on the energetics associated with each type of site on each surface,[11-14] and their contributions and interactions greatly complicate the understanding of the dissolution processes (kinetics and mechanism).[13,15] Experimental studies need to provide an holistic view of the impact of surface morphology, surface reactivity, driving force and mass transport on dissolution kinetics.[16]

Traditional dissolution testing methodologies for APIs are based solely on measuring bulk solution concentration of a dissolving suspension of a particulates as a function of time.[17,18] These approaches give average dissolution rates of a population of

crystals but do not provide any information about the contribution of the individual crystal faces or the micromorphology changes during the dissolution process.[19-21] Furthermore, difficulties in the quantification of mass transport in such systems impedes the elucidation of the driving force for dissolution (undersaturation at the crystal/solution interface).

The use of scanning probe microscopy methods such as atomic force microscopy (AFM),[8,22-24] or scanning ion conductance microscopy (SICM),[25] among others,[26,27,28] has provided detailed kinetic and structural information of dissolution processes. The study of microcrystals by these techniques is particularly advantageous, as this configuration offers high diffusional mass transport rates between the crystal and bulk solution and the possibility of mapping the behavior of entire crystals and the different faces exposed.[25] Furthermore, this approach allows the ready combination of experimental data with numerical simulations of mass transport and surface kinetics, making it possible to determine concentration gradients and interfacial concentrations, so as to quantify the dissolution kinetic regime.

The microcrystal approach is adopted herein, using a combination of *in situ* AFM imaging data and finite element method (FEM) simulations, to probe face-specific dissolution of bicalutamide (BIC) (Scheme 3.1) crystals as a function of time. BIC is the API in AstraZeneca's product CASODEX[®29] and belongs to class II of the biopharmaceutics classification system (BCS) (low solubility and high permeability). It is used to prevent the growth of prostate cancer by blocking the action of androgens on the cancer cells.[29-31] The low solubility/dissolution rate of BIC is a major limiting factor for its bioavailability and clinical applications. Accordingly, an in-depth understanding of the microscopic dissolution process in aqueous solution at the single crystal level is expected to be important in leading to new formulation strategies that would enhance its bioavailability. The approach we outline herein could be generally powerful for revealing the dissolution kinetics of class II API crystals.
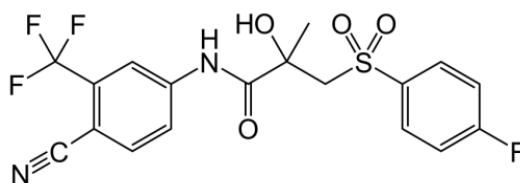
Scheme 3.1. Molecular structure of bicalutamide.

2. Experimental

2.1 Samples and Solutions

All chemicals were used as received. Aqueous solutions were prepared using high purity water (Purite, Select HP) with a resistivity of 18.2 MΩ cm at 25 °C. BIC was supplied by AstraZeneca. BIC crystals were grown by mixing 200 μL of a 10 mM solution of BIC dissolved in a mixture of ethanol (≥ 99.5%) and dimethyl sulfoxide (≥ 99.9 %) in 5:1 v/v ratio (solvent) with 400 μL of water (antisolvent) in a plastic petri dish (Willco Well) to create a supersaturated solution. The solution was allowed to stand under a closed environment for 15 min. The supernatant was then removed to reveal plate-like crystals, with the largest dimension in the range 10-60 μm, attached to the petri dish base. The crystals were then rinsed briefly with ultra-pure water and dried using nitrogen (BOC).

2.2 X-ray Characterization

Single crystal X-ray analysis was used to determine the unit cell of the grown crystals. A large crystal (100 μm in length, grown for ~1 hour) was mounted on a Mitegen loop with silicone oil and placed on an Oxford Diffraction Xcalibur Gemini diffractometer fitted with a Ruby CCD area detector. The crystal was kept at 293(2) K during data collection. Using Olex2,[32] the structure was solved with the ShelXS-2013[33] structure solution program using Direct Methods and refined with the ShelXL[34] refinement package using least squares minimization. The face indexing was performed using CrysAlis PRO (Agilent Technologies UK Ltd.). Powder X-ray diffraction analysis was executed at room temperature using Panalytical X'Pert Pro MPD with hybrid monochromator to give pure CuKα_1 radiation (1.541 Å). The bottom of the petri dish containing the crystals was cut and placed on the sample holder. A Pixcel detector was used in scanning mode over the range 5° < 2θ < 30°, stepping 0.02° over a period of 45 min.

2.3 *In situ* Atomic Force Microscopy

Dissolution investigations were performed in 2 mL of unstirred pure water (sink conditions) directly in the petri dish containing the crystals, as grown, using a Bioscope Catalyst microscope with a Nanoscope V controller (Veeco). AFM images

of selected diffusionally isolated crystals (~ 35 μm in length; separated from neighboring crystals by >20 times this distance) were acquired in *ScanAsyst* mode using silicon-tips on a silicon nitride lever with a spring constant of 0.35 Nm^{-1} according to manufacturer (SNL-10, Bruker). The images were obtained at a scan rate of 0.45 Hz and the temperature was *ca.* 20 °C. Dissolution rates were measured from consecutive frames acquired at ~10 min per frame with a resolution of 256 lines and 512 samples per line. Images acquired were analyzed using SPP 6.0.14 software, where a first order plane correction was applied making sure the crystal was masked out to correct any background tilt.

2.4 Simulations

Numerical simulations were performed on a Dell Intel core 7i Quad 2.93 GHz computer, equipped with 16 GB of RAM running Windows 7 Professional x64 bit edition using the commercial FEM modelling package Comsol Multiphysics 4.2a (COMSOL AB, Sweden). The "mass transport of diluted species" module was used in the 3D domain illustrated in Figure 3.1 to simulate the mass transport of BIC dissolution during the *in situ* AFM experiments. The models were defined using experimental data that included changes in both the crystal morphology and dissolution rates at specific dissolution times. Calculations employed >12000 tetrahedral mesh elements and resolution was defined to be finest near the surface of the crystal. Solution of the partial differential equations for each model was achieved using the direct solver MUMPS in the COMSOL environment with a relative error tolerance of 10^{-6}.
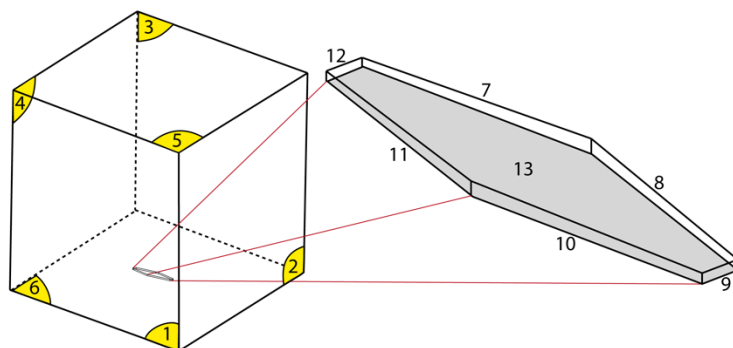
Figure 3.1. Three-dimensional domain (not to scale) used for FEM simulations of BIC dissolution. The numbers correspond to the boundaries described in Table 3.1.

For the experimental length scale, mass transport is predominantly by diffusion. The diffusion time can be estimated using a semi-infinite diffusion model according to equation 3.1, where t_{diff} is the steady-state diffusion time, d is crystal largest dimension length and D denotes diffusion coefficient.

$$t_{diff} \approx d^2 / D \qquad\qquad (3.1)$$

The diffusion coefficient of BIC molecules in aqueous solution ($D = 4.5 \times 10^{-6}$ cm^2 s^{-1}) was calculated using the Wilke-Chang equation (eq. 2.2) which provides diffusivities with an absolute error no bigger than 11%, [35] a level that did not have a major impact on our final results. FEM simulations taking into account the upper and lower limit of the diffusion coefficient calculated from the Wilke-Chang correlation showed that the absolute error in the calculation of the solute concentration near the crystal/solution interface and the flux of solute from each individual crystal face was < 11%, a precision that was sufficient not to affect our conclusions about the kinetic regime. For the dilute solutions during dissolution, D was assumed constant over the entire domain. The characteristic diffusion time for a dissolving crystal (~35 μm in length) is about 3 s, which is about 4 orders of magnitude faster than the duration of a typical dissolution experiment (6 h). Mass transport by diffusion was therefore assumed to be at a steady-state, for particular AFM snapshots, and the flux conservation equation (eq 3.2) was solved, where J is the flux and C is the concentration of the BIC solute.

$$\nabla J = -D\nabla^2 C = 0 \qquad\qquad (3.2)$$

Four different geometric models were developed that mimicked the main crystal morphologies found during dissolution. For each model, the experimental data of face displacement velocity allowed the flux (per unit area) for each crystal face, $J_{\{hkl\}}$,[13] to be defined. These form the boundary conditions on the crystal surface which, together with the remaining boundary conditions (Table 3.1), allowed equation 3.1 to be solved to obtain the concentration of BIC in the solution around the dissolving crystal. These simulation data allowed evaluation of the dissolution regime, i.e., mass transport vs. kinetic control, as a function of time. In order to deduce the relative importance of mass transport and surface kinetics, two additional sets of models with the same geometry but different boundary conditions were employed (Table 3.1),

such that dissolution of all the crystal faces was controlled by diffusion (crystal/solution interface saturated with soluble BIC), denoted MT1 models, or where only the small and fast dissolving crystal faces {051} and {$\overline{1}$02} were controlled by diffusion, denoted MT2 models

Table 3.1. Boundary conditions applied to the numerical models as defined in Figure 3.1, where n denotes the outward vector normal to the boundary, t denotes dissolution time, C_{bulk} is the bulk concentration (0 µM) and C_{sat} is the saturation solubility of 11.6 µM

Boundary	Experimental conditions	MT1 conditions	MT2 conditions
1-5	$C = C_{bulk}$	$C = C_{bulk}$	$C = C_{bulk}$
6	$\mathbf{n} \cdot (D\nabla C) = 0$	$\mathbf{n} \cdot (D\nabla C) = 0$	$\mathbf{n} \cdot (D\nabla C) = 0$
7, 8, 10, 11	$\mathbf{n} \cdot (D\nabla C) = -J_{\{051\},t}$	$C = C_{sat}$	$C = C_{sat}$
9, 12	$\mathbf{n} \cdot (D\nabla C) = -J_{\{\overline{1}02\},t}$	$C = C_{sat}$	$C = C_{sat}$
13	$\mathbf{n} \cdot (D\nabla C) = -J_{\{100\},t}$	$C = C_{sat}$	$\mathbf{n} \cdot (D\nabla C) = -J_{\{100\},t}$

3. Results and Discussion

3.1 Bicalutamide Crystals

The solid form of BIC presents polymorphism, which has been thoroughly characterized by Vega *et al.*[29] Two crystalline forms (I and II) and an amorphous phase of solid BIC have been reported. Single crystal CCD X-ray diffraction determined that the crystallization method described herein produced polymorph I, which is the most stable form, characterized by the monoclinic $P2_1/c$ space group (Supporting Information, Table 3.2). Optical microscopy revealed the crystals had a plate-like crystal habit, as shown in Figure 3.2a. The orientation of the crystals grown in the plastic petri dish was determined by powder X-ray diffraction. Only peaks corresponding to the (*h00*) reflections (*h*=1-4) were observed, indicating that the crystals were oriented with the {100} faces parallel to the surface (Supporting information, Figure 3.8). The remaining faces were determined by single crystal X-ray diffraction taking into account the specific angles of the crystal faces. The (*hkl*) indexes assigned to each crystal face are presented in Figure 3.2b.
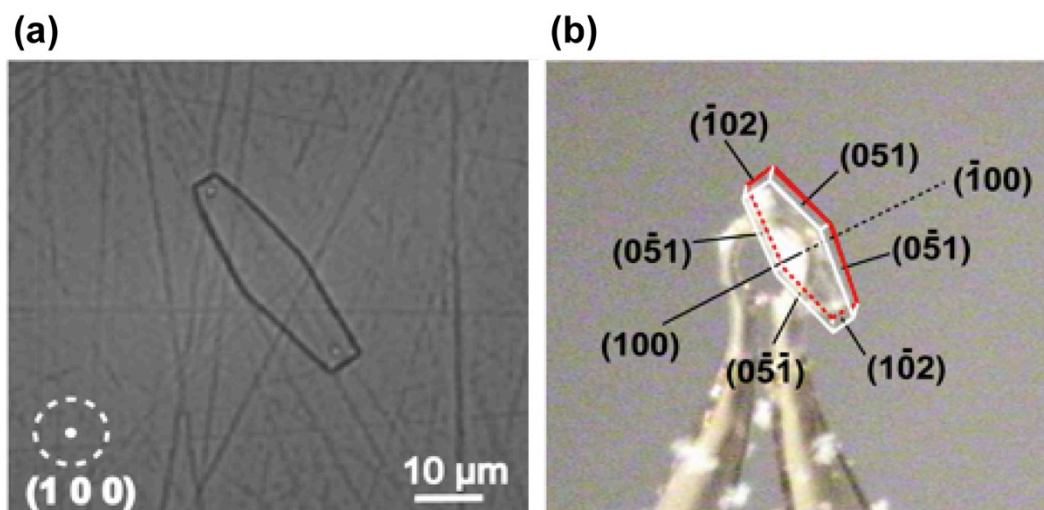
Figure 3.2. Crystal morphology of BIC (Form I). (a) Bright field microscopy image of a typical grown crystal acquired normal to the (100) face. (b) Representation of the single crystal X-ray diffraction of BIC with crystal faces assigned. Red line represents the 2D crystal outline.

3.2 Dissolution Rates and Surface Dynamics

Herein, the aqueous dissolution kinetics of microscopic BIC single crystals has been studied by AFM imaging in quiescent conditions. Only a few crystals were present in the petri dish (< 20). Considering the volume of the crystals and the molar volume of bicalutamide ($V_{m(BIC)}$ = 3601.572 mol m^{-3}), the bulk concentration would only reaches *ca.* 0.003 μM after all the crystals had been dissolved. As such, we consider pure sink conditions during the time course of our experiment.. As discussed in the introduction, visualization of the morphology changes of an entire single crystal during dissolution allows the assessment of the dissolution rates of individual crystal faces, providing information on the evolution of surface structure and dissolution activity.[36] Additionally, the use of microcrystals generates fast and well-defined mass transport that can be modeled, enabling the quantification of the relative contributions of mass transport and surface kinetics to observed dissolution rates. ScanAsyst mode[37] was chosen to operate at very low forces, which minimized tip/sample interactions while enabling high resolution images to be obtained. Additionally, in order to determine if the AFM probe had an effect on dissolution kinetics, dissolution studies of diffusionally isolated BIC single crystals of similar size were performed by optical microscopy (optical data not shown due to the resolution limits of optical microscopy). The total dissolution time measured by optical microscopy was broadly comparable to that determined by AFM such that it was possible to discard AFM tip

effects promoting the dissolution of the crystals. Other possible effects of the AFM probe on the mass transport of species diffusing from the crystal surface to bulk solution were also considered. As shown in previous work,[38-40] the AFM tip can block the diffusion of solute and affect the elucidation of the kinetic regime, especially when the crystal dissolves under a mixed kinetic regime and a very small area of the crystal surface is imaged. However, in the case reported in this work, FEM results show that the dissolution of BIC crystals, in particular the (100) face, is strongly controlled by surface kinetics and small changes in the mass transport of BIC due to the AFM probe can be neglected. Moreover, the whole crystal is imaged by the AFM probe, allowing the natural mass transport behavior of the system to be quickly recovered when the tip moves laterally a few microns, as shown in other works that studied the influence of AFM probe position and geometry on diffusion to ultramicroelectrodes in an in-situ AFM environment.[41]

Measurements were made on different crystals, and although there were some subtle differences between them, the phenomena observed and the time course of dissolution was broadly similar. We thus describe the data in detail for one crystal and provide example data for three additional crystals in Supporting Information, Figures 3.9-3.11.

Figure 3.3 (a) presents time-dependent 3D AFM images of a dissolving BIC microcrystal in aqueous solution. In the early stages, AFM measurements show the formation of pits on the top surfaces, as well as roughening of the side faces. The dissolution velocity of the {100} faces was followed by tracking the changes in the average crystal height over the entire crystal area as a function of time, whereas the dissolution velocities of the {051} and {$\overline{1}$02} faces were determined from the perpendicular retreat of the faces as referenced in Figure 3.3b. The mean of the 2 cross-sectional lines, forming right angles between parallel {051} faces, as shown in Figure 3.3b, was used as the average width. The mean of 9 cross-sectional lines along the direction labeled as length in Figure 3.3b was used to extract the average length of the crystal at each frame. Measurements were extracted for all dimensions until the dissolution time reached 240 min. Within this time range, measurements could be made with good certainty, since the crystal showed a well-defined morphology. Figure 3.3c plots the displacement behavior in the length and width dimensions. The displacement slope of the {$\overline{1}$02} faces (length) is steeper than the {051} faces (width),

indicating faster dissolution rate. The increase in rate with time can be understood from visual analysis of the AFM images, showing that the initiation and propagation of pits, and face roughening, over time have a great impact on the rate at which the BIC crystal faces dissolve.
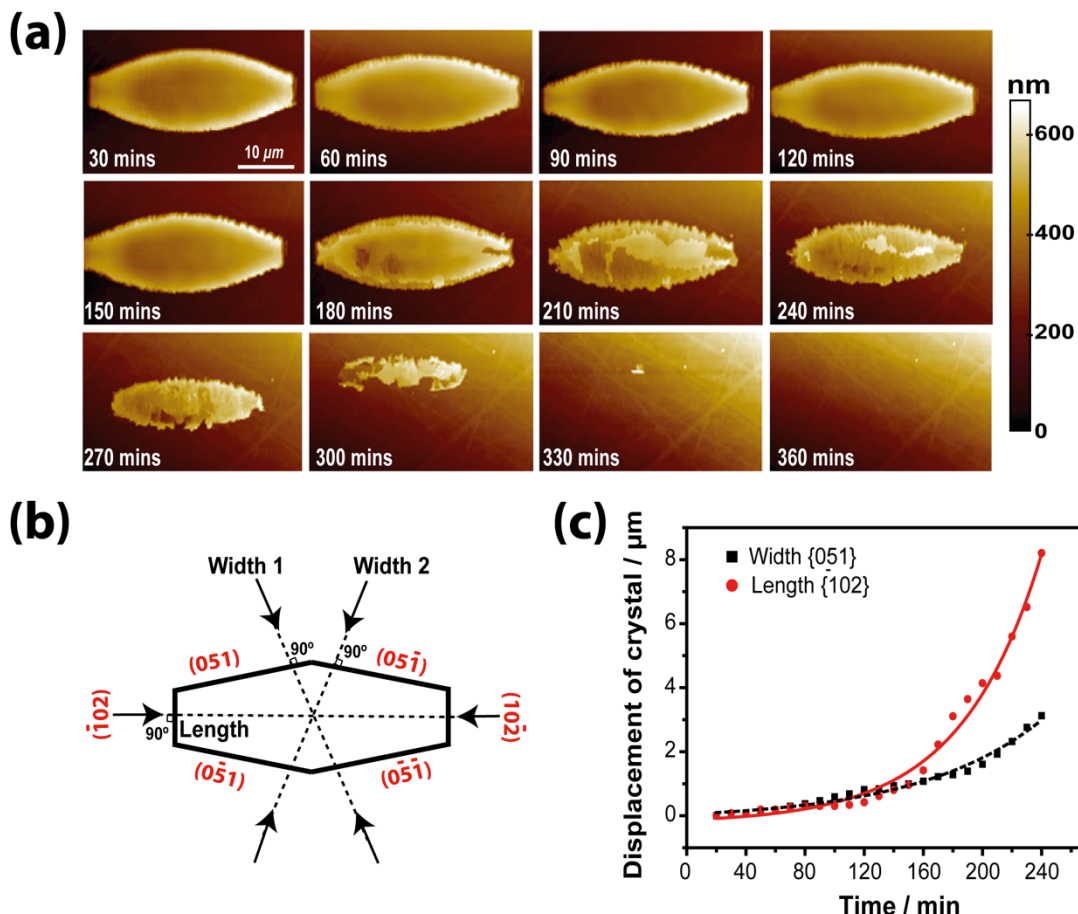
Figure 3.3. (a) AFM images of a single BIC microcrystal (initially 36 μm in length and 10.5 μm in width) during dissolution in aqueous solution. (b) 2D BIC crystal morphology indicating how displacement data were extracted. (c) Plot showing the changes in width and length over time of the dissolving BIC crystal shown in (a).

The overall displacement of the {100}, {051} and {$\overline{1}$02} faces with time fit well to an exponential function (Figure 3.4a). Data were fitted empirically to such a function (eq 3.3) to yield the best R^2 value included in the software OriginPro 9.1.0.

$$y = A(1 - \exp^{-Bx})$$ (3.3)

The best linear fits in the early and late time period are shown by the blue dotted lines. Molar dissolution rates of the individual crystal faces, $J_{(hkl)}^{obs}$, were determined directly

from the data in Figure 3.4a using equation 3.4, where $v_{(hkl)}$ is the dissolution velocity of the $\{hkl\}$ face and $\overline{V}_{BIC}$ is the molar volume of BIC calculated from the density of the BIC polymorph (1.55 g cm^{-3}).

$$J_{(hkl)}^{obs} = v_{(hkl)} \cdot \overline{V}_{BIC} \qquad\qquad (3.4)$$
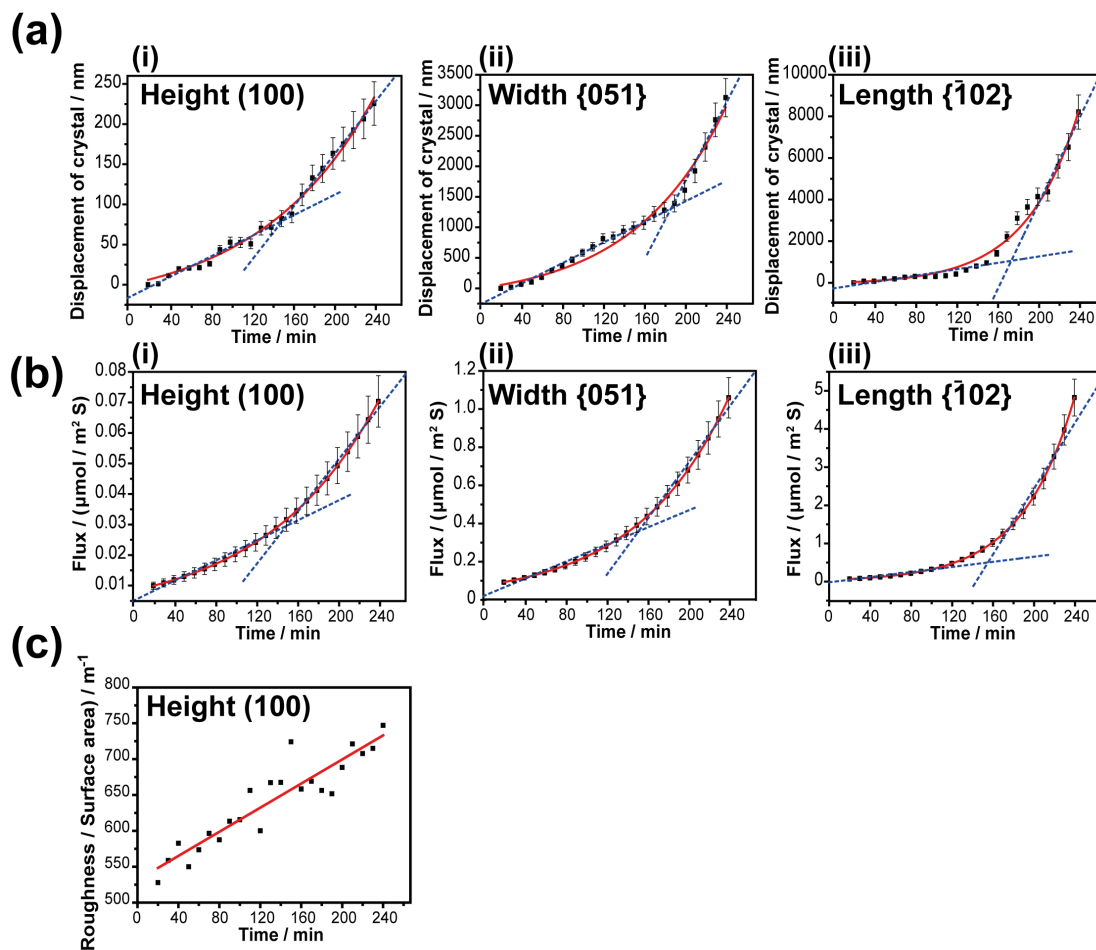
Figure 3.4. (a) Plots showing changes in crystal dimensions over time: (i) Height {100}, (ii) Width {051} and (iii) Length {$\bar{1}$02}. (b) Corresponding dissolution rates (flux) over time: (i) Height {100}, (ii) Width {051} and (iii) Length {$\bar{1}$02}. Data are fitted to an exponential function (solid red curves) and the blue linear portions highlight the change in the rate for the basal surface and roughened surfaces are at early and advanced dissolution times (c) Plot showing the change in surface roughness of {100} face normalized by the geometric surface area as a function of time.

The slowest dissolution rate was found to be for the {100} face. The dissolution rates of the {051} and {$\bar{1}$02} faces were faster, but both increased markedly with time (Figure 3.4b (ii-iii)). As alluded to above, these changes are mainly associated with

changes of the crystal surface energy, due to the evolving face topography, although a decrease in crystal size also leads to higher diffusion rates which serves to increase the dissolution rate of this mixed surface kinetic-diffusion dissolution system (*vide infra*).

Further insight into the dissolution process was obtained by conducting an analysis of the relationship between dissolution rate and surface roughness, as determined by AFM, normalized by the changes in geometric surface area as a function of time (Figure 3.4c). This procedure is most accurate for the top {100} face because full images of the surface are obtained in detail. It can be seen that surface area-normalized roughness increases by less than a factor of two, yet the rate of reaction over this time period increases by a factor of six. Although AFM may not provide a view of atomic-scale defects, it appears that the rate is not simply proportional to surface roughness. Rather as dissolution proceeds, sites of higher reactivity, including high-index nanofacets, are produced which accelerate the reaction.

The roughness of the {051} and {$\overline{1}02$} faces is more difficult to quantify, but it can be seen from Figure 3.4a (ii) and (iii) and 3.4b (ii) and (iii) that the dramatic increase in rate is far more extensive than could be explained from the roughening of the crystal side faces (Figure 3.3a) Indeed, these images highlight the formation of high index faces (manifested as indents) around the crystal perimeter.

Initially, the crystal faces are relatively flat (low step edge and kink density), so the overall activation energy for dissolution tends to be larger.[42] The data presented indicate that as dissolution proceeds, the crystal surface roughens, the edges become rounded and new crystal faces of higher crystallographic indexes are exposed to the solvent (Supporting Information, Figure 3.12). Etch-pits produced on the {100} face, imaged directly by AFM (Figure 3.3a), show that the distribution is non-uniform and etch-pits do not present a particular crystallographic orientation. All the crystal faces present high-degree of surface etch-pitting at long dissolution times, which explains the slope difference in the two linear regions of all plotted dissolution rates versus time, in Figure 3.4b, and the newly exposed reactive sites cause the increase in the dissolution rate.[43, 44] As further shown in the Supporting Information, Figures 3.9-3.11 all examined BIC crystals dissolved at different rates despite their similarity in size (~50-60 μm in length). This is attributed to the different crystal surface

characteristics, such as the number and type of defects in each crystal, which increasingly lead to the emergence of high index faces on dissolution kinetics at longer times. The creation of reactive dissolution sites is considered to be an indicator of surface-controlled dissolution,[9,10,13] but to confirm the kinetic regime, the determination of the solute concentration near the crystal/solution interface and the quantification of the surface reactivity and diffusion contributions to the dissolution process is necessary (*vide infra*). These observations build on recent dissolution kinetics measurements of salicylic acid in aqueous solution using hopping intermittent contact scanning electrochemical microscopy[27] and the aqueous dissolution of the organic crystal furosemide, studied in chapter II, using the combination of scanning ion conductance microscopy and optical microscopy.[25] Both studies highlight the strong influence of evolving surface roughness on the overall dissolution kinetics time-course.

The face-specific dissolution rates at the beginning of the dissolution process corresponds to the dissolution of the {100}, {051} and {$\overline{1}02$} faces presented in the initial crystal habit. As highlighted above, crystal surface energy has a huge impact on the overall dissolution rate, and this was examined, as shown in Figure 3.5 (generated using the unit cell parameters of the crystal structure JAYCES[29] available in the CCDC and using the commercial package Mercury 3.8, CCDC Cambridge[45]). Considering the (100) face presented in Figure 3.5a, the hydrogen bonding network is contained within the (100) plane with the exposure of fluorobenzene rings at the surface. This is the characteristic of a face with a low surface energy and slow growth.[46] In contrast, the ($\overline{1}02$) face structure (Figure 3.5b) exposes a sulphonyl group at the surface and results in a hydrogen bonding network perpendicular to the ($\overline{1}02$) plane, making the ($\overline{1}02$) face a high energy surface. This behavior is also seen in the (051) face, although to a smaller extent compared to the ($\overline{1}02$) face, highlighted by the exposure of trifluoromethyl benzonitrile groups at the surface and the zig zag arrangement of the hydrogen bonds along the structure shown in Figure 3.5c. The order of the measured dissolution rates (Figure 3.4b) of the different faces: {100} < {051} < {$\overline{1}02$}, agrees with the hydrogen bonding model, i.e. the greater the degree of hydrogen bonding between the surfaces and adjacent solution, the faster the dissolution kinetics. It is reasonable to assume that the relative dissolution rates of the

different faces for this period of time would mirror the order of the attachment energies of BIC molecules to the surface, as would occur during crystal growth, and as found in our previous work on furosemide.[25]
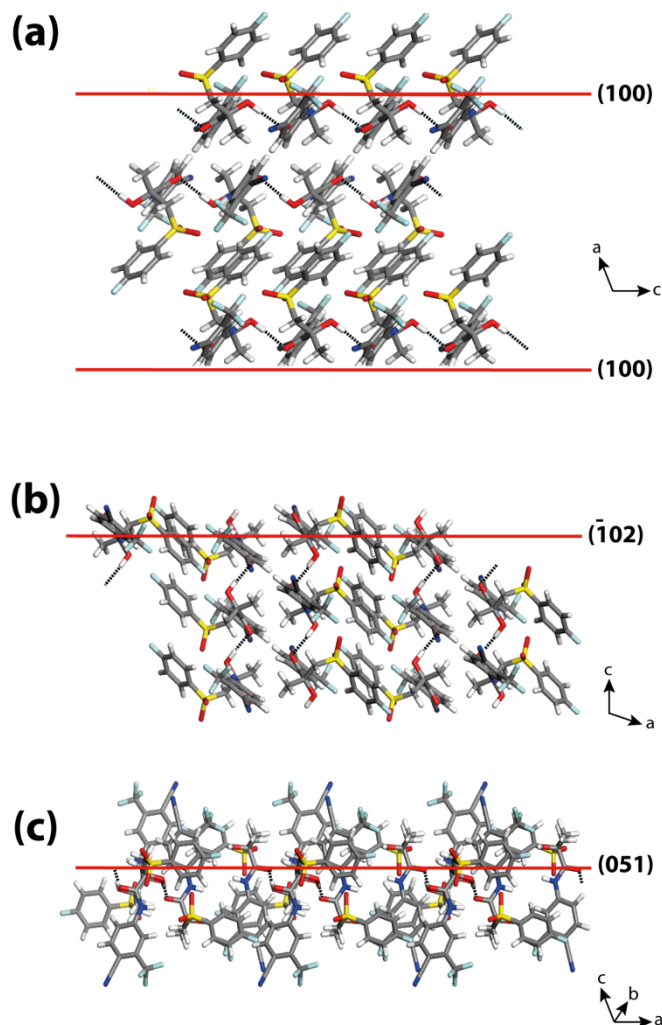
Figure 3.5. Stucture of BIC crystal faces: (a) (100), (b) ($\bar{1}$02) and (c) (051). Black dotted lines highlight hydrogen bonds.

3.3 Determination of Interfacial Concentrations and Kinetic Regime

In the case of a mixed surface kinetic-diffusion regime, the concentration of solute molecules near the crystal surface has an intermediate value between close to bulk concentration (pure kinetic control) and equilibrium (saturated) value (diffusion control). The actual value depends on the relative contributions of mass transport and surface kinetics.[40] To elucidate how the kinetic regime during the dissolution of BIC crystals evolves with time, the concentration of BIC solute near the crystal/solution

interface during dissolution was calculated by FEM simulations formulated directly from AFM experimental data.

Because the crystal size, morphology and dissolution rates of the individual crystal faces are time-dependent, four different steady-state FEM models at different dissolution times were formulated to evaluate the evolution of the kinetic regime with time. The computations used the experimental dissolution rates determined for each crystal face and the crystal size and morphology determined from AFM images at each dissolution time (20 min, 80 min, 170 min and 240 min). The crystal morphology was approximated to smooth surfaces, i.e. to the underlying basal surface, considering the difficulty of constructing and assigning overall dissolution rates to rough surfaces in the FEM modeling package. The results of the FEM calculations (Figure 3.6a) revealed that $C_{int\ \{\bar{1}02\}} > C_{int\ \{051\}} > C_{int\ \{100\}}$ during the whole dissolution process, and that all the $C_{int\ \{hkl\}}$ values increase with time consistent with the kinetic coefficient for dissolution increasing as dissolution proceeds. At the beginning, $C_{int\ \{hkl\}}$ is very similar to the bulk concentration. This is consistent with a dissolution process controlled by surface kinetics in which the rate of the surface reaction is much slower than the rate of surface to bulk diffusion. As dissolution proceeds, AFM imaging indicates that more reactive sites are formed and surface dissolution kinetics increase, leading to higher $C_{int\ \{hkl\}}$. Consequently, concentration gradients from the crystal to bulk solution become steeper, indicating an increasing contribution from diffusion. However, surface kinetics still dominate, since $C_{int\ \{hkl\}}$ is well below the equilibrium concentration value (11.62 µM, at 20 °C)[47] during the entire dissolution process (Supporting Information, Table 3.4).

To evaluate the relative contributions of mass transport and surface kinetics on dissolution, these results were compared to those obtained from FEM calculations parameterized for the same crystal size and geometry at each dissolution time, but where a pure mass transport controlled dissolution regime was imposed at specific crystal faces, $C_{int\ \{hkl\}} = C_{sat}$, (Figure 3.6b-c). It can be seen that the surface concentration is much larger when dissolution is diffusion controlled. A first comparison of Figure 3.6a and Figure 3.6b indicates how the experimental system evolves towards increasing diffusion control with time. This is also highlighted in Figure 3.7, which shows plots of the ratio of diffusion to experimental fluxes (J_{MT}/

J_{obs}) for the different faces versus time. J_{MT1} is the predicted flux for a process where the dissolution of all the crystal faces is purely diffusion-limited and J_{obs} is the measured flux. During the early stages, the dissolution rates of the BIC crystal would be at least two orders of magnitude higher if dissolution of all the crystal faces was limited by diffusion (MT1 model). Whereas at later stages, the magnitude of the experimentally obtained fluxes tend towards those calculated for a pure diffusion-limited system (Supporting Information, Table 3.4), particularly for the $\{10\overline{2}\}$ faces, which are those that dissolve the fastest. It is important to note, that the flux magnitude is strongly influenced by the crystal morphology and size, and under mixed kinetic control, the crystal geometry and the BIC concentration at adjacent crystal faces. In the MT1 model, the concentration of BIC near all the crystal faces is c_{sat}, an extreme situation that does not take into account the acute anisotropic kinetic character for dissolution of the different (hkl) crystal faces observed experimentally (different balance between mass transport and surface kinetics for each family of faces, *vide supra*). Under mixed kinetic control, the flux of solute molecules arising from the most morphologically important face, the (100) face, affect the apparent behavior of the very small adjacent faces. To illustrate this point, a third set of models where only the dissolution of the $\{051\}$ and $\{10\overline{2}\}$ faces was forced to be diffusion-limited and the slow dissolving large basal (100) face behaved as observed experimentally, were formulated (MT2). In this situation, the calculated molar flux of BIC, J_{MT2} at the $\{051\}$ and $\{10\overline{2}\}$ faces is much higher than that calculated by MT1 for each dissolution time (Figure 7). The kinetic regime of these smaller faces is then in good agreement when comparing either concentrations near the crystal/solution interface or flux of material (J_{MT2}/ J_{obs}) (Supporting Information, Table 3.4. Further, through this model, one can even appreciate the effect of the influence of the concentration near the $\{051\}$ and $\{10\overline{2}\}$ faces on the calculation of $c_{surf, (100)}$. This is observed to be enhanced compared to that calculated in the experimental model, despite the fact that the flux applied was the same in each case, $J_{obs,(100)} = J_{MT2,(100)}$ (Supporting Information, Table 3.4).
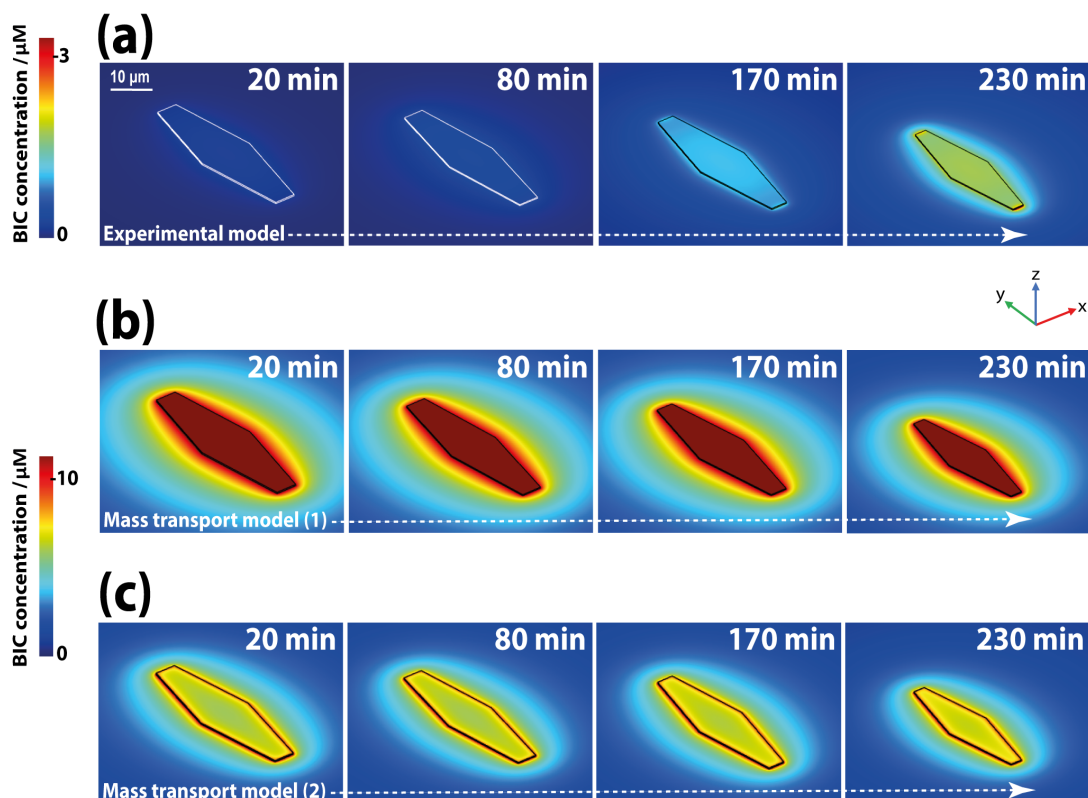
Figure 3.6. FEM simulation for the dissolution of BIC in bulk aqueous solution at different time points: (a) model formulated from experimental data. (b) MT1 model where the dissolution of all faces is purely diffusion-controlled, and (c) MT2 model where only the {051} and {$\bar{1}$02} faces are diffusion-controlled and the (100) face dissolves as observed experimentally. Note the difference in the concentration ranges for (a) and (b-c).
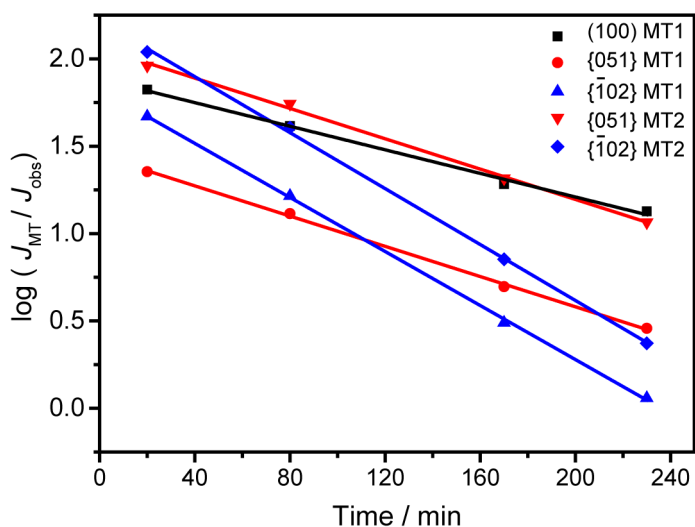
Figure 3.7. Comparative plots of J_{MT}/J_{obs} versus time for the (100) faces (black), {051} faces (red) and {$\bar{1}$02} faces (blue), showing the extent to which each face evolves towards increasing mass transport contribution during dissolution in the case where all the crystal faces are diffusion-limited (MT1) and where only the {051} and {$\bar{1}$02} faces are diffusion-limited (MT2).

4. Conclusions

In this study, the combined use of *in situ* AFM measurements and FEM modeling has allowed the surface processes that accompany dissolution to be monitored quantitatively in real-time to obtain dissolution kinetics for individual faces of a single BIC microcrystal. Morphological changes and the formation of pits associated with surface-controlled dissolution were observed. At longer dissolution times the roughening of individual crystal faces and the exposure of high index faces result in greatly increased dissolution kinetics. Incorporating AFM experimental data into a FEM model of a dissolving BIC microcrystal has provided direct concentration distributions at individual crystal faces. As a result, we were able to determine the importance of surface kinetics compared to mass transport for each crystal face. All BIC crystal faces showed significant surface kinetic-controlled dissolution behavior, being far from the mass transport limited regime, but with increasing mass transport (diffusion) contribution to the kinetics as the reaction proceeded.

The study of single microcrystals provides considerable understanding of API crystal dissolution kinetics and could provide strategic insight for the future engineering of drug crystals with appropriate dissolution characteristics whilst maintaining suitable physical and chemical stability. For example, these studies have shown that roughened and defect-rich surfaces have greatly enhanced dissolution kinetics. Further, the significant time-dependence of the dissolution kinetics is important for improved pharmacokinetic modeling.

5. Supporting Information

Table 3.2. Crystal data and structure refinement for BIC

Parameter	Value
Identification code	BIC
Empirical formula	$C_{18}H_{14}F_4N_2O_4S$
Formula weight	430.37
Temperature/K	296(2)
Crystal system	monoclinic
Space group	$P2_1/c$
a/Å	14.9237(5)
b/Å	12.2149(3)
c/Å	10.4612(3)
$\alpha/°$	90
$\beta/°$	104.668(3)
$\gamma/°$	90
Volume/$Å^3$	1844.84(10)
Z	4
ρ_{calc}mg/mm^3	1.550
m/mm^{-1}	2.201
F(000)	880.0
Crystal size/mm^3	$0.4 \times 0.18 \times 0.05$
Radiation	CuKα (λ = 1.54184)
2Θ range for data collection	6.122 to 155.976°
Index ranges	$-18 \leq h \leq 15$, $-7 \leq k \leq 15$, $-11 \leq l \leq 12$
Reflections collected	7177
Independent reflections	3820 [R_{int} = 0.0233, R_{sigma} = 0.0310]
Data/restraints/parameters	3820/11/282
Goodness-of-fit on F^2	1.038
Final R indexes [I>=2σ (I)]	R_1 = 0.0478, wR_2 = 0.1344
Final R indexes [all data]	R_1 = 0.0547, wR_2 = 0.1418
Largest diff. peak/hole / e Å^{-3}	0.52/-0.33
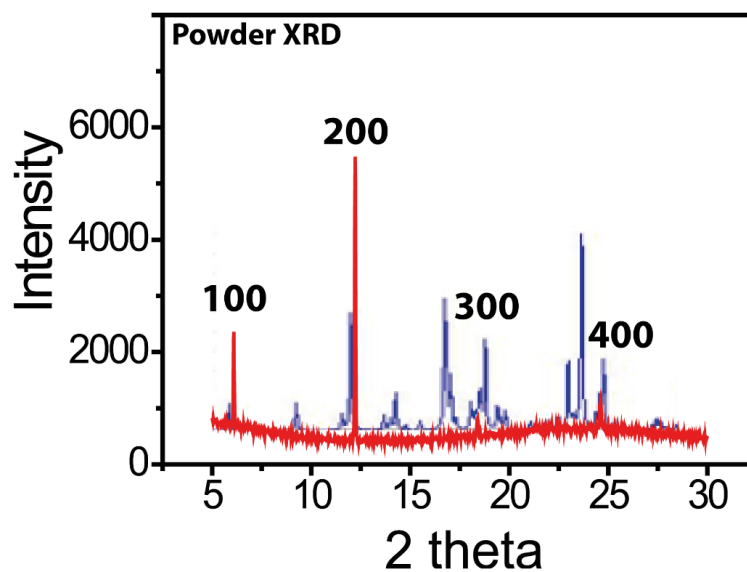
Figure 3.8. Calculated powder X-ray diffraction pattern of bicalutamide form I (blue) and experimental (red) obtained for bicalutamide crystals mounted on a plastic Petri dish (λ = Cu-Kα, 0.1541 nm). The experimentally observed peaks correspond to the (100), (200), (300) and (400) reflections of polymorph I respectively, confirming the orientation of the crystals parallel to the plastic Petri dish.
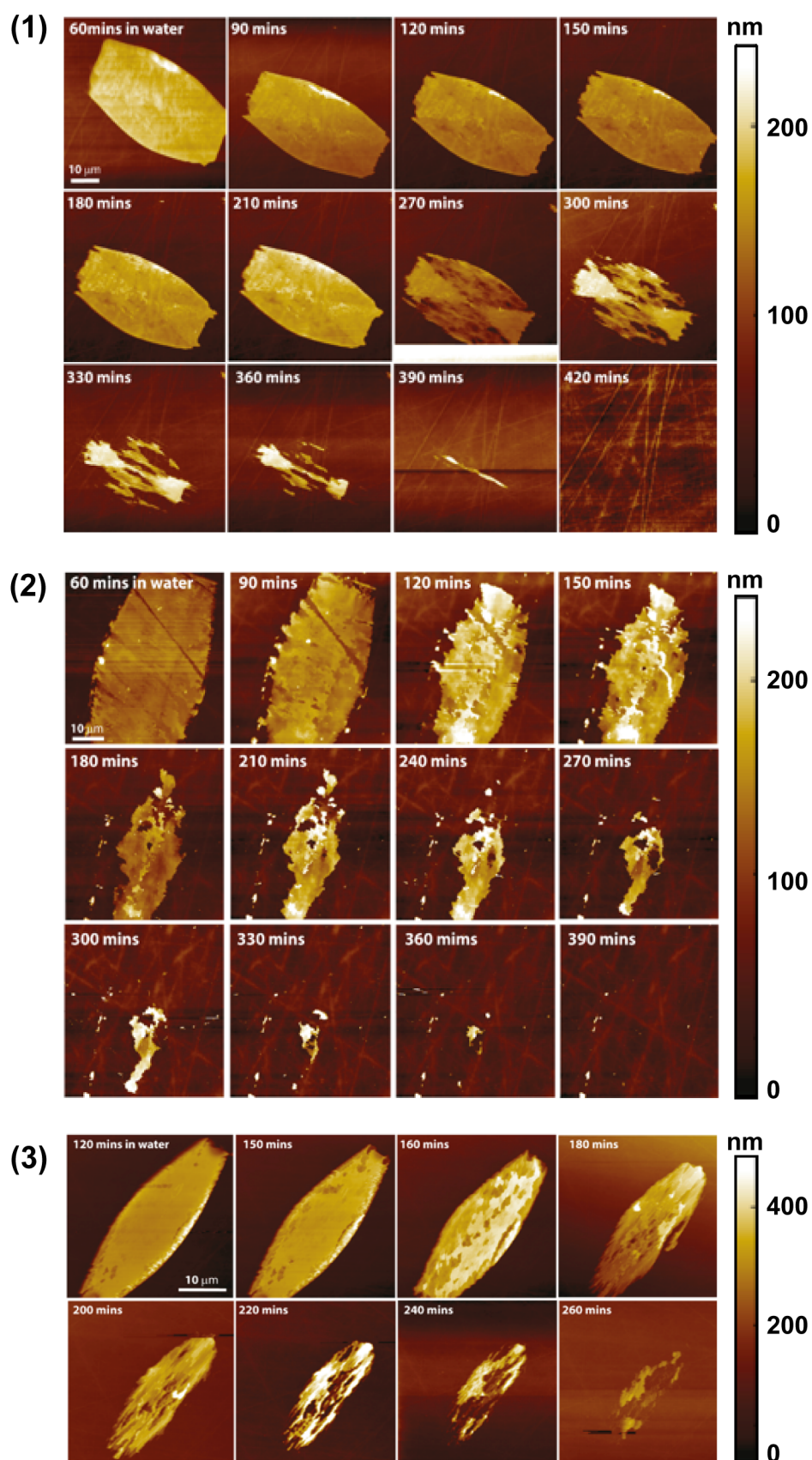
Figure 3.9. AFM topography images of aqueous dissolution sequence of 3 different single BIC crystals.
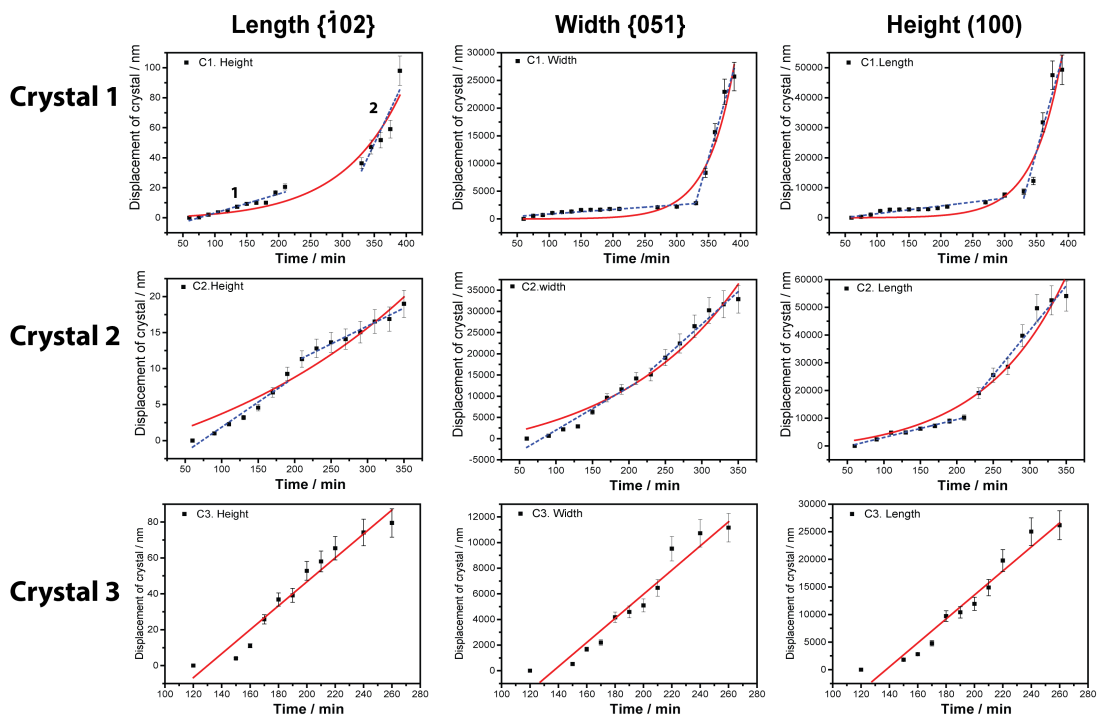
Figure 3.10. Plots showing changes in crystal dimensions over time of the crystals shown in Figure 3.9.
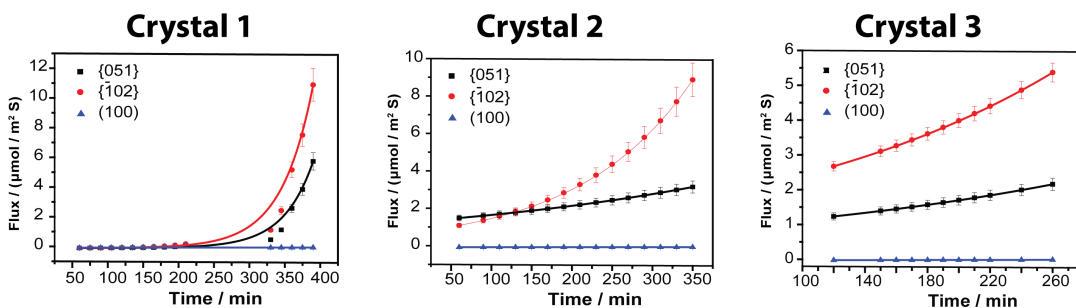
Figure 3.11. Corresponding dissolution rates (flux per unit area) over time of the crystals shown in Figure 3.9. Plots illustrate that as the crystal starts to roughen the dissolution rate increases significantly. The order of the measured dissolution rates for all three crystals was found to be: $(100) < \{051\} < \{\bar{1}02\}$.

Table 3.3. Parameters achieved of the functions used to fit the displacement curves shown in the Figure 3.9.

Crystal 1	R^2 Exponential fit $y = A(1-\exp^{-Bx})$	A	B	R^2 Linear fit $y = A + Bx$	A	B
(100)	0.937	-1.34	-0.011	0.917	-9.48	0.13
				0.906 2nd	-266.23	0.90
{051}	0.945	-2.49	-0.024	0.947 1st	57.49	8.25
				0.991 2nd	-129743.74	402.29
{$\bar{1}$02}	0.933	-8.72	-0.022	0.954 1st	-123.06	25.88
				0.966 2nd	-249519.60	776.19
Crystal 2						
(100)	0.933	-10.48	-0.003	0.973 1st	-5.07	0.07
				0.907 2nd	0.98	0.05
{051}	0.963	-5559.38	-0.006	0.970 1st	-8157.47	101.55
				0.984 2nd	-19269.55	154.12
{$\bar{1}$02}	0.959	-2858.31	-0.009	0.989 1st	-3407.23	64.76
				0.978 2nd	-54758.57	321.41
Crystal 3						
(100)				0.976	-86.81	0.67
{051}				0.970	-12918.79	94.39
{$\bar{1}$02}				0.975	-29912.09	217.30
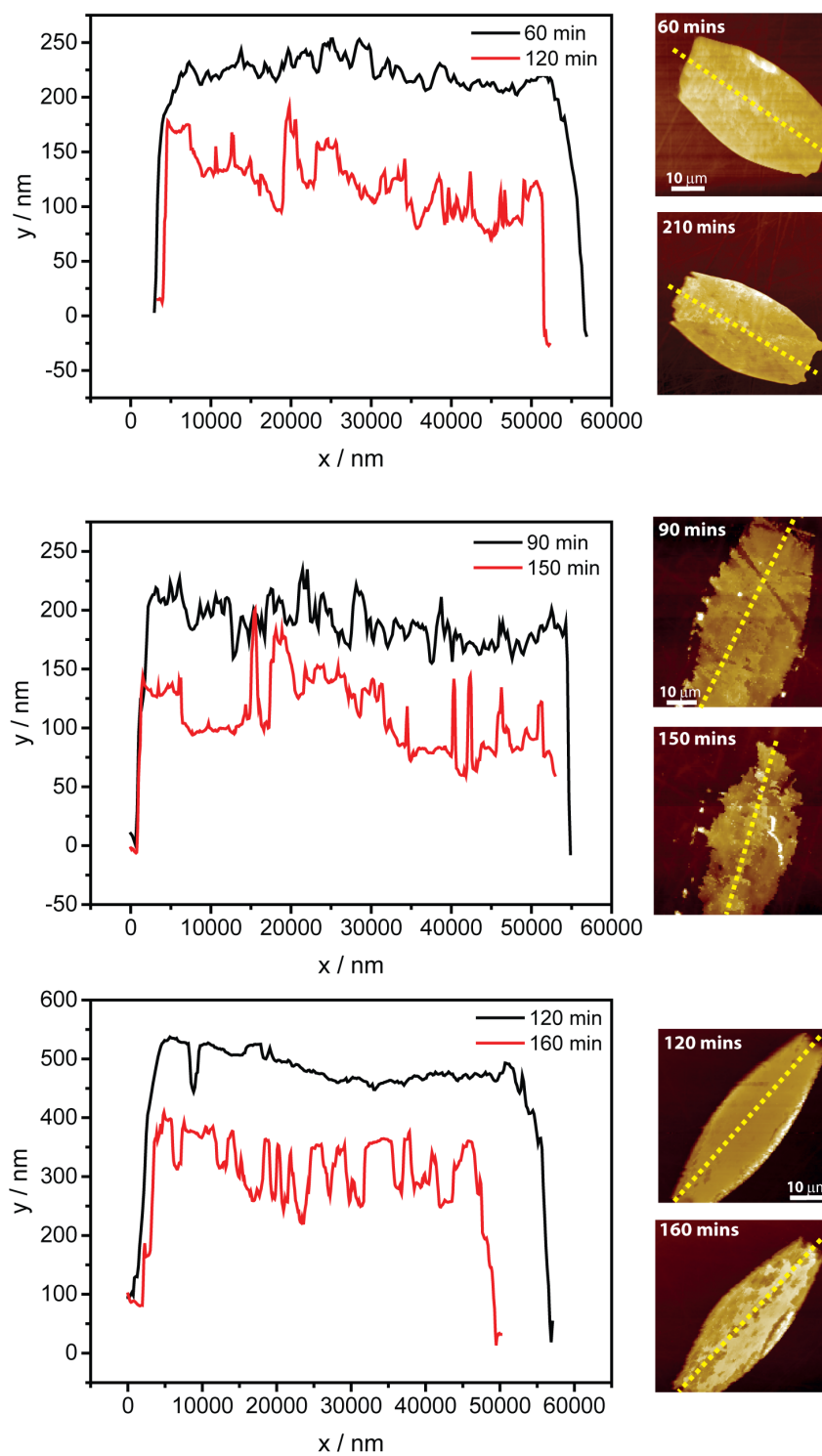
Figure 3.12. Graphs showing cross-sections of the above crystals at various time points.

Table 3.4. Concentration ($\times 10^{-4}$ mM) near the crystal/solution interface and normal total fluxes ($\times 10^{-7}$ mol m^{-2} s^{-1}) at various times for the different crystal faces calculated from FEM simulations

Time (min)	Faces {hkl}	C_{surf} Experimental	C_{surf} MT1	C_{surf} MT2	J_{obs}	J_{MT1}	J_{MT2}
20	100	2.38	116.2	70.2	0.0994	6.63	0.0994
20	051	2.68	116.2	116.2	0.927	20.9	75.2
20	$\bar{1}02$	2.04	116.2	116.2	0.687	32.1	84.7
80	100	3.93	116.2	70.3	0.169	6.98	0.169
80	051	4.45	116.2	116.2	1.80	23.4	88.4
80	$\bar{1}02$	4.01	116.2	116.2	2.19	36.0	99.5
170	100	9.45	116.2	72.1	0.377	7.24	0.377
170	051	11.1	116.2	116.2	4.88	24.2	88.8
170	$\bar{1}02$	14.5	116.2	116.2	12.5	38.5	101.0
230	100	15.5	116.2	74.6	0.643	8.62	0.643
230	051	19.0	116.2	116.2	9.48	27.2	93.5
230	$\bar{1}02$	34.2	116.2	116.2	39.7	45.5	110.1

J_{MT1} = Theoretical flux obtained for when all crystal faces are purely diffusion controlled.

J_{MT2} = Flux obtained when only the {051} and {$\bar{1}02$} faces are purely diffusion controlled and the (100) face dissolves as observed experimentally.

J_{obs} = Experimental flux.

6. References

1. Chen, J.; Sarma, B.; Evans, J. M. B.; Myerson, A. S. *Cryst. Growth Des.* **2011**, *11*, 887-895.

2. Stegemann, S.; Leveiller, F.; Franchi, D.; de Jong, H.; Lindén, H. *Eur. J. Pharm. Sci.* **2007**, *31*, 249-261.

3. Brouwers, J.; Brewster, M. E.; Augustijns, P. *J. Pharm. Sci.* **2009**, *98*, 2549-2572.

4. Blagden, N.; de Matas, M.; Gavan, P. T.; York, P. *Adv. Drug Delivery Rev.* **2007**, *59*, 617-630.

5. Dokoumetzidis, A.; Macheras, P. *Int. J. Pharm.* **2006**, *321*, 1-11.

6. **1997**.

7. Ku, M. S. *The AAPS Journal* **2008**, *10*, 208-212.

8. Unwin, P. R.; Macpherson, J. V. *Chem. Soc. Rev.* **1995**, *24*, 109-119.

9. MacInnis, I. N.; Brantley, S. L. *Chem. Geol.* **1993**, *105*, 31-49.

10. MacInnis, I. N.; Brantley, S. L. *Geochim. Cosmochim. Acta* **1992**, *56*, 1113-1126.

11. Mullin, J. W. *Crystallization*; Butterworth-Heinemann: Oxford; Boston, 2001.

12. Lasaga, A. C.; Luttge, A. *Science* **2001**, *291*, 2400-2404.

13. Blum, A. E.; Yund, R. A.; Lasaga, A. C. *Geochim. Cosmochim. Acta* **1990**, *54*, 283-297.

14. den Brok, S. W. J.; Morel, J. *Geophysical Research Letters* **2001**, *28*, 603-606.

15. Ritchie, G. S. P. In *Advances in Agronomy*, Donald, L. S., Ed.; Academic Press, 1994, pp 47-83.

16. Peruffo, M.; Mbogoro, M. M.; Edwards, M. A.; Unwin, P. R. *Phys. Chem. Chem. Phys.* **2013**, *15*, 1956-1965.

17. Gray, V.; Kelly, G.; Xia, M.; Butler, C.; Thomas, S.; Mayock, S. *Pharm Res* **2009**, *26*, 1289-1302.

18. Coombes, S. R.; Hughes, L. P.; Phillips, A. R.; Wren, S. A. C. *Anal. Chem.* **2014**, *86*, 2474-2480.

19. Nguyen, T. T. H.; Hammond, R. B.; Roberts, K. J.; Marziano, I.; Nichols, G. *CrystEngComm* **2014**, *16*, 4568-4586.

20. Missel, P. J.; Stevens, L. E.; Mauger, J. W. *Pharm. Dev. Technol.* **2005**, *9*, 453-459.

21. Qiu, Y.; Rasmuson, Å. C. *AlChE J.* **1990**, *36*, 665-676.

22. Danesh, A.; Connell, S. D.; Davies, M. C.; Roberts, C. J.; Tendler, S. J.; Williams, P. M.; Wilkins, M. J. *Pharm Res* **2001**, *18*, 299-303.

23. Abendan, R. S.; Swift, J. A. *Cryst. Growth Des.* **2005**, *5*, 2146-2153.

24. Gasharova, B.; Göttlicher, J.; Becker, U. *Chem. Geol.* **2005**, *215*, 499-516.

25. Adobes-Vidal, M.; Maddar, F. M.; Momotenko, D.; Hughes, L. P.; Wren, S. A. C.; Poloni, L. N.; Ward, M. D.; Unwin, P. R. *Cryst. Growth Des.* **2016**, 4421-4429.

26. Macpherson, J. V.; Unwin, P. R. *J. Phys. Chem.* **1994**, *98*, 1704-1713.

27. Perry, A. R.; Lazenby, R. A.; Adobes-Vidal, M.; Peruffo, M.; McKelvey, K.; Snowden, M. E.; Unwin, P. R. *CrystEngComm* **2015**, *17*, 7835-7843.

28. Kinnear, S. L.; McKelvey, K.; Snowden, M. E.; Peruffo, M.; Colburn, A. W.; Unwin, P. R. *Langmuir* **2013**, *29*, 15565-15572.

29. Vega, D. R.; Polla, G.; Martinez, A.; Mendioroz, E.; Reinoso, M. *Int. J. Pharm.* **2007**, *328*, 112-118.

30. Abu-Diak, O. A.; Jones, D. S.; Andrews, G. P. *J. Pharm. Sci.* **2012**, *101*, 200-213.

31. Andrews, G. P.; AbuDiak, O. A.; Jones, D. S. *J. Pharm. Sci.* **2010**, *99*, 1322-1335.

32. Dolomanov, O. V.; Bourhis, L. J.; Gildea, R. J.; Howard, J. A. K.; Puschmann, H. *J. Appl. Crystallogr.* **2009**, *42*, 339-341.

33. Sheldrick, G. *Acta Crystallogr., Sect. A: Found. Adv.* **2008**, *64*, 112-122.

34. Sheldrick, G. *Acta Crystallographica Section C* **2015**, *71*, 3-8.

35. Wilke, C. R.; Chang, P. *AIChE J.* **1955**, *1*, 264-270.

36. Prasad, K. V. R.; Ristic, R. I.; Sheen, D. B.; Sherwood, J. N. *Int. J. Pharm.* **2002**, *238*, 29-41.

37. Kaemmer, S.; Bruker Nano Surfaces Division, Santa Barbara, 2011.

38. Gasperino, D.; Yeckel, A.; Olmsted, B. K.; Ward, M. D.; Derby, J. J. *Langmuir* **2006**, *22*, 6578-6586.

39. Peruffo, M.; Mbogoro, M. M.; Adobes-Vidal, M.; Unwin, P. R. *J. Phys. Chem. C* **2016**, *120*, 12100-12112.

40. Adobes-Vidal, M.; Shtukenberg, A. G.; Ward, M. D.; Unwin, P. R. *Cryst. Growth Des.* **2017**.

41. Burt, D. P.; Wilson, N. R.; Janus, U.; Macpherson, J. V.; Unwin, P. R. *Langmuir* **2008**, *24*, 12867-12876.

42. Christoffersen, J.; Christoffersen, M. R. *J. Cryst. Growth* **1988**, *87*, 41-50.

43. Jiang, H. B.; Cuan, Q.; Wen, C. Z.; Xing, J.; Wu, D.; Gong, X.-Q.; Li, C.; Yang, H. G. *Angew. Chem., Int. Ed.* **2011**, *50*, 3764-3768.

44. Burt, H. M.; Mitchell, A. G. *Int. J. Pharm.* **1981**, *9*, 137-152.

45. Macrae, C. F.; Edgington, P. R.; McCabe, P.; Pidcock, E.; Shields, G. P.; Taylor, R.; Towler, M.; Streek, J. v. d. *J. Appl. Crystallogr.* **2006**, *39*, 453-457.

46. Ward, M. D. *Chem. Rev.* **2001**, *101*, 1697-1726.

47. Ren, F.; Jing, Q.; Tang, Y.; Shen, Y.; Chen, J.; Gao, F.; Cui, J. *Drug Dev. Ind. Pharm.* **2006**, *32*, 967-972.

Chapter IV | Multiscale Visualization and Quantitative Analysis of L-Cystine Crystal Dissolution

Abstract

There is considerable interest in the growth and dissolution of the hexagonal form of L-cystine crystals, not least because L-cystine kidney stones - aggregates of single crystals of L-cystine - are a consequence of the genetic disorder cystinuria. While recent investigations have revealed the growth mechanism and kinetics of L-cystine crystals at the molecular level, the dissolution process has not yet been considered. Dissolution involves coupled surface and diffusion processes at different crystal faces exposed to solution, presenting a significant challenge for quantitative physicochemical measurements. The multi-microscopy approach herein uses a range of complementary *in situ* microscopy techniques – atomic force microscopy (AFM), scanning ion conductance microscopy (SICM) and optical microscopy – combined with finite element method (FEM) analysis, to reveal the mechanism of face-specific dissolution and the associated kinetics. Dissolution from the {0001} face involves the formation of funnel-shaped hexagonal pits, centered at single screw dislocation cores, but the handedness of the dissolution spirals is opposite to that found for steps in growth spirals. Significantly, step velocities measured by AFM quantitatively scale up to capture the overall dissolution kinetics of this face, and the measurements further serve as a roadmap for the quantitative analysis of single crystal dissolution and growth.

1. Introduction

Kidney stones comprising L-cystine account for nearly 2% of all stones, affecting more than 20,000 U.S. patients annually. Unlike calcium oxalate monohydrate (COM) stones, cystine stones are caused by a genetic disorder and tend to be larger, recur more frequently, and are more likely to cause chronic kidney disease.[1] The formation of L-cystine stones is a consequence of excessive levels of L-cystine in the urine due to excess excretion of cystine.[2] Exacerbated further by the low solubility of L-cystine,[3] which provokes the formation of crystals that aggregate into millimeter-sized stones. This has prompted recent investigations of the growth and inhibition of L-cystine crystallization at the microscopic level,[4-8] and the discovery of molecular inhibitors that arrest L-cystine growth. These inhibitors show promise as therapeutic agents,[9,10] possibly serving as replacements for existing treatments[11,12] that often are not effective in the prevention of L-cystine stones.[5,7] It is reasonable to suggest that agents that promote dissolution of existing L-cystine crystals may represent an alternative strategy for interrupting stone formation, especially in light of recent work on COM,[13] but to our knowledge the microscopic mechanisms of L-cystine crystal dissolution have not been explored.
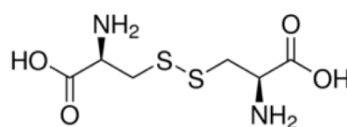
Scheme 4.1. Molecular Structure of L-Cystine

L-cystine crystallizes in the $P6_122$ space group, forming hexagonal crystals with large $\{0001\}$ faces confined by six equivalent $\{10\bar{1}0\}$ faces.[14] The micromorphology of $\{0001\}$ faces during crystal growth from aqueous solution revealed the formation of hexagonal hillocks emerging from screw dislocations with a Burger vector normal to $\{0001\}$ at concentrations below 3.5 mM[7] (the equilibrium solubility, C_{sat}, is 0.7 mM at 25°C).[15,16] The growth mechanism, kinetic coefficient of the $\{10\bar{1}0\}$ steps, critical length and step spacing of grown spirals at dislocations, at different supersaturations, were determined using real-time *in situ* atomic force microscopy (AFM),[6,7] which has become an exceptionally powerful technique to study crystal growth and dissolution

at the nanoscale.[17-24] This method, however, typically is used for examining a particular crystal face and is limited to processes that are slow compared to the image acquisition rate.[25,26]

Herein, we describe an investigation of the dissolution of hexagonal L-cystine crystals, with the aim of obtaining quantitative information about the relationship between surface structure and reactivity, the role of mass transport in dissolution, the influence of interfacial solute concentration on the dissolution kinetics and mechanism,[25] and changes in dissolution kinetics accompanying changes in crystal morphology. Furthermore, our studies reveal critical information on the relationship between crystal growth and dissolution under equivalent *interfacial driving force*, an important consideration of general interest in the crystal growth/dissolution field that has proved difficult to address.

Using a recently introduced approach[27] (introduced in chapter II) that combines optical microscopy (OM) and scanning ion-conductance microscopy[28] (SICM), quantitative 3D visualization of crystal morphology during the dissolution of micro-crystals can be realized under conditions of well-defined and high mass transport rates, enabling determination of face-dependent dissolution rates. The experimental data permit the determination of interfacial concentrations, concentration gradients, and separation of kinetic and mass transport limiting regimes with finite element method (FEM) simulations.[27,29,30] Specifically, the dissolution rates of the $\{0001\}$ and $\{10\bar{1}0\}$ faces of L-cystine crystals have been determined. Imaging of the $\{0001\}$ face of L-cystine crystals during dissolution by real-time *in situ* AFM at various cystine concentrations provides substantial insights into the dissolution mechanism through measurement of step velocities on hexagonal spirals descending along screw dislocations on the $\{0001\}$ face. Kinetic data obtained from OM-SICM and AFM, which measure kinetics in different ways, are in good agreement when the different mass transport regimes of the two experimental configurations are accounted for. These measurements thus provide a rare example of dissolution kinetics that are quantitatively self-consistent from the nanoscale to the macroscopic (whole crystal) level and underpinned by a detailed mechanistic view of the dissolution process.

2. Experimental

2.1 Crystallization of L-Cystine

Hexagonal L-cystine crystals were crystallized from an aqueous solution (18.2 MΩ cm, Direct-Q 3 Millipore) containing 2 mM L-cystine (Sigma-Aldrich, St. Louis, MO), prepared by heating under reflux at 100 °C for 30 min with stirring. The solution was cooled slowly to room temperature with mild stirring for 70 min and transferred to a glass container that was sealed to prevent evaporation. The resulting solution (pH = 6.5) corresponded to a relative supersaturation $C/C_{sat} \approx 3$, based on the L-cystine solubility (C_{sat} = 0.7 mM at pH = 7; 25 °C).[15,16] Crystals for AFM measurements were obtained by storing this solution at room temperature without stirring for 10 days, after which large (> 100 μm across) hexagonal single crystals were collected by vacuum filtration (Whatman grade 1 filters, >11 μm pores) and air-dried. Crystals for OM-SICM studies were harvested by transferring 4 mL aliquots to separate 47 mm diameter circular glass microscope slides (Thermo Scientific, Inc. Waltham, MA), each mounted into a 47 mm diameter Petri dish (Willco Wells, Netherlands) with a Plexiglas rim. The Petri dish was covered and allowed to stand at room temperature until single crystals with {0001} faces having ca. 20 μm cross section were observed attached to the glass slide. The supernatant solution was then removed, the crystals rinsed with water, and dried with a nitrogen stream.

2.2 Optical Microscopy-Scanning Ion-Conductance Microscopy (OM-SICM) Measurements

Dissolution studies were performed at 25 °C and pH 6.5 in 100 mM KCl electrolyte solution (Sigma-Aldrich, AR grade). Note that the solubility of L-cystine is relatively insensitive to ionic strength from pure water (as used for AFM, see below) to this concentration of electrolyte,[15] so that the driving force for AFM and OM-SICM experiments was the same. The combined OM-SICM system comprised a homebuilt SICM mounted on an inverted optical microscope (Axiovert 40 CFL, Zeiss, Germany) as previously described.[27,31] The optical microscope was equipped with an LED light source (BXRA-56C1600-B-00, Bridgelux Inc. Livermore, CA) to reduce sample heating and a video camera (B700, PixeLINK). SICM probes were fabricated from quartz capillaries (1.2 mm o.d., 0.69 mm i.d., Harvard Apparatus, Holliston,

MA) using a laser puller (P-2000, Sutter Instruments, Novato, CA) and optimized pulling parameters to produce tips with an opening diameter *ca.* 80 nm. The nanopipettes were filled with the same electrolyte solution (100 mM KCl) used for the bathing solution and mounted on a single axis (*Z*) piezoelectric positioner (P-753-3CD, PhysikInstrumente, Germany) with a 38 μm travel range to control the height of the probe, here oriented normal to the {0001} face of an L-cystine crystal. The petri dish containing the crystals was mounted on a two-axis (*XY*) piezoelectric positioner system (Nano-BioS300, Mad City Labs Inc., Madison, WI) for lateral positioning. The SICM was operated in bias modulated (BM) mode,[32] in which there was an oscillating (sinusoidal) bias between a Ag/AgCl quasi-reference counter electrode in the tip and one in the bath (38 mV amplitude, 358 Hz frequency), generated by a lock-in amplifier (SR830, Stanford Research Systems, Sunnyvale, CA) with zero net (time-averaged) bias. The resulting current response was measured using a custom-built wideband current-to-voltage converter. The SICM setup was controlled with a programmed FPGA card (7852R, National Instruments, Austin, TX) using LabVIEW (2013, National Instruments, Austin TX).

L-cystine single crystals, with ca. 20 μm wide {0001} faces and diffusionally isolated (separated by at least 800 μm) from neighboring crystals were selected for study. Following addition of 4 mL of the electrolyte solution to the Petri dish, time-lapse sequences of optical images (40X objective, every 30 s) and line traces along the crystal in a BM-SICM hopping mode[32-34] were acquired. The nanopipette probe was lowered toward the surface at a rate of 1 μm/s at each position. When the near-surface was detected by the probe as a change of 0.5° in the phase of the AC current, the *Z* position was recorded and the nanopipette was retracted *ca.* 10 μm at a speed of 10 μm/s. It was then moved laterally to a new position, typically 3-6 μm from the previous point. This process was repeated at a minimum of 10 lateral positions, which led to the acquisition of a height profile every 2 min. The dissolution velocity of the {0001} face was determined by measuring the height displacements as a function of time. The acquisition time of the SICM data was slower than previously reported for other dissolution studies[27] due to the height of L-cystine crystals (~ 8 μm) at the beginning of the experiment, but the time resolution was sufficient for the dissolution kinetics measured. The dissolution velocities of the {10$\bar{1}$0} faces were determined

from time-lapse optical microscope images, by measuring the edge to center distance using ImageJ (version 1.45, NIH).

2.3 Real-Time *in Situ* Atomic Force Microscopy

AFM crystal growth and dissolution experiments were performed as described previously.[5-8] L-cystine crystals, *ca.* 100 μm across, were sprinkled onto an AFM sample mounting disk coated with Norland optical adhesive (type 81) partially cured by UV exposure (λ = 365 nm, 1 min), and then pressed gently against the disk using weighing paper. The {0001} faces of the plate-like hexagonal crystals naturally aligned parallel to the disk surface. The crystals were then fixed permanently by curing the adhesive completely (15 min). Dissolution and growth studies were performed in a fluid cell at room temperature with a Nanoscope IIIa Multimode system (Digital Instruments, Santa Barbara, CA) in contact mode using Veeco NP-BSi$_3$N$_4$ tips on silicon nitride cantilevers with a spring constant of 0.12 N/m. Prior to measurements, the crystals were etched slightly by flushing the fluid cell with 0.5 mL of deionized water at a rate of 15 mL/h to remove any impurities or amorphous deposits on the surface. This flow rate corresponds to a Reynolds number of Re = 11.5, consistent with laminar flow ($Re = rUL/m$, where r = 0.997 g/cm^3 and m = 0.00954 g/cm·s are the fluid density and viscosity, respectively, U = 1.1 cm/s is the centerline velocity at the fluid cell inlet, and L = 0.1 cm is the thickness of the fluid cell). The velocity of the major steps, v_{step}, on the {0001} face was measured at various L-cystine concentrations (2 mM for growth and 0-0.6 mM for dissolution) under a continuous flow of solution, at a rate of V_f = 15 mL/h, by measuring the distance of the steps from the dislocation core in consecutive deflection images. Images with the same scan direction, acquired at periodic intervals of 10 s, were analyzed using ImageJ (version 1.45, NIH).

2.4 Numerical Simulations

All simulations were performed using the commercial finite element method (FEM) modeling package Comsol Multiphysics 4.4 (Comsol AB, Sweden) installed on a Dell Intel Core 7i Quad 3.40 GHz computer equipped with 32 GB of RAM running Windows 7 Professional 64 bit edition. Three-dimensional models were formulated to simulate and evaluate the fluid flow and mass transport of L-cystine dissolution

during the OM-SICM and AFM experiments. The models were defined using geometrical parameters and morphological changes in the crystal over time obtained from experimental data. Calculations employed optimized triangular and tetrahedral mesh elements. More details about the 3D domains used are provided in Supporting Information, Figures 4.12 and 4.13.

For the OM-SICM models, the mass transport of L-cystine away from the crystal during dissolution was described by the steady-state diffusion equation (eq. 4.1) where J is the flux, c is the concentration of the L-cystine solute, and D is the L-cystine diffusion coefficient.

$$\nabla J = -D\nabla^2 c = 0 \qquad (4.1)$$

The characteristic diffusional time t_{diff} for mass transport from microscopic surfaces to bulk solution can be estimated using equation 4.2, where d is the size of the crystal.

$$t_{diff} \approx d^2 / D \qquad (4.2)$$

The diffusion coefficient of L-cystine (7.5×10^{-6} cm^2/s), was estimated from the Wilke-Chang correlation[35] (eq. 2.2.) and was assumed constant over the entire domain. The absolute error in the diffusivities (pure water) determined with this correlation have been reported to be no more than 11%,[36] which would have a minor impact on the results presented here. The characteristic time for a diffusion front to travel a distance equal to the crystal size of $d \sim 20$ mm size (a reasonable estimate for the time to steady-state) is approximately 0.2 s, which is four orders of magnitude faster than the duration of a typical OM-SICM dissolution experiment (30 minutes for the complete dissolution of a crystal), justifying the use of a steady-state model.

The models denoted here as EXP1, EXP2 and EXP3 simulate the mass transport of L-cystine during the dissolution of a particular crystal at different times in an OM-SICM experiment. Three models were used due to the change in the crystal morphology over time. The parameters used to define the models, specifically the crystal dimensions, geometry and flux of material (per unit area) for each crystal face (observed dissolution rate, $J^{obs}_{\{hkil\}}$) at a given time were determined experimentally (*vide infra*). Using appropriate boundary conditions (Table 4.4, Supporting Information) the

concentration of L-cystine near the crystal-solution interface and in the solution around the dissolving crystal was simulated, from which it was possible to distinguish the dissolution regime, i.e. the balance between mass transport and surface kinetics control (*vide infra*). In order to deduce the relative importance of mass transport and surface kinetics, models (MTM1, MTM2 and MTM3) with the same geometry as the corresponding EXP models were employed, but with the dissolution regime completely controlled by diffusion (L-cystine concentration at the crystal-solution interface $C_{int} = C_{sat}$) (Table 4.4, Supporting Information). Solution of the partial differential equations for both types of models (EXP and MTM) was achieved using the direct solver MUMPS in the Comsol environment, with a relative error tolerance of 10^{-6}. Simulations were carried out with >24,000,000 tetrahedral mesh elements. The mesh resolution was refined to be the finest, down to a value of 0.1 nm, at the surfaces of the crystal.

The steady-state approach to mass transport is also applicable for the *in situ* AFM model, in which L-cystine crystal dissolution occurs in a continuous solution flow. Mass transport around the dissolving crystal is described by equation 4.3,

$$D\nabla^2 c - \mathbf{v} \cdot \nabla c = 0 \qquad (4.3)$$

where **v** is the velocity vector calculated from the momentum conservation (eq. 4.4) and continuity (eq. 4.5) Navier-Stokes equations for an incompressible fluid,

$$\rho \mathbf{v} \cdot \nabla \mathbf{v} = \eta \nabla^2 \mathbf{v} - \nabla p \qquad (4.4)$$

$$\rho \nabla \mathbf{v} = 0 \qquad (4.5)$$

where ρ and η are the solution density (1.00 g/cm^3) and dynamic viscosity (1.00 mPa·s), respectively, and p is the pressure. Boundary conditions applied for the calculation of fluid flow and convective-diffusion mass-transport in the AFM cell are supplied in Table 4.5, Supporting Information. The AFM model examined the crystal−solution interfacial concentration of an L-cystine crystal *ca.* 100 mm across and 10 mm height, dissolving in a fluid cell flushed with solution at a rate of $V_f = 15$ mL/h. For comparison with experimental AFM data, dissolution rates of each crystal face were defined by an intrinsic dissolution rate constant (kinetic coefficient)

determined from OM-SICM dissolution experiments and the corresponding mass transport-kinetic simulations.

3. Results and Discussion

3.1 Dissolution Rates and Intrinsic Rate Constants: OM-SICM and FEM Modeling

When studying dissolution kinetics, it is essential to consider the series of events that constitute the dissolution process. These events comprise (*i*) those occurring at the crystal surface, such as detachment of molecules from active sites, surface diffusion and desorption and (*ii*) the mass transport of detached solvated species away from the crystal to the undersaturated bulk solution. The slowest process will limit the overall dissolution rate and the dissolution kinetics can be described as surface–kinetic controlled (mass transport comparatively fast), mass–transport controlled (mass transport comparatively slow), or in a mixed regime (comparable surface and mass transport contributions). Only a few techniques can reliably differentiate between mass transport and surface kinetic contributions,[37,38] and the deduction of the growth regime often can be difficult.[25] Microscale single crystals can be advantageous for separating mass transport from surface kinetic effects in dissolution studies, as they provide for mass transport rates that are high and well-defined (*i.e.*, can be modeled), to the extent that surface kinetics can be obtained.[27,30] L-cystine single crystals with well-defined facets no larger than 20 μm across were used here to ensure rapid diffusion of L-cystine from dissolving crystal surfaces to the surrounding solution.

OM-SICM enables tracking of time-dependent changes in the crystal 3D morphology. The retreat of the $\{10\bar{1}0\}$ faces (edge-to-center distance) was recorded by time-lapse images acquired with optical microscopy (Figure 4.1). The changes in crystal height (thickness) were determined from the retreat of the $\{0001\}$ face, as measured by BM-SICM.[32] This scanning mode was chosen because it minimizes the perturbations of the local ionic atmosphere, so that convective and electro-osmotic effects can be neglected.[39]
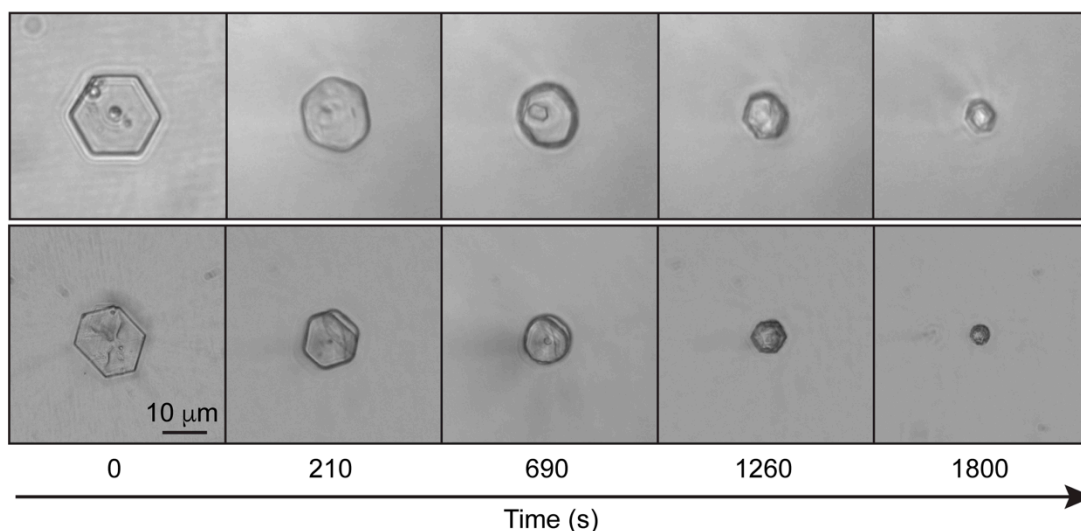
Figure 4.1. Time-lapse optical micrographs of the dissolution of two L-cystine single crystals in an aqueous solution containing only 100 mM KCl, as viewed normal to the {0001} face.

Linear dissolution rates, $v_{\{hkil\}}$, measured separately for three different crystals in 100 mM KCl aqueous solutions behave similarly. The dissolution rate of each crystal face increased monotonically, although the dissolution behavior could be parsed into three stages distinguished by different dissolution rates and morphology (Figure 4.2). Crystals in stage 1 are polygonal with sharp edges and corners. The edges and corners become more rounded in stage 2, and crystals in stage 3 tend toward a disc-like morphology, although precise characterization of the shape of these small crystals is difficult due to the resolution limits of optical microscopy. This is consistent with the formation of higher index microfacets, which would be expected to result in higher dissolution kinetic coefficients.[40-43] A decrease in crystal size, however, also results in higher mass transport rates.[27] Measurement of the crystal height in stage 1 was not feasible due to the time required for tip engagement near the (0001) face. The {0001} face is the largest crystal face exhibited by as-grown crystals, consistent with a lower surface energy and slower growth rate perpendicular to the face[44,45] than the $\{10\bar{1}0\}$ faces on the perimeter. Accordingly, the difference between the $\{10\bar{1}0\}$ dissolution rates in stages 1 and 2 is much less pronounced than between stages 2 and 3. Therefore, it is reasonable to suggest that during stage 1 the dissolution rate of the {0001} face, which dissolves more slowly than $\{10\bar{1}0\}$, would not differ substantially from that of stage 2. Hence, we assume that the {0001} dissolution rates in stages 1 and 2 are the same.

109
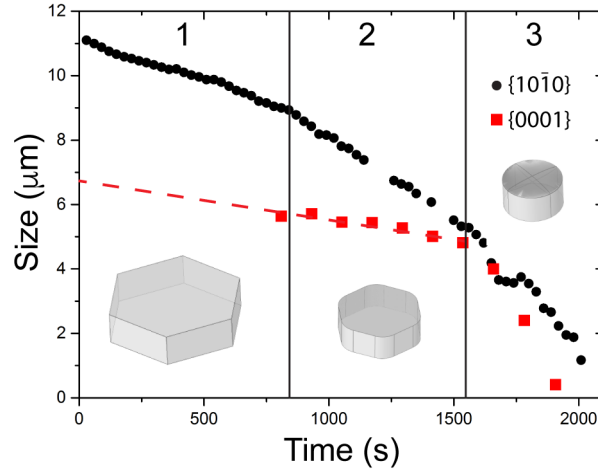
Figure 4.2. Size evolution of a representative L-cystine crystal during dissolution in 100 mM KCl. Retreat of the {10$\bar{1}$0} faces, as measured edge-to-center, is denoted by black dots. Retreat of the {0001} face, as measured from crystal height change, is denoted by red squares. The dashed red line denotes extrapolation of the crystal height to t = 0 s. Three different stages of the dissolution process, each with a unique dissolution rate, are denoted by regions 1, 2 and 3. The crystal morphology in each region stage is depicted schematically.

The molar dissolution rates for each {$hkil$} face, tantamount to the L-cystine flux from the surface, $J^{obs}_{\{hkil\}}$, were calculated from their linear dissolution rates ($v_{\{hkil\}}$) using equation 4.6, where V_m is the molar volume of hexagonal L-cystine (1.42 $\times 10^{-4}$ m^3 mol^{-1}).[7] The average value of $J^{obs}_{\{hkil\}}$ for the {10$\bar{1}$0} and {0001} faces at each stage, determined from data acquired for three crystals, were combined with the crystal shapes to formulate FEM models corresponding to each of the three stages (Table 4.1; EXP1, EXP2 and EXP3). This enabled calculation of the L-cystine concentration at the crystal-solution interface, C_{int}, as well as the concentration gradients at the interface (Figures 4.3B1-B3 and Table 4.2). The FEM calculations revealed that C_{int} $_{\{10\bar{1}0\}}$ > C_{int} $_{\{0001\}}$, both values increasing with time, i.e., C_{int} **(EXP1)** < C_{int} **(EXP2)** < C_{int} **(EXP3)** (Figures 4.3B1-B3). During stage 1, dissolution at both faces is slow, C_{int} is not appreciably different from the bulk concentration, and the concentration gradient is shallow (Figure 4.3B1). This is consistent with dissolution essentially limited by surface kinetics.[46] As crystal dissolution continues, C_{int} at both the {10$\bar{1}$0} and {0001} crystal faces increases (Figures 4.3B2-B3), indicating that the kinetic coefficient for dissolution increases. The increase in C_{int} causes the concentration gradient to become steeper, leading to increase in mass flux of L-cystine from the

surface. Notably, C_{int} never reaches C_{sat}, such that the system is always in a mixed regime with comparable mass transport and surface kinetic contributions. A simple schematic illustrating the effects of kinetic control on diffusion profiles at each dissolution stage is presented in Figure 4.14 of the Supporting Information.

$$J^{obs}_{\{hkil\}} = v_{\{hkil\}} / V_m \tag{4.6}$$

Table 4.1. Comparison of experimental average dissolution fluxes ($J^{obs}_{\{hkil\}}$) and dissolution fluxes calculated for a pure mass-transport limited condition ($J^{MTM}_{\{hkil\}}$) for the {10$\bar{1}$0} and {0001} faces of L-cystine crystals at the three stages in Figure 4.2. Flux units are 10^{-5} mol·m^{-2}·s^{-1}. The standard deviation for $J^{obs}_{\{hkil\}}$ during stage 3 is larger than for the other two stages due to the rapid change in crystal size, which reduces the measurement precision.

Faces	Stage 1		Stage 2		Stage 3	
	$J^{obs}_{\{hkil\}}$	$J^{MTM}_{\{hkil\}}$	$J^{obs}_{\{hkil\}}$	$J^{MTM}_{\{hkil\}}$	$J^{obs}_{\{hkil\}}$	$J^{MTM}_{\{hkil\}}$
{10$\bar{1}$0}	2.0 ± 0.1	4.5 ± 0.3	3.5 ± 0.1	5.6 ± 0.5	4.7 ± 0.5	9.1 ± 0.3
{0001}	1.0 ± 0.2	3.6 ± 0.3	1.0 ± 0.2	4.7 ± 0.5	6.5 ± 1.9	9.2 ± 0.4

Table 4.2. Average interfacial concentration at the {10$\bar{1}$0} and {0001} faces of L-cystine crystals calculated from FEM simulations (EXP models).

Faces	C_{int}, mM		
	Stage 1	Stage 2	Stage 3
{10$\bar{1}$0}	0.28 ± 0.04	0.37 ± 0.03	0.39 ± 0.05
{0001}	0.25 ± 0.05	0.28 ± 0.04	0.44 ± 0.08

The contributions of mass transport and surface kinetics to dissolution were evaluated further by comparison of experimental dissolution rates with models that invoked pure mass transport-limiting behavior, for which $C_{int} = C_{sat}$, during each of the three stages (models MTM1, MTM2 and MTM3, Figures 4.3C1-C3). The mass transport-limited flux at each crystal face, defined as $J^{MTM}_{\{hkil\}}$, increases with time due to an increasing contribution from hemispherical diffusion as a consequence of the rounding of the crystal and its reduction in size (Table 4.1). Notably, $J^{MTM}_{\{hkil\}}$ is always

larger than the experimental flux $J_{\{hkil\}}^{obs}$, consistent with persistent kinetic limitations and a mixed kinetic regime.
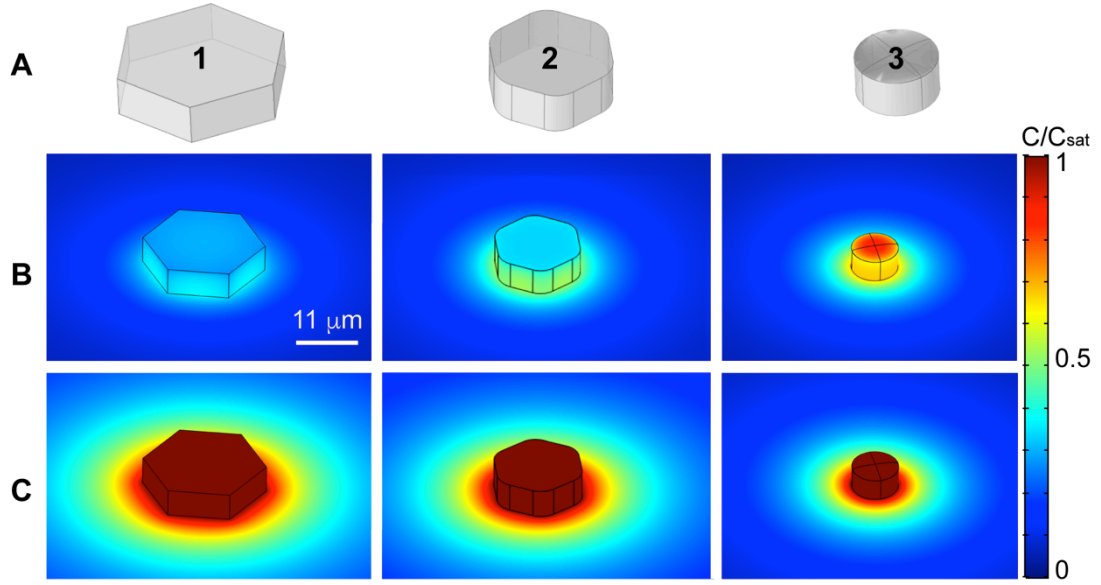
Figure 4.3. (A) Crystal geometries used in FEM models for the three dissolution stages in Figure 4.2. (B) Results of FEM simulations EXP1, EXP2 and EXP3 for the interfacial concentration and concentration profiles of a particular L-cystine crystal during dissolution. (C) Interfacial concentrations and concentration profiles in a mass transport–controlled process obtained from simulations MTM1, MTM2 and MTM3 for the same crystal. C/C_{sat} denotes the saturation ratio around the crystal.

The surface kinetics generally obeys a power law described by the empirical relationship in equation 4.7, where $J_{\{hkil\}}^{SK}$ represents a detachment rate from an {*hkil*} face, $k_{\{hkil\}}^{int}$ is the corresponding intrinsic dissolution rate constant, and *n* is the order of the surface reaction.[47] Conversely, the diffusive mass transport rate depends linearly on the concentration gradient, as described by Equation 4.8, where δ is the thickness of the diffusion boundary layer.[47] At steady-state, $J_{\{hkil\}}^{SK}$ (which corresponds to the experimental $J_{\{hkil\}}^{obs}$) is equal to $J_{\{hkil\}}^{MT}$ (equation 4.9), allowing determination of $k_{\{hkil\}}^{int}$ for each crystal face during each dissolution stage from the $J_{\{hkil\}}^{obs}$ and C_{int} values, the latter determined from the EXP models. The order of the surface reaction with respect to interfacial driving force depends on the mechanism of the reaction.[47-51] For the analysis here, we use $n \approx 1$, which is most appropriate for high interfacial driving force[49] and is a value which is corroborated by AFM measurements under similar

conditions (*vide infra*). This allows $k_{\{hkil\}}^{int}$ for each crystal face to be calculated (Table 4.3).

$$J_{\{hkil\}}^{SK} = k_{\{hkil\}}^{int}(C_{sat} - C_{int})^n \tag{4.7}$$

$$J_{\{hkil\}}^{MT} = \frac{D}{\delta}(C_{int} - C_{bulk}) \tag{4.8}$$

$$J_{\{hkil\}}^{obs} = J_{\{hkil\}}^{SK} = J_{\{hkil\}}^{MT} = k_{\{hkil\}}^{int}(C_{sat} - C_{int}) \tag{4.9}$$

Table 4.3. Intrinsic rate constants calculated for the {10$\bar{1}$0} and {0001} faces (10^{-5} m·s^{-1}).

Faces	$k_{\{hkil\}}^{int}$		
	Stage 1	Stage 2	Stage 3
{10$\bar{1}$0}	4.7 ± 0.7	10.7 ± 1.0	15.2 ± 4.2
{0001}	$2.3 \pm 0.6*$	2.4 ± 0.6	25.2 ± 16.2

* $J_{\{0001\}}^{obs}$ in stage 1 was assumed to be constant and similar to that in stage 2 (*vide supra*).

The entries in Table 4.3 reveal that $k_{\{hkil\}}^{int}$ increases as the L-cystine crystal dissolves, mirroring the increase in the experimental $J_{\{hkil\}}^{obs}$. During stage 1, when the crystal is polygonal with well-defined facets, the crystal faces are expected to have low step edge and kink density[52] compared with stages 2 and 3, when the crystal surface is more rounded (Figure 4.1), tantamount to higher step density and the formation of steps with higher Miller indices. It is reasonable to expect that the formation of these steps would be accompanied by an acceleration in the dissolution rate, as clearly observed in stage 3.[41] This is not unlike the behavior observed for other molecular crystals.[27,30,53] The crystal morphology of L-cystine is consistent with a lower surface energy for the {0001} face compared with {10$\bar{1}$0}. Therefore, it is expected that $k_{\{0001\}}^{int} < k_{\{10\bar{1}0\}}^{int}$ is consistent with the $J_{\{hkil\}}^{obs}$ values. Collectively, these results reveal that the intrinsic rate constant for L-cystine detachment from the crystal surfaces increases as the crystal dissolves owing to the change of morphology.

3.2 In situ AFM of {0001} Dissolution

As reported previously for L-cystine growth,[5-7] the hexagonal spirals can be attributed to the coincidence of a screw dislocation, with a Burger's vector equal to the lattice parameter c = 5.6275 nm, with the crystallographic 6_1 screw axis. For growth, each spiral consists of a single molecular layer of L-cystine (~ 1 nm height) with six crystallographically identical $\langle 10\bar{1}0 \rangle$ directions (white lines at the dislocation core in Figure 4.4A and 4.4D) that advance across the terrace from the dislocation.[6] The spirals rotate clockwise and synchronously about the c axis, spinning out to form six interlacing spirals, which then bunch due to in-plane growth rate anisotropy along the six different directions of each spiral. This results in a micromorphology that resembles islands of with ca. 5.6 nm height (major steps), as illustrated in Figure 4.4A-D. The handedness of the spiral growth hillocks on the {0001} faces of L- and D-cystine reflects the chirality at the molecular level; the spirals spin counterclockwise on L-cystine {0001} but clockwise on D-cystine {0001}.[7]
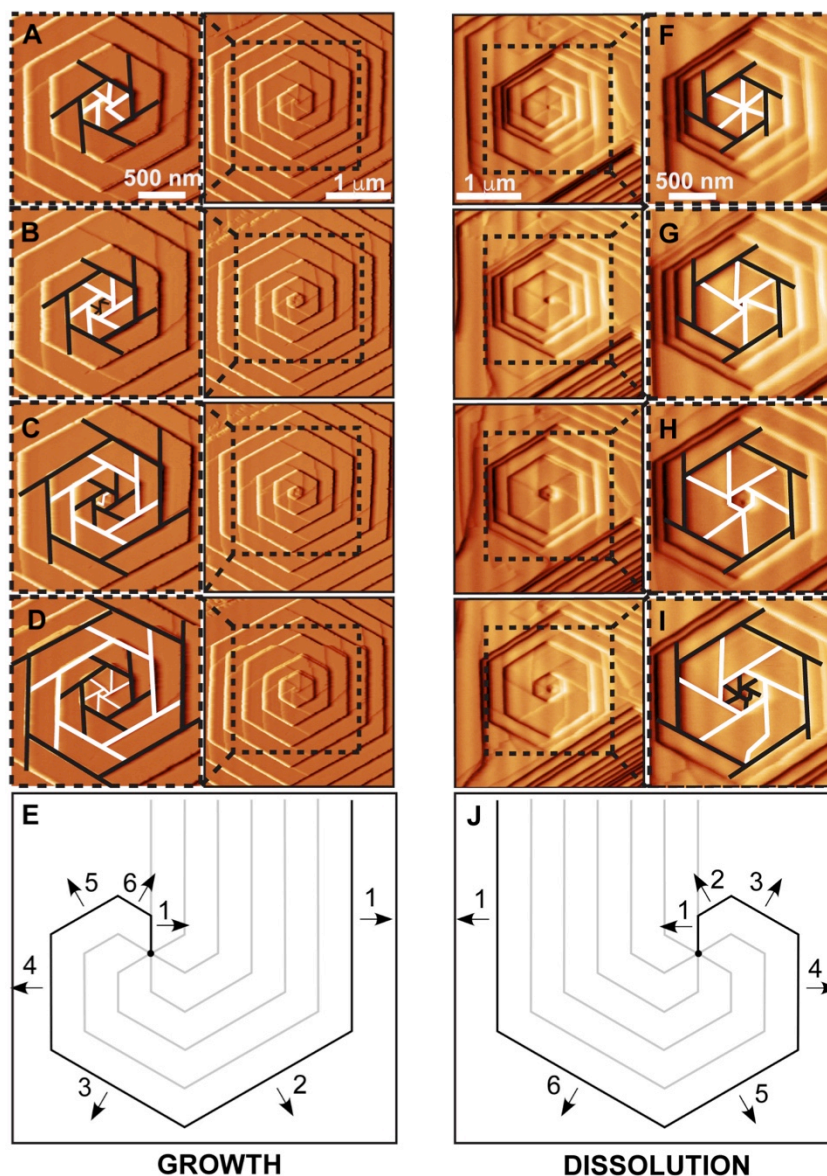
Figure 4.4. A series of AFM deflection images depicting the evolution of the hexagonal spiral morphology on the (0001) face of L-cystine during (A-D) growth (C_{bulk} = 2 mM) and (F-I) dissolution (C_{bulk} = 0.2 mM). The six minor steps and the bunched steps of each hillock are traced in white or black lines as a visual guide. The corresponding AFM images at large scan area are on the left and right, respectively. The panels at the bottom (E and J) illustrate the direction of minor step motion during growth and dissolution, revealing the opposite handedness of the dissolution spirals about the pinning point at the core. Arrows denote the directions of step motion, and numbers denote six crystallography unique step edges.

Dissolution of hexagonal L-cystine crystals was observed at $C_{bulk} \leq 0.5$ mM, below the equilibrium solubility of C_{sat} = 0.7 mM, accompanied by the formation of terraced hexagonal etch pits on the {0001} surface, each pit containing a single dislocation spiral (Figure 4.4F-I). Like the spirals observed during growth, the etch pits exhibit a pinwheel of six minor steps, each with a height of ca. 1 nm, radiating from a

dislocation hollow core (white and black traces in Figure 4.4F-I). The handedness of the dissolution spiral on *L*-cystine {0001}, however, is *opposite* to that of the growth spiral (Figure 4.4A-D). This corresponds to a direction of step motion during dissolution that is opposite to that during growth, leading to the observed reversal in handedness (Figure 4.4E and 4.4J). The retreating minor steps bunch to create a funnel-shaped pit with terraces defined by 6 nm-high major steps. Given the larger size of the crystals used for AFM measurement (ca. 100 μm wide vs. 20 μm for SICM), the time required for AFM measurements (2-3 hours), and the associated lower overall mass transport rates, the measurements most closely correspond to stage 2, as further confirmed below.

The molar dissolution rate of the {0001} crystal surface can be described as a flux ($J_\perp$) according to equation 4.10, wherein v_{step} is the retreating step velocity, L the step spacing, and h the bunched step height ($h \approx 6$ nm).[37,38] Figure 4.5 illustrates that v_{step} decreases linearly with increasing C_{bulk}. During growth, the value of L can be assumed to be constant for a given C_{bulk}[54] and to fall within a narrow range, from 250 to 350 nm, for $1 \leq C_{bulk} \leq 2$ mM.[7] However, for dissolution, values of L often were not uniform within the same pit over time (Figure 4.6), most likely due to transient changes in local mass transport, which contributes more significantly to the overall kinetics than for crystal growth (*vide supra*). Variations in L with time during dissolution are evident in Movies S1-S4. For the range of C_{bulk} investigated the step spacing varied from 100 to 400 nm during dissolution, giving rise to a spread of the dissolution rates of the {0001} face calculated with equation 4.10, and reflected in the rather large error bars in Figure 4.7. Nonetheless, there appears to be a linear dependence of the dissolution rate of the {0001} face on C_{bulk} (Figure 4.7).

$$J_\perp = (v_{step} \cdot \frac{h}{L}) / V_m \qquad\qquad (4.10)$$
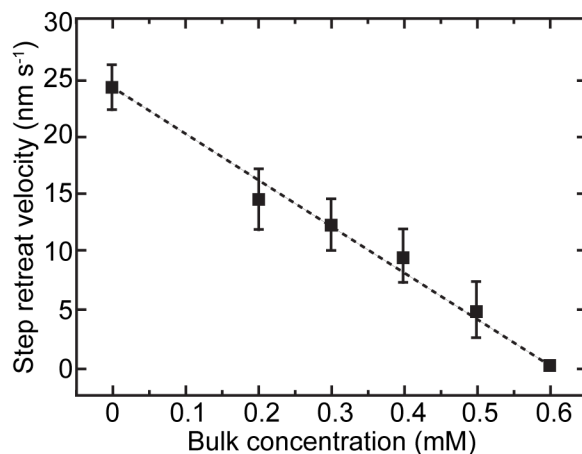
Figure 4.5. Dependence of the retreat velocities, v_{step}, of the {10$\bar{1}$0} major steps on L-cystine concentration, illustrating the linear increase of v_{step} with decreasing C_{bulk}. No dissolution was observed near the equilibrium solubility, C_{sat} = 0.7 mM.
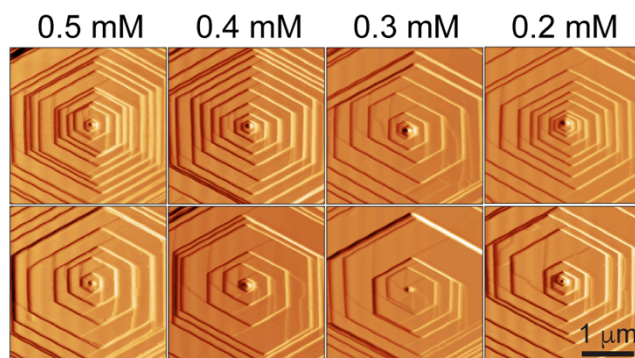
Figure 4.6. Real-time in situ AFM deflection images revealing non-uniform step spacing and step bunching on the (0001) L-cystine surface during dissolution (top and bottom) at various undersaturated L-cystine concentrations, as indicated above the top panels. The pair of images were obtained for the same etch pit, and selected to illustrate the most significant differences in step spacing observed at each concentration. Images were acquired from movies S1-S4.
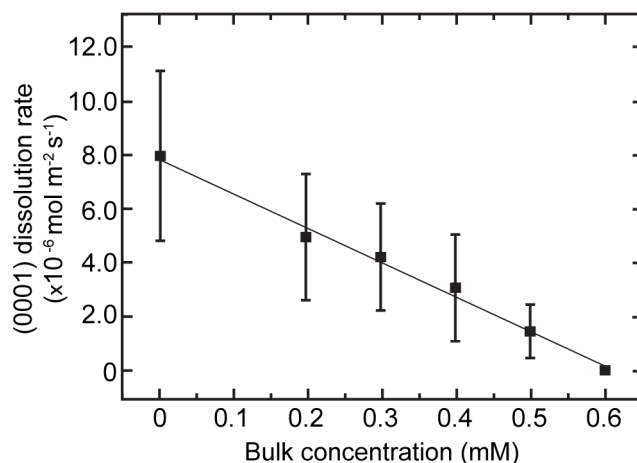
Figure 4.7. Dissolution rates of {0001} face calculated using eq. 4.10 measured at different L-cystine concentrations, as deduced from real time *in situ* AFM measurements of step velocities, step spacings, and step heights. The data reveal a linear relationship between dissolution rate and C_{bulk}.

3.3 Analysis of AFM Dissolution Kinetics and Mass Transport

FEM analysis has been used to examine mass transport in an AFM fluid cell for the growth of COM crystals[55] and for the dissolution of gypsum single crystals.[56] Both simulations revealed spatial heterogeneities in mass transport, with the AFM cantilever and tip blocking diffusion of solute molecules to the crystal during growth[55] and from the crystal during crystal dissolution (Figure 4.8).[56] The Reynolds number in the flow cell (Re = 11.5) was consistent with laminar flow and found to be similar to that reported earlier.[55] The gypsum investigation highlighted the importance of dissolution processes occurring outside the AFM scan area, denoted here as the region of interest (ROI). Dissolution can flood the ROI with solute molecules and increase C_{int} significantly. Ignoring this contribution can lead to the incorrect determination of the dissolution kinetics in the ROI.
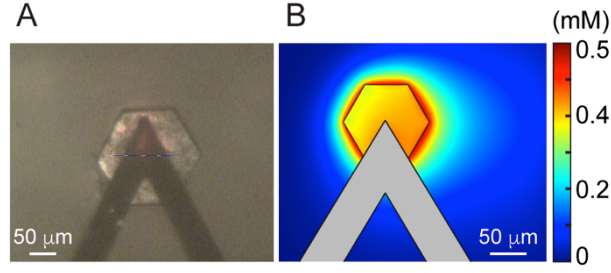
Figure 4.8. A typical experimental *in situ* AFM setup revealing an L-cystine crystal and AFM cantilever (A), and the computational geometry (B). The colors in panel B correspond to C_{int} calculated for a dissolution simulation at a flow rate of 15 mL/h, with $k^{int}_{\{10\bar{1}0\}}$ = 1.1 ×10^{-4} m/s and $k^{int}_{\{0001\}}$ = 2.4 ×10^{-5} m/s, and C_{bulk} = 0 mM.

FEM simulations were performed using the experimental flow rates of 15 mL/h, and C_{bulk} values of 0, 0.2, 0.3, 0.4, 0.5, and 0.6 mM. Dissolution rate laws for the exposed crystal faces, as deduced from the OM-SICM data, $J_\perp = k^{int}_{\{hkil\}}(C_{sat} - C_{int})$, with $k^{int}_{\{10\bar{1}0\}}$ = 1.1 ×10^{-4} m/s and $k^{int}_{\{0001\}}$ = 2.4 ×10^{-5} m/s, as obtained for stage 2, were applied. This stage was most relevant to the *in situ* AFM studies because the AFM images were acquired when the {0001} faces were decorated with etch pits and the {10$\bar{1}$0} faces were rounded (Figure 4.15, Supporting Information). Figure 4.9 illustrates the case of C_{bulk} = 0 mM; C_{int} is relatively high, signaling contributions from both mass transport and surface kinetics.

The model also reveals spatial heterogeneities in C_{int} at the {0001} face (Figure 4.9B), particularly at the AFM ROI, a 3 μm × 3 μm scanned area (Figure 4.9C). The interfacial L-cystine concentration is not uniform owing to the direction and magnitude of the solution flow and the presence of the AFM probe. Notably, advection from the flowing fluid decreases in areas near the cantilever, and the AFM cantilever and tip block the diffusion of L-cystine molecules from the crystal to the bulk solution. Therefore, compared with the area outside the ROI, the upstream region of the crystal, in contact with fresh solution, is characterized by a lower C_{int}, and the region under the AFM cantilever a higher C_{int} (lower mass transport rate) (Figure 4.9B). Furthermore, as the tip is scanning during an AFM experiment the non-uniform interfacial concentration would be expected to change with time, which may explain some of the variance in step density in consecutive images at constant bulk undersaturation (Figure 4.6).
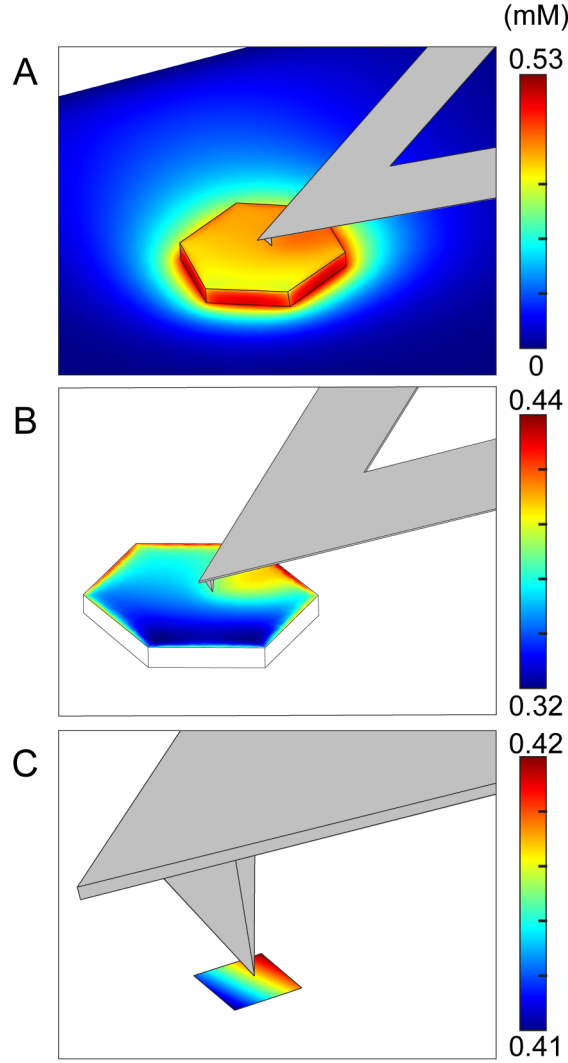
Figure 4.9. Simulations of the interfacial concentration and distribution of L-cystine during an in situ AFM dissolution experiment at different scales. (A) {10$\bar{1}$0} and {0001} faces and bulk solution; (B) the {0001} face and (C) the scanned area (i.e. the ROI) on the {0001} face. Kinetic parameters and flow rate are defined in the text.

This model provides the values of C_{int} within the AFM ROI simulated for each C_{bulk}, while taking into account the dissolution kinetics of the entire crystal (OM-SICM data). This permits the interfacial fluxes (Figure 4.7, *y*-ordinate) to be plotted against C_{int} at the AFM ROI (Figure 4.10). The value of $k_{\{0001\}}^{int}$ determined from the slope is 3.1 ($\pm$ 0.9) $\times 10^{-5}$ m/s, in good agreement with $k_{\{0001\}}^{int}$ obtained from OM-SICM data, 2.4 ($\pm$ 0.6) $\times 10^{-5}$ m/s. It is worth reiterating that the intrinsic dissolution flux normal to the {0001} face is deduced from AFM measurements of step velocities (and height/spacing) , whereas SICM measures the dissolution flux *on a larger lengthscale*

by recession of an entire surface. The similarity of the $k^{int}_{\{0001\}}$ values determined by the two methods is evidence that the step motion observed by AFM –- on a scale of few microns –- quantitatively captures the overall dissolution kinetics of this face when measured at a length scale of few hundred microns, revealing an essential link between microscopic and macroscopic behavior.
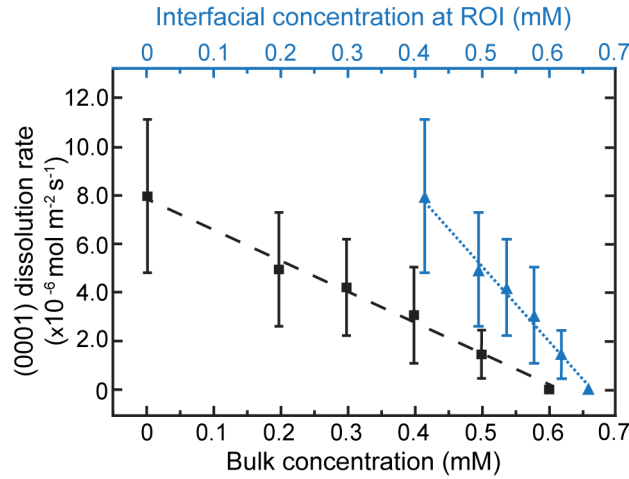
4.10. L-cystine {0001} dissolution rate ($J_{\perp}$) vs. L-cystine interfacial concentration at the AFM ROI, C_{int}, calculated from FEM simulations (blue triangles), and bulk concentration, C_{bulk} (black squares).

The calculated values of C_{int} range from 0.48 to 0.35 mM for solution flow rates increasing from 0 to 100 mL/h (C_{bulk} = 0 mM, and $k^{int}_{\{0001\}}$ = 2.4 ×10^{-5} m/s and $k^{int}_{\{10\bar{1}0\}}$ = 1.1 ×10^{-4} m/s, crystal size of 92 μm across and 10 μm crystal height, Figure 4.11) meaning that entirely surface kinetics limited dissolution can never be achieved in the AFM ROI for this system for any practically accessible flow rates. The dissolution process will always be in a mixed kinetic regime, $C_{bulk} < C_{int} < C_{sat}$, and mass transport cannot be ignored. Notably, C_{int} calculated from the FEM analysis exhibited a weak dependence on the flow rate (Figure 4.11), corresponding to small changes of v_{step} with increasing flow rate. A weak dependence of step velocity on flow rate has been used as an indicator of a kinetically controlled regime,[57,58] but this alone is not a sufficient criterion for proving the establishment of a kinetically-controlled regime.
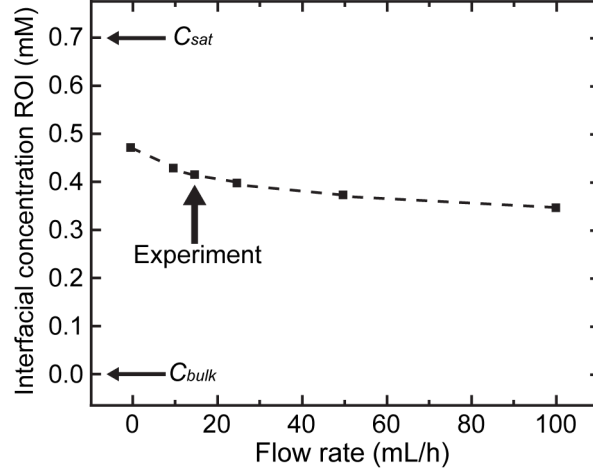
Figure 4.11. Dependence of the average L-cystine interfacial concentration, Cint, at the ROI on the flow rate, using the kinetic parameters and crystal size defined in the text. The arrow labeled 'Experiment' signifies the condition under which measurements were made. L-cystine solubility concentration, Csat, and bulk concentration, C_{bulk}, values have been indicated in the graph, illustrating that the dissolution process will always be in a mixed kinetic regime, $C_{bulk} < C_{int} < C_{sat}$.

Notably, the kinetic coefficient for dissolution of the $\{10\overline{1}0\}$ major steps, based on the vstep values measured by AFM and the driving force (C_{sat} - C_{bulk}), was βstep, dissolution = 3 ×10-4 m/s (eq 4.11a). This value is roughly four times larger than that measured under growth conditions, $\beta_{step,\ growth}$ = 7 ×10^{-5} m/s (eq 4.11b).[7] This comparison, however, does not account for the actual concentration at the dissolution or growth interfaces. This can be corrected for dissolution by replacing C_{bulk} in eq 4.11a with Cint calculated from the FEM analysis described above, resulting in a kinetic coefficient for dissolution of 6.7 ± 0.4 ×10^{-4} m/s. An equivalent analysis is not possible for growth, however, as Cint under growth conditions has not yet been determined.[7]

$$v_{step,dissolution} = \beta_{step,dissolution} V_m (C_{sat} - C_{bulk}) \qquad (4.11a)$$

$$v_{step,growth} = \beta_{step,growth} V_m (C_{bulk} - C_{sat}) \qquad (4.11b)$$

4. Conclusions

An in situ multi-microscopy approach (AFM and OM-SICM), coupled with FEM simulations, provides substantial insight into the mechanism and kinetics of the dissolution of hexagonal L-cystine crystals, in which mass transport and surface kinetic contributions can be separated, while demonstrating an essential link between microscopic and macroscopic behavior measured by AFM and SICM, respectively. This approach provides an accurate determination of the actual interfacial concentration during dissolution and a rare holistic view of crystal reactivity. Specifically, the dissolution of the $\{0001\}$ and $\{10\bar{1}0\}$ faces of L-cystine is characterized by a mixed regime with comparable contributions from surface kinetics and mass transport. The reduction in crystal size during dissolution is accompanied by the appearance of high index crystal faces, concomitant with an increase in the kinetic coefficient for detachment of L-cystine molecules from crystal sites and increasing mass transport control. Collectively, these results suggest a roadmap for the quantitative analysis of single crystal dissolution across multiple lengthscales.

5. Supporting Information
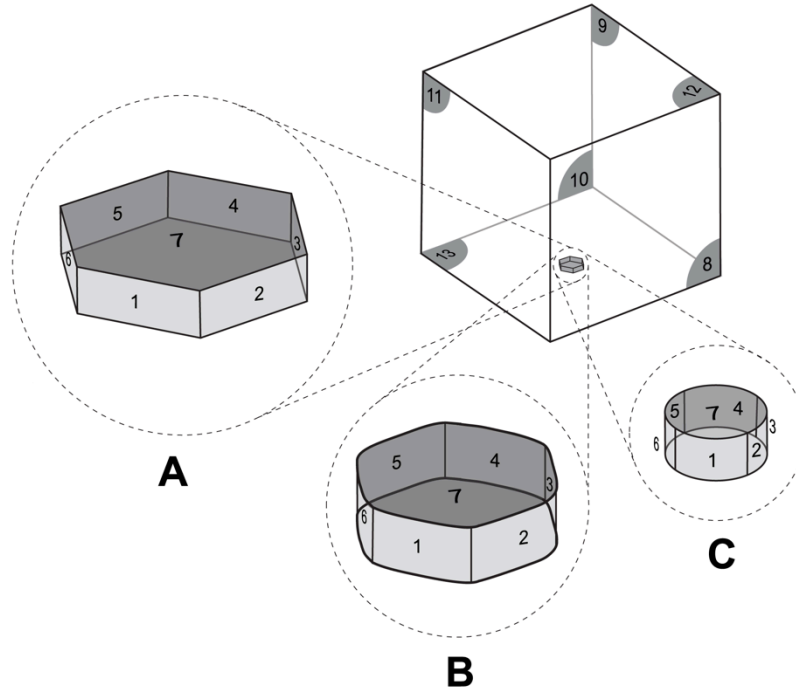
Figure 4.12. Three-dimensional domains used for FEM simulations of L-cystine dissolution in the OM-SICM experimental environment (A) EXP1 and MTM 1 models, (B) EXP2 and MTM2 models and (C) EXP3 and MTM3 models (not to scale). The numbers correspond to the boundaries described in Table 4.4.

Table 4.4. Boundary Conditions for Numerical Simulations of L-Cystine Dissolution Studies by OM-SICM.

Boundary	Characteristics	Boundary conditions EXP1-3	Boundary conditions MTM1-3
1, 2, 3, 4, 5, 6	$\{10\bar{1}0\}$ faces	$J_{(hkl)} = -\mathbf{n} \cdot (D\nabla c)$	$c = C_{sat}$
7	$\{0001\}$ face	$J_{(hkl)} = -\mathbf{n} \cdot (D\nabla c)$	$c = C_{sat}$
8, 9, 10, 11, 12	Bulk solution	$c = C_{bulk} = 0$	$c = C_{bulk} = 0$
13	Glass slide	$0 = -\mathbf{n} \cdot (D\nabla c)$	$0 = -\mathbf{n} \cdot (D\nabla c)$

The boundary numbers correspond to those depicted in Figure 4.12.

$\mathbf{n}$ = the vector normal to the surface

C_{sat} = solubility concentration of L-cystine (0.7 mM)

C_{bulk} = concentration of L-cystine in bulk solution
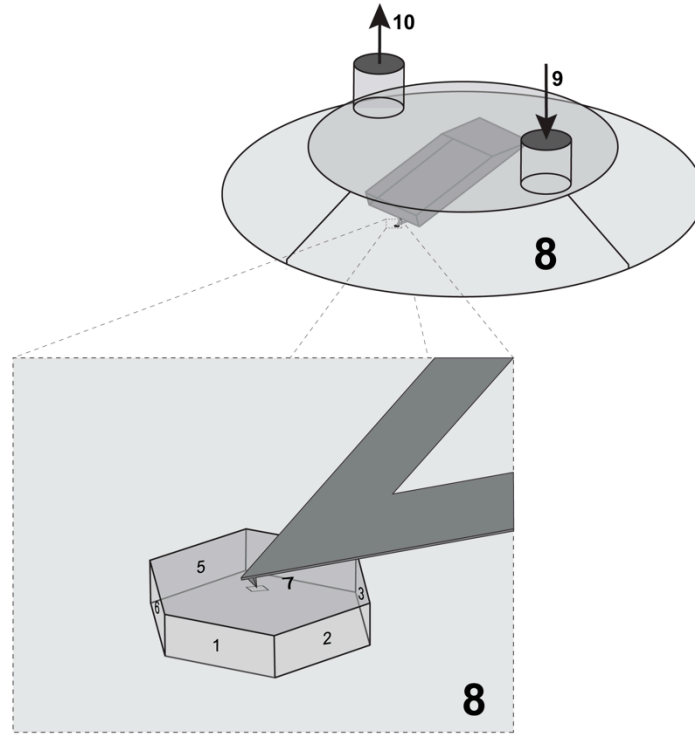
Figure 4.13. Three-dimensional representation of the AFM flow cell. The numbers represent the boundary conditions applied to numerical simulations described in Table S2.

Table 4.5. Boundary Conditions for Numerical Simulations of L-Cystine Dissolution Studies in the AFM flow cell

Boundary	Characteristics	Boundary conditions Convection	Boundary conditions Convective-diffusion mass transport
1, 2, 3, 4, 5, 6	$\{10\bar{1}0\}$ faces	$\mathbf{v} = 0$	$J_{(hkl)} = -\mathbf{n} \cdot (D\nabla c)$
7	$\{0001\}$ face	$\mathbf{v} = 0$	$J_{(hkl)} = -\mathbf{n} \cdot (D\nabla c)$
8	Flow cell walls	$\mathbf{v} = 0$	$J_{(hkl)} = -\mathbf{n} \cdot (D\nabla c)$
9	Flow cell inlet	$v_r = \dfrac{V_f}{\pi r_0^2}(1 - \dfrac{r^2}{r_0^2})$	$c = C_{bulk}$
10	Flow cell outlet	$p = 0$ $\mathbf{n} \cdot \eta \nabla^2 \mathbf{v} = 0$	$0 = -\mathbf{n} \cdot (D\nabla c)$

The boundary numbers correspond to those depicted in Figure 4.13.

$\mathbf{n}$ = the vector normal to the surface

r_0 = the inlet tube radius and r the radial coordinate with respect to the tube axis

C_{bulk} = the concentration of L-cystine in bulk solution
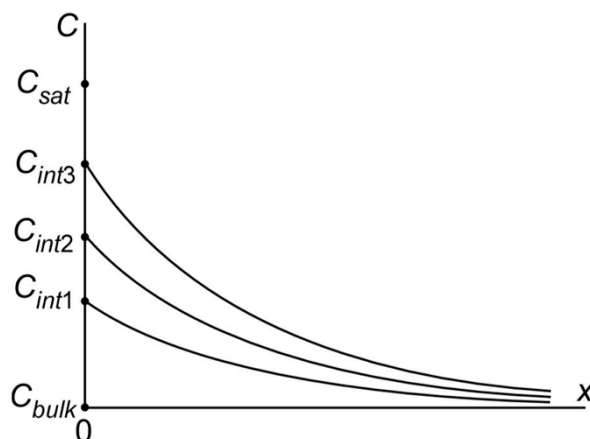
Figure 4.14. Schematic illustrating the effects of kinetic control on diffusion profiles. As the rate of detachment of L-cystine molecules from the crystal surface increases, the concentration at the interface (C_{int}) becomes higher and the diffusion profile becomes steeper, indicating a process increasingly limited by mass transport. C_{int} can approach, but never reach C_{sat}.

BEFORE DISSOLUTION   AFTER DISSOLUTION
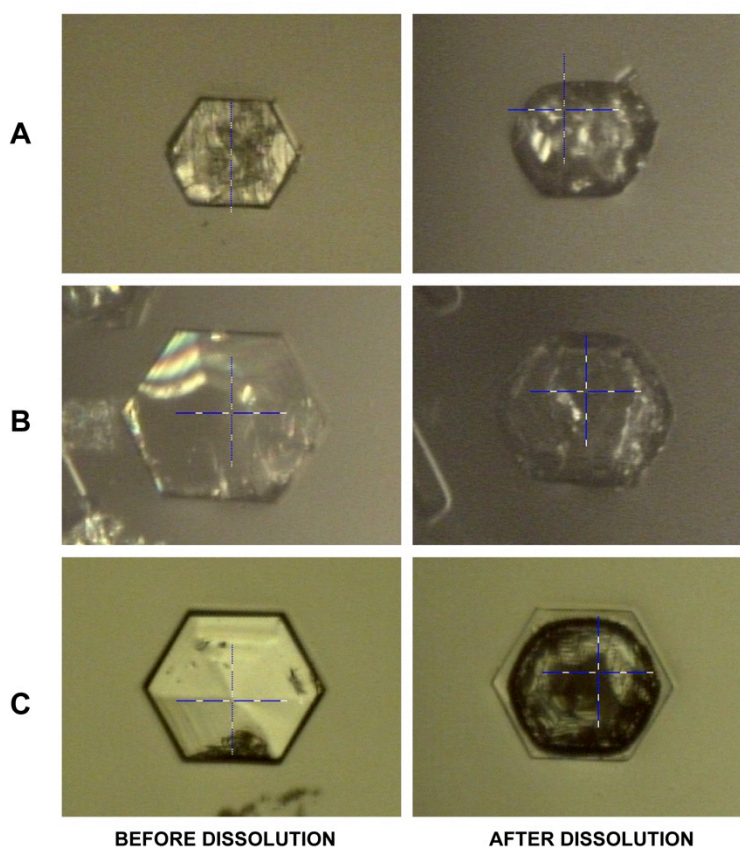
Figure 4.15. Optical micrographs of L-cystine crystals before and after *in situ* AFM dissolution experiments. During dissolution, crystal faces become rounded and the {0001} face shows the presence of etch pits.

Movies S1-S4 can be found in the enclosed CD

126

6. References

1.   Ahmed, K.; Dasgupta, P.; Khan, M. S. *Postgrad. Med. J.* **2006**, *82*, 799-801.

2.   Dolin, D. J.; Asplin, J. R.; Flagel, L.; Grasso, M.; Goldfarb, D. S. *J. Endourol.* **2005**, *19*, 429-432.

3.   Moe, O. W. *Lancet*, *367*, 333-344.

4.   Coe, F. L.; Asplin, J. R. *Science* **2010**, *330*, 325-326.

5.   Rimer, J. D.; An, Z.; Zhu, Z.; Lee, M. H.; Goldfarb, D. S.; Wesson, J. A.; Ward, M. D. *Science* **2010**, *330*, 337-341.

6.   Shtukenberg, A. G.; Zhu, Z.; An, Z.; Bhandari, M.; Song, P.; Kahr, B.; Ward, M. D. *Proc. Natl. Acad. Sci. U. S. A.* **2013**, *110*, 17195-17198.

7.   Shtukenberg, A. G.; Poloni, L. N.; Zhu, Z.; An, Z.; Bhandari, M.; Song, P.; Rohl, A. L.; Kahr, B.; Ward, M. D. *Cryst. Growth Des.* **2015**, *15*, 921-934.

8.   Mandal, T.; Shtukenberg, A. G.; Yu, A. C.; Zhong, X.; Ward, M. D. *Cryst. Growth Des.* **2016**, *16*, 423-431.

9.   Sahota, A.; Parihar, J. S.; Capaccione, K. M.; Yang, M.; Noll, K.; Gordon, D.; Reimer, D.; Yang, I.; Buckley, B. T.; Polunas, M.; Reuhl, K. R.; Lewis, M. R.; Ward, M. D.; Goldfarb, D. S.; Tischfield, J. A. *Urology* **2014**, *84*, 1249.e1249-1249.e1215.

10. Hu, L.; Yang, Y.; Aloysius, H.; Albanyan, H.; Yang, M.; Liang, J.-J.; Yu, A.; Shtukenberg, A.; Poloni, L. N.; Kholodovych, V.; Tischfield, J. A.; Goldfarb, D. S.; Ward, M. D.; Sahota, A. *J. Med. Chem.* **2016**, *59*, 7293-7298.

11. Becker, G. *Nephrology* **2007**, *12*, S21-S25.

12. Nakagawa, Y.; Asplin, J. R.; Goldfarb, D. S.; Parks, J. H.; Coe, F. L. *J. Urol.* **2000**, *164*, 1481-1485.

13. Chung, J.; Granja, I.; Taylor, M. G.; Mpourmpakis, G.; Asplin, J. R.; Rimer, J. D. *Nature* **2016**, *536*, 446-450.

14. Oughton, B. M.; Harrison, P. M. *Acta Crystallogr.* **1959**, *12*, 396-404.

15. Carta, R.; Tola, G. *J. Chem. Eng. Data* **1996**, *41*, 414-417.

16. Königsberger, E.; Wang, Z.; Königsberger, L.-C. *Monatsh. Chem.* **2000**, *131*, 39-45.

17. Liu, G.; Liu, J.; Sun, H.; Zheng, X.; Liu, Y.; Li, X.; Qi, H.; Bai, X.; Jackson, K. A.; Tao, X. *J. Am. Chem. Soc.* **2015**, *137*, 4972-4975.

18. Holden, M. A.; Cubillas, P.; Attfield, M. P.; Gebbie, J. T.; Anderson, M. W. *J. Am. Chem. Soc.* **2012**, *134*, 13066-13073.

19. Ward, M. D. *Science* **2005**, *308*, 1566-1567.

20. Dandekar, P.; Doherty, M. F. *Science* **2014**, *344*, 705-706.

21. Perrin, C. M.; Swift, J. A. *CrystEngComm* **2012**, *14*, 1709-1715.

22. Xu, M.; Higgins, S. R. *Geochim. Cosmochim. Acta* **2010**, *75*, 719-733.

23. McPherson, A.; Malkin, A. J.; Kuznetsov, Y. G. *Ann. Rev. Biophys. Biomol. Struct.* **2000**, *29*, 361-410.

24. Brent, R.; Cubillas, P.; Stevens, S. M.; Jelfs, K. E.; Umemura, A.; Gebbie, J. T.; Slater, B.; Terasaki, O.; Holden, M. A.; Anderson, M. W. *J. Am. Chem. Soc.* **2010**, *132*, 13858-13868.

25. Unwin, P. R.; Macpherson, J. V. *Chem. Soc. Rev.* **1995**, *24*, 109-119.

26. Dove, P. M.; Platt, F. M. *Chem. Geol.* **1996**, *127*, 331-338.

27. Adobes-Vidal, M.; Maddar, F. M.; Momotenko, D.; Hughes, L. P.; Wren, S. A. C.; Poloni, L. N.; Ward, M. D.; Unwin, P. R. *Cryst. Growth Des.* **2016**, 4421-4429.

28. Hansma, P. K.; Drake, B.; Marti, O.; Gould, S. A.; Prater, C. B. *Science* **1989**, *243*, 641-643.

29. Peruffo, M.; Mbogoro, M. M.; Edwards, M. A.; Unwin, P. R. *Phys. Chem. Chem. Phys.* **2013**, *15*, 1956-1965.

30. Perry, A. R.; Peruffo, M.; Unwin, P. R. *Cryst. Growth Des.* **2013**, *13*, 614-622.

31. Nadappuram, B. P.; McKelvey, K.; Al Botros, R.; Colburn, A. W.; Unwin, P. R. *Anal. Chem.* **2013**, *85*, 8070-8074.

32. McKelvey, K.; Perry, D.; Byers, J. C.; Colburn, A. W.; Unwin, P. R. *Anal. Chem.* **2014**, *86*, 3639-3646.

33. Novak, P.; Li, C.; Shevchuk, A. I.; Stepanyan, R.; Caldwell, M.; Hughes, S.; Smart, T. G.; Gorelik, J.; Ostanin, V. P.; Lab, M. J.; Moss, G. W. J.; Frolenkov, G. I.; Klenerman, D.; Korchev, Y. E. *Nat. Methods* **2009**, *6*, 279-281.

34. Yang, X.; Liu, X.; Zhang, X.; Lu, H.; Zhang, J.; Zhang, Y. *Ultramicroscopy* **2011**, *111*, 1417-1422.

35. Wilke, C. R.; Chang, P. *AIChE J.* **1955**, *1*, 264-270.

36. Hayduk, W.; Laudie, H. *AIChE J.* **1974**, *20*, 611-615.

37. Vekilov, P. G.; Ataka, M.; Katsura, T. *J. Cryst. Growth* **1993**, *130*, 317-320.

38.   Colombani, J.; Bert, J. *Geochim. Cosmochim. Acta* **2007**, *71*, 1913-1920.

39.   Momotenko, D.; McKelvey, K.; Kang, M.; Meloni, G. N.; Unwin, P. R. *Anal. Chem.* **2016**, *88*, 2838-2846.

40.   Prasad, K. V. R.; Ristic, R. I.; Sheen, D. B.; Sherwood, J. N. *Int. J. Pharm.* **2002**, *238*, 29-41.

41.   Burt, H. M.; Mitchell, A. G. *Int. J. Pharm.* **1981**, *9*, 137-152.

42.   Chernov, A. A. *Contemp. Phys.* **1989**, *30*, 251-276.

43.   Lasaga, A. C.; Luttge, A. *Science* **2001**, *291*, 2400-2404.

44.   Hartman, P.; Perdok, W. G. *Acta Crystallogr.* **1955**, *8*, 521-524.

45.   Hartman, P.; Perdok, W. G. *Acta Crystallogr.* **1955**, *8*, 49-52.

46.   Sangwal, K. *Etching of Crystals: Theory, experiment, and application*; North-Holland Amsterdam: Amsterdam, NL, 1987; Vol. 497.

47.   Lasaga, A. C. *Kinetic Theory in the Earth Sciences*; Princeton University Press, 1998.

48.   Nielsen, A. E. *J. Cryst. Growth* **1984**, *67*, 289-310.

49.   Burton, W. K.; Cabrera, N.; Frank, F. C. *Philos. Trans. R. Soc., A* **1951**, *243*, 299-358.

50.   Macpherson, J. V.; Unwin, P. R. *J. Phys. Chem.* **1994**, *98*, 1704-1713.

51.   Macpherson, J. V.; Unwin, P. R. *J. Phys. Chem.* **1996**, *100*, 19475-19483.

52.   Christoffersen, J.; Christoffersen, M. R. *J. Cryst. Growth* **1988**, *87*, 41-50.

53.   Perry, A. R.; Lazenby, R. A.; Adobes-Vidal, M.; Peruffo, M.; McKelvey, K.; Snowden, M. E.; Unwin, P. R. *CrystEngComm* **2015**, *17*, 7835-7843.

54.   Cabrera, N.; Levine, M. M. *Philos. Mag.* **1956**, *1*, 450-458.

55.   Gasperino, D.; Yeckel, A.; Olmsted, B. K.; Ward, M. D.; Derby, J. J. *Langmuir* **2006**, *22*, 6578-6586.

56.   Peruffo, M.; Mbogoro, M. M.; Adobes-Vidal, M.; Unwin, P. R. *J. Phys. Chem. C* **2016**, *120*, 12100-12112.

57.   Bracco, J. N.; Gooijer, Y.; Higgins, S. R. *Geochim. Cosmochim. Acta* **2016**, *183*, 1-13.

58.   Urosevic, M.; Rodriguez-Navarro, C.; Putnis, C. V.; Cardell, C.; Putnis, A.; Ruiz-Agudo, E. *Geochim. Cosmochim. Acta* **2012**, *80*, 1-13.

| **Chapter V** | **Tracking the Dissolution of Calcite Single Crystals in Acid Waters: A Simple Method for Measuring Fast Surface Kinetics** |

Abstract

Although the dissolution kinetics of calcite in acid waters has been studied for more than a century, the process is not fully understood, and for particles and microcrystals the process is often assumed to be diffusion-controlled. Herein, the dissolution kinetics of calcite single microcrystals in aqueous solution (pH *ca.* 3) has been investigated for the first time by a combination of real-time optical microscopy coupled with numerical simulations. The small size and well-defined geometry of rhombohedral calcite single crystals enables the measurement of the dissolution rates of the individual crystal faces exposed to the solvent and an assessment of the relative importance of corners and edges compared to the {104} faces. Data are used to parameterize finite element method (FEM) models for the quantitative analysis of dissolution kinetics. The simulations provide an accurate determination of the near-interface concentration of solution species during dissolution, as well as concentration gradients. The intrinsic first-order dissolution rate constant for the attack of protons on the exposed {104} faces, k_{surf} = 6.4 (± 2.8) ×10^{-4} m s^{-1}, is in good agreement with previous microscopic and macroscopic measurements, corroborating the method. This study is a further demonstration of the power of simple *in-situ* optical microscopy for quantitative interfacial (dissolution/growth) kinetic measurements, using a configuration of practical relevance for processes as diverse as the remediation of acid water and scale removal.

1. Introduction

Calcite crystal dissolution and growth have been extensively studied for more than a century,[1] since they are crucial processes involved in many important geochemical phenomena, such as the formation of karst in limestone terrains, the neutralization of acidic lakes, and the global cycling of CO_2. Calcite is also very relevant in industrial processes as it is the main component in scaling corrosion of pipes, among others.[2] However, despite the environmental and industrial significance, calcite dissolution and growth are still not fully comprehended because these are complex physicochemical processes involving mass transport and coupled chemical reactions in solution.[3]

The dissolution process is recognized to be strongly dependent on pH[4, 5] and has been investigated in many experimental formats, ranging from bulk suspensions of powders[5-7] to cleaved single crystals surfaces[8-12] and monitoring step velocities and etch pit formation on cleaved surfaces by *in situ* atomic force microscopy (AFM).[13-18] For pH < 4, most techniques find that calcite dissolution rates are controlled by the diffusion of protons to the surface.[4, 5, 11] Indeed, the process is so fast, that measuring the intrinsic surface dissolution kinetics has proved to be rather challenging[8, 9, 19, 20] and only a few techniques, namely the channel flow method with electrochemical detection (CFMED),[1, 21] *in-situ* AFM using a specially designed fast-flow cell[22] and scanning electrochemical microscopy (SECM),[23] have been capable of measuring the intrinsic dissolution rate constant of calcite in acid water. The results obtained by these three different techniques are in broad agreement, but require rather sophisticated setups with flow systems and specialized sensors,[1, 21] detailed analysis of the hydrodynamics[22] or even *ex-situ* characterization of the topographical changes on the crystal surface in order to deduce surface kinetics.[23] Moreover, these methods focus on individual crystal faces, but for a number of applications (*vide infra*) it would be more appropriate to track the behaviour of an entire microcrystal (faces and edges), which is the motivation for the studies herein.

Very recently, we have demonstrated that studying the morphological changes of microscale single crystals using *in-situ* microscopy techniques in combination with finite element method (FEM) simulations is a very powerful approach for measuring interfacial dissolution/growth kinetics.[24-26] This approach: (i) provides the possibility

of generating high mass transport (diffusion) rates, much higher than achievable with fast flow systems[1, 21, 22] or the rotating disc method;[9, 12, 19, 20] (ii) results in chemostatic control of the reaction conditions; (iii) tracks all of the individual crystal faces and edges exposed to the solvent simultaneously; and (iv) quantifies interfacial fluxes and concentration distributions to elucidate the kinetic regime.

Herein, we demonstrate the versatility of the method and its capabilities for studying fast kinetic processes, investigating the dissolution of rhombohedral calcite single microcrystals at pH = 3.1. This configuration is directly relevant to practical applications, such as the treatment of acid water with calcite particulates,[27, 28] or the removal of scale from surfaces.[29-31] The results herein show that in this configuration, surface kinetics contribute significantly to the dissolution kinetics, i.e. calcite microcrystals dissolve at slower rates than predicted by these models. This work is important because recent studies and analyses of proton-promoted calcite dissolution in such systems still consider the process to be diffusion-controlled.[9, 19, 32-34]

2. Experimental

2.1 Samples and Solutions

All solutions were prepared fresh on the day of use, with ultrapure water produced by a Purite Select HP system with a typical resistivity of 18.2 MΩ cm (25 °C). Calcite microcrystals were prepared by mixing equal volumes of 5 mM $CaCl_2$ (Sigma-Aldrich, AR grade) and 10 mM $NaHCO_3$ (Sigma-Aldrich, AR grade) solutions in a 35 mm diameter polystyrene Petri dish (Greiner Bio-One International GmbH, Austria) to create a supersaturated solution. The dish was then covered, and allowed to stand at room temperature for 24 hours. The supernatant solution was subsequently removed to reveal small transparent calcite rhombohedrons, with sides typically <40 μm, attached to the bottom of the Petri dish.

2.2 Dissolution Studies

After careful rinsing with ultrapure water and drying with a nitrogen stream, the Petri dish containing the calcite crystals was placed on an inverted optical microscope (Axiovert 40 CFL, Zeiss, Germany) equipped with an LED light source to reduce sample heating and a video camera (B700, PixeLINK) to assist the selection and
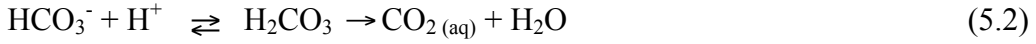
monitoring of a particular crystal. All dissolution studies were performed in 0.8 mM HCl (made from Sigma-Aldrich, 37% reagent grade) and 50 mM KCl (Sigma-Aldrich, AR grade) as background electrolyte at 25 °C. Solution pH (3.1) was measured with a pH meter (Metler Toledo, Switzerland). This simplified the modeling (spatially invariant activity coefficients for all reactive species), and allowed direct comparison of the results with previous studies on individual crystal faces. [1, 21-23]

The approach described requires that the height of the crystal is known at the start of the experiment. For the crystal sizes herein, simply focusing on the top microcrystal face and Petri dish base would give this dimension with sufficient accuracy (± 1 μm), but for higher accuracy, we used home-built scanning ion-conductance microscopy, as a system was installed on the stage of the optical microscope. This provided a measure of the crystal height at the start of the experiment as previously described.[24, 26, 35] Diffusionally isolated calcite crystals (separated more than 40× times their largest dimension from neighbouring crystals) with the longest side of 36 ± 4 μm and height of 21 ± 2 μm were studied (total of 10 individual crystals in separate experiments). Following the addition of 4 mL of the acidic solution, a time-lapse sequence of optical images (40× lens magnification, every 30 s) was acquired and the dissolution velocities of the characteristic {104} faces of rhombohedral calcite were determined by measuring the crystal dimensions using ImageJ (version 1.45, NIH). In addition, the optical approach obviously revealed any change in morphology.

2.3 FEM Simulations

Numerical simulations were performed using the transport of diluted species module of the commercial finite element method (FEM) modeling package Comsol Multiphysics 5.2 (Comsol AB, Sweden). Three-dimensional models were formulated using inputs from experimental data to estimate the interfacial concentration of species during the dissolution process and determine the dissolution rate constant of the first-order heterogeneous reaction in terms of interfacial proton concentration.[1, 22, 23]

The models simulate the mass transport of species during the dissolution of a calcite crystal in a quiescent solution at pH 3.1. At this pH, the proton-promoted dissolution process at the crystal surface can be described by (eq. 5.1 and 5.2):[1, 5]

$$CaCO_3 + H^+ \ \rightleftharpoons \ Ca^{2+} + HCO_3^- \tag{5.1}$$

$$HCO_3^- + H^+ \ \rightleftharpoons \ H_2CO_3 \ \rightarrow CO_{2\,(aq)} + H_2O \tag{5.2}$$

The models also take account of chemical equilibria in the solution that are relevant under the conditions of our experiment[35, 36] (Table 5.1). These reactions are expressed in the simulations by activity corrected mass action rate equations[23, 37] and the rate constants are defined to be fast enough to maintain the solution processes at equilibrium at a particular point in space. The mass transport of species is governed exclusively by diffusion and assumed to be effectively at a steady-state, for which the following is solved (eq. 5.3):

$$\nabla J_i = \nabla \cdot (D_i \nabla c_i) + R_i = 0 \tag{5.3}$$

where J_i is the flux, D_i is the diffusion coefficient, c_i is the concentration of species i, and R_i is the reaction rate expression for the species i. The use of a steady-state model is appropriate because the characteristic diffusional time for the mass transport of protons from bulk solution to the microscopic crystal surface, estimated using a semi-infinite diffusion model according to eq. 5.4, is about 0.14 s, which is 4 orders of magnitude faster than the duration of a typical crystal dissolution experiment (30 min for the complete dissolution of a crystal). $t_{diff,\,i}$ denotes the steady-state diffusion time and d is crystal largest dimension size.

$$t_{diff,\,i} \approx \frac{d^2}{D_i} \tag{5.4}$$

The diffusion coefficients of the individual species at infinite dilution were obtained from the literature[36] and corrected for the ionic concentration in bulk solution. Diffusion coefficients were assumed to be constant over the entire domain (Table 5.2).

Table 5.1. Equilibrium Reactions for the Calcite-Water System open to the Atmosphere.

Reaction	$pK_{eq}^{*\,36}$
$H_2O \rightleftharpoons H^+ + OH^-$	14
$CO_{2\,(aq)} + H_2O \rightleftharpoons H_2CO_3$	1.446
$CO_3^{2-} + H^+ \rightleftharpoons HCO_3^-$	-10.33
$HCO_3^- + H^+ \rightleftharpoons H_2CO_3^{\circ}$	-6.35
$Ca^{2+} + CO_3^{2-} \rightleftharpoons CaCO_{3\,(aq)}$	-3.20
$Ca^{2+} + HCO_3^- \rightleftharpoons CaHCO_3^+$	-1.00

* Value before activity correction

$H_2CO_3^{\circ}$ signifies the total concentration of dissolved carbonate in the form CO_2 and H_2CO_3

Table 5.2. Diffusion Coefficients of the Species Considered in the FEM Model.

Species	Ca^{2+}	CO_3^{2-}	HCO_3^-	H_2CO_3	$CaCO_3$	$CaHCO_3^+$	H^+	OH^-
$D\,(\times10^{-9}\,m^2\,s^{-1})$	0.760	0.886	1.137	1.137	0.818	1.039	8.939	5.062

The three-dimensional domain used in the simulations is shown in Figure 5.1 and was parameterized with the average crystal dimensions and geometry of ten independent crystals determined by optical microscopy and scanning ion conductance microscopy. The models simulated the dissolution process described in eq. 5.1-5.2 and were developed by applying a flux of protons into the calcite surface that causes a release of calcium and bicarbonate ions, representing the flux of species leaving the dissolving crystal faces. The model, denoted here as Model 1, used as the flux value for each individual crystal face, the experimental dissolution rate of the {104} face, J_{obs}, obtained from the time-lapse optical images. The model designated Model 2, defined the flux of species to and from the crystal surface as a result of a first-order process in near-surface (*surf*) proton concentration,[1, 22, 23] applying eq. 5.5, where k_{surf} is the intrinsic dissolution rate constant.

$$J_i = k_{surf}[H^+]_{surf} \tag{5.5}$$

Using appropriate boundary conditions (Table 5.3), the concentrations of species near the calcite-solution interface and in the solution around the dissolving crystal were simulated and the results obtained from each model were compared. The solutions of the partial differential equations for both models were acquired using the direct solver MUMPS in the Comsol environment, with a relative error tolerance of 10^{-6}. Simulations were carried out with optimized tetrahedral mesh elements.
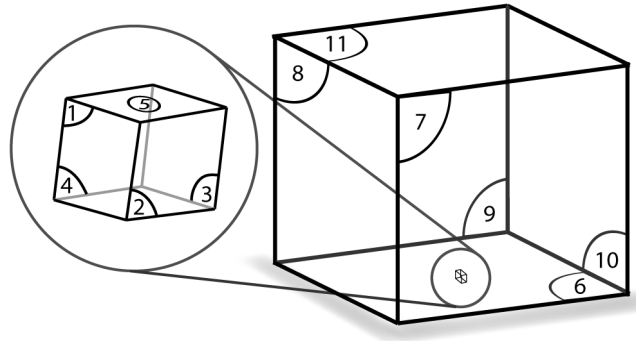
Figure 5.1. Three-dimensional domain used for FEM simulations (not to scale). The numbers correspond to the boundaries described in Table 5.3.

Table 5.3. Boundary Conditions used in the FEM Simulations

Boundary	Characteristics	Conditions Model 1	Conditions Model 2
1-5	Calcite {104} face	$\mathbf{n} \cdot D_{H^+} \nabla c_{H^+} = J_{obs}$ $-\mathbf{n} \cdot D_{Ca^{2+}} \nabla c_{Ca^{2+}} = J_{obs}$ $-\mathbf{n} \cdot D_{HCO_3^-} \nabla c_{HCO_3^-} = J_{obs}$	$\mathbf{n} \cdot D_{H^+} \nabla c_{H^+} = k_{surf}[H^+]_{surf}$ $-\mathbf{n} \cdot D_{Ca^{2+}} \nabla c_{Ca^{2+}} = k_{surf}[H^+]_{surf}$ $-\mathbf{n} \cdot D_{HCO_3^-} \nabla c_{HCO_3^-} = k_{surf}[H^+]_{surf}$
6	Petri dish surface	$\mathbf{n} \cdot D_i \nabla c_i = 0$	$\mathbf{n} \cdot D_i \nabla c_i = 0$
7-11	Bulk solution	$c_i = c_{i,bulk}$	$c_i = c_{i,bulk}$

The boundary numbers are in accordance with the boundaries defined in Figure 5.1
$\mathbf{n}$ denotes the vector normal to the surface
$c_{i,bulk}$ is the bulk concentration of the species i governed by the equilibrium reactions in Table 5.1

2.4 Speciation Computations

The initial concentration of species in bulk solution, $c_{i,\,bulk}$, was calculated using the speciation software MINEQL+[38, 39] (version 4.6, Environmental Research Software). The simulations considered a system open to the atmosphere where $PCO_2 = 10^{-3.5}$ atm;[40] the temperature was fixed at 25 ºC, the ionic strength was calculated by the software and the pH was computed satisfying electroneutrality conditions. The simulated pH (pH = 3.1) was in agreement with the experimental data, confirming the validity of the speciation calculations. The concentrations of the relevant species are listed in Table 5.4.

Table 5.4. Concentration of Species in Bulk Solution

Species	Concentration (mM)
H^+	0.808
OH^-	1.87×10^{-8}
Ca^{2+}	0
Cl^-	50.8
K^+	50
CO_3^{2-}	1.16×10^{-12}
HCO_3^-	9.03×10^{-6}
H_2CO_3	0.011
$CaCO_3$	0
$CaHCO_3^+$	0
pH	3.1

3. Results and Discussion

3.1 Dissolution Rates of Rhombohedral Calcite Crystals

Crystals grown by the precipitation method described in the experimental section were inspected by optical microscopy. As mentioned above, the calcite crystals studied were of 36 ± 4 μm side length and 21 ± 2 μm in height. The similarity of the sizes of the ten crystals allowed data to be pooled to improve the statistics. It can be seen from Figure 5.2 that the crystal habit forms a rhombohedron with angles 78° and 102°, representative of the intersection of {104} faces. The {104} faces are the most stable facets of calcite crystals due to the neutrality and flat ion arrangement and are kinetically favoured from pure aqueous solutions as they are the slowest growing faces.[41, 42]
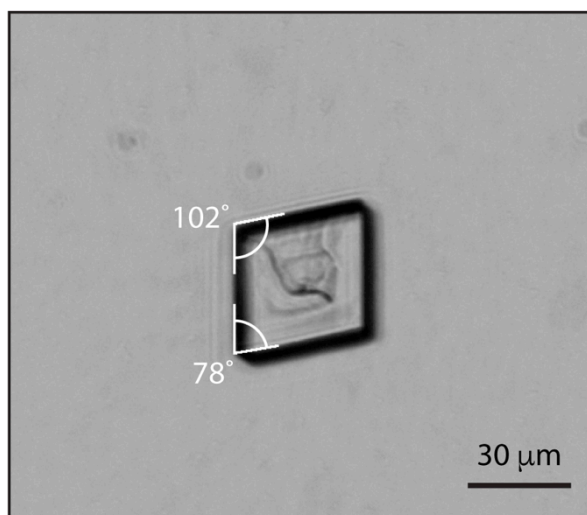
Figure 5.2. Typical morphology of a grown calcite crystal for dissolution studies. The intersection of the crystal faces produces angles of 102° and 78° confirming that the dominant crystal faces are the {104} faces.

The crystal dimensions prior to the dissolution studies were acquired as described in our previous work[24, 26] by the combination of optical and scanning ion conductance microscopy. Since all the facets of the exposed crystal habit are equivalent, it is reasonable to assume that all faces will exhibit the same dissolution rate, a fact that could be confirmed for opposite pairs of side faces. Thus, it is possible to extrapolate the results obtained by 2D optical microscopy to all the crystal faces exposed to the solvent and identify the 3D changes in crystal size. Time-lapse images acquired

during the dissolution of a typical calcite crystal are shown in Figure 5.3A. Initially, the rhombohedral calcite crystals have sharp edges and corners. However, as the crystal dissolves, the edges and corners start rounding, and rounding increases with dissolution time until the crystals become spherical towards the end of the process. Figure 5.3D shows the evolution of the crystal circularity (2D projection) as a function of dissolution time calculated by eq. 5.6. The maximum circularity value of one indicated a perfect circle.

$$Circularity = 4\pi \frac{Area}{Perimeter} \tag{5.6}$$

This observation indicates that during dissolution the crystal units are preferably removed from the edges and corners because the step and kink density is higher relative to the smooth terraces characterizing the faces,[43, 44] while at the same time such features experience a higher diffusive flux of material (if the faces are not diffusive sink/sources).

Figure 5.3B shows plots of the average displacement of the {104} faces (edge to centre distance) as a function of time, determined from data acquired for the ten crystals studied. Under purely diffusion control conditions, the displacement of the {104} face would depend on the square root of dissolution time as described by eq. 5.7, deduced from the solution of Fick's second law for spherical isotropic diffusion at steady-state, where r denotes the radius of the sphere (calcite microcrystal) and t specifies time. The constant parameter, a, depends on the values of the concentration and diffusion coefficient of the reacting species and the molar volume of calcite.[45]
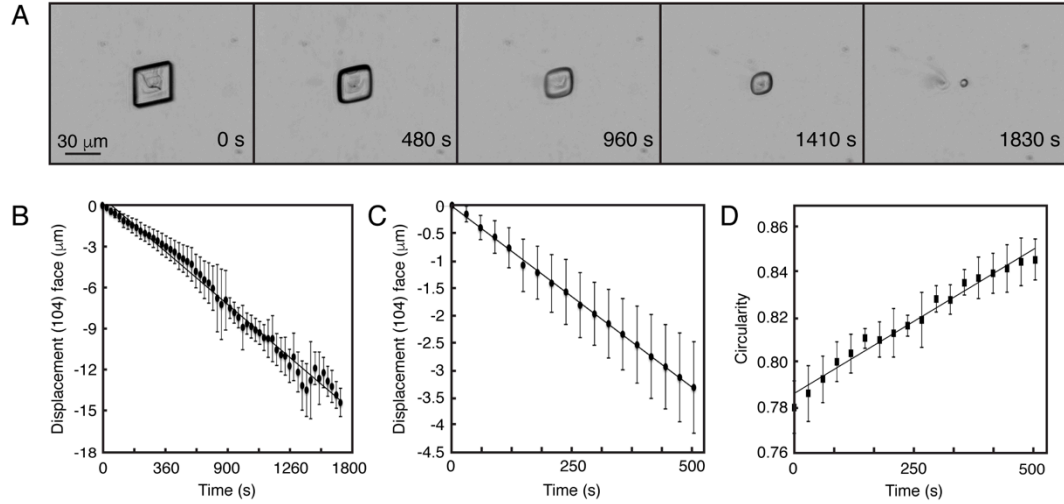
Figure 5.3. (A) Representative time-lapse optical microscopy images of the dissolution of a calcite microcrystal in aqueous solution at pH = 3.1. (B) Plot of the average displacement of the {104} faces over time. (C) Plot of the average displacement of the {104} faces during the first 510 s of dissolution. (D) Plot showing the average changes in circularity of calcite crystals during the first 510 s of dissolution.

In contrast, there is a strong linear dependence of the {104}-face displacement on the dissolution time, suggesting significant surface control,[45] although the accuracy of the data is degraded towards the end of the process due to the resolution limits of the optical microscope. Only the early stage of dissolution (Figure 5.3C), where the crystal morphology and dissolution rate was most accurate, was analysed to obtain insights into the dissolution kinetics by FEM simulations since the linear dependence on the {104}-face displacement on the dissolution time alone is not always an indicative of surface control, especially when focusing in short periods of time. A quantitative determination of the dissolution kinetics is shown below by FEM simulations, which highlight a mixed kinetic regime.

$$r = \sqrt{2a \cdot t} \tag{5.7}$$

The molar dissolution rate of the {104} faces, J_{obs}, was determined using eq. 5.8, where $v_{\{104\}}$ is the retreat velocity of the lateral faces during the first 510 s of the dissolution process (determined from the slope of the displacement *vs.* time plots), and $\overline{V}$ is the molar volume of calcite (36.9 cm^3 mol^{-1}).[45] The calculated value of J_{obs} was 1.77 ($\pm$ 0.38) $\times 10^{-4}$ mol m^{-2} s^{-1}, in agreement with the dissolution fluxes (> 10^{-4} mol m^{-2} s^{-1}) reported from SECM experiments of individual calcite crystal faces

(natural Iceland Spar crystals), where a very high flux of protons produced at an ultramicroelectrode (UME) induced the dissolution of a calcite surface.[23] This exhibits the key feature of our approach, which is that isolated microcrystals in solution generate high mass transport (diffusion) rates during dissolution to enable the kinetics of rapid surface processes to be accessed.

$$J_{obs} = v_{\{104\}} / \overline{V} \tag{5.8}$$

3.2 Determination of Interfacial Concentrations and the Intrinsic Dissolution Rate Constant

Three-dimensional FEM models were formulated using experimental data (interfacial dissolution flux) as an input to obtain the near-interface concentration of species during the dissolution process and determine the dissolution rate constant of the first-order heterogeneous reaction in terms of interfacial proton concentration.

Model 1 was parameterized using the initial rhombohedral geometry with the average size and initial dissolution rate (first 510 s) obtained for the ten different crystals. The simulation produced the concentration distribution of all the chemical species around the dissolving crystal, such that concentration profiles of any species from the crystal surface to bulk solution could be analysed. The concentration profiles of the most relevant species involved in the dissolution of calcite in acidic aqueous solution in the vertical direction from the centre of the crystal surface are plotted in Figure 5.4. It is evident that the near-interface proton concentration is lower than in bulk solution, which is consistent with the protons being consumed in the dissolution process. On the other hand, the concentration of calcium ions and dissolved inorganic carbon (DIC), defined as the sum of H_2CO_3, HCO_3^- and CO_3^{2-} species, is higher at the crystal/solution interface, since Ca^{2+} and HCO_3^- are liberated from the crystal surface due to proton attack, and the release of HCO_3^- produces an increment of H_2CO_3 and CO_3^{2-} in order to maintain equilibrium conditions. The average concentration of protons simulated at the crystal/solution interface is 0.27 mM, a clear illustration that the process is not simply diffusion-controlled, as still widely adopted in the literature,[9, 19, 32-34] for which $[H^+]_{surf} \approx 0$ mM would be observed.[4]
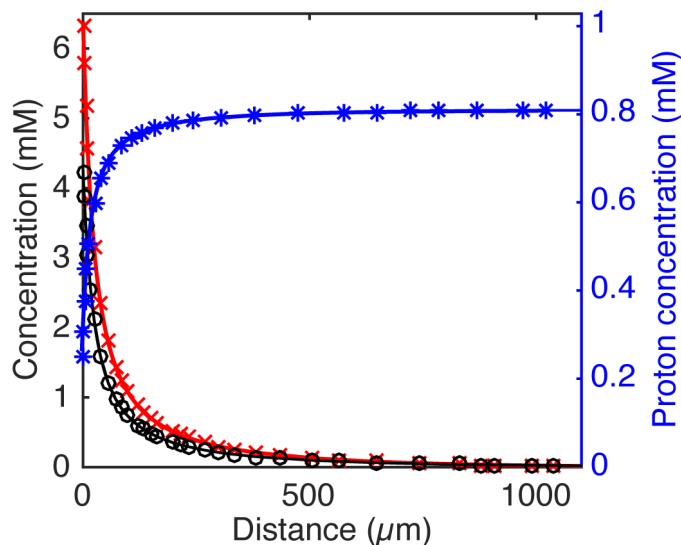
Figure 5.4. Concentration profiles of H^+ (blue), DIC (black) and Ca^{2+} (red) species during the dissolution of a rhombohedral calcite single microcrystal in aqueous solution at pH =3.1. Solid lines correspond to the results obtained from Model 1, where $J_i = J_{obs}$, and symbols correspond to the simulations from Model 2, for which $J_i = k_{surf} [H^+]_{surf}$, where k_{surf} = 6.4 ×10^{-4} m s^{-1}.

Hence, considering that the dissolution of calcite at pH < 4 is a heterogeneous reaction that depends on the concentration of protons at the crystal/solution interface (*vide supra*), k_{surf} can easily be determined solving eq. 5.5, where $J_i = J_{obs}$ and $[H^+]_{surf}$ is the interfacial proton concentration simulated in Model 1. Nevertheless, in order to explore surface fluxes and concentration profiles of the relevant species as a function of k_{surf} (Figure 5.5), and confirm the validity of first-order heterogeneous kinetics, a second model with the same geometry was employed. Model 2 simulated a series of surface fluxes described as $J_i = k_{surf} [H^+]_{surf}$, and k_{surf} was then evaluated to obtain the interfacial concentration and concentration profiles of species equivalent to those simulated in Model 1, accounting for the experimental dissolution rate and crystal geometry.[35] It can be seen from Figure 5.5, that k_{surf} = 6.4 ×10^{-5} m s^{-1} and 6.4 ×10^{-3} m s^{-1} approximate to the lower (surface kinetic control) and upper (diffusion-controlled) kinetic limits of this technique. The value of k_{surf} determined herein is 6.4 (± 2.8) ×10^{-4} m s^{-1} (Figure 5.4), in agreement with SECM experiments of single crystal faces, 6.3 (± 1.3) ×10^{-4} m s^{-1},[23] and similar to that from fast-flow hydrodynamic systems.[1, 21, 22]
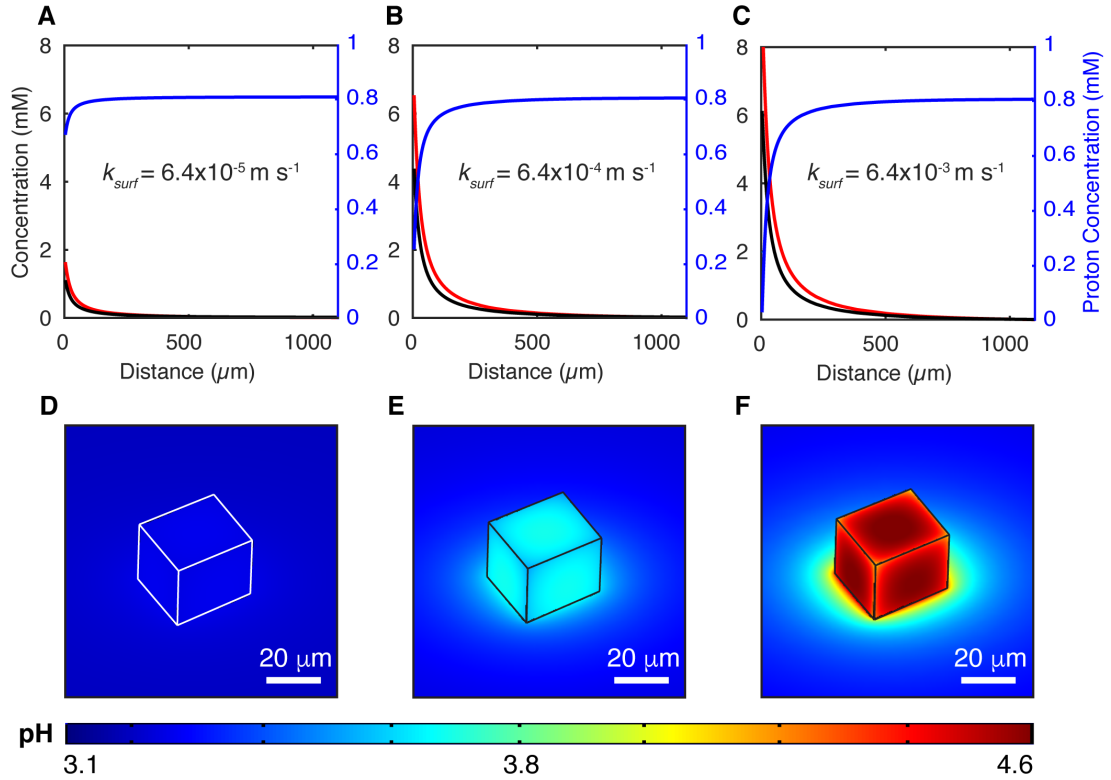
Figure 5.5. Concentration profiles of H^+ (blue), DIC (black) and Ca^{2+} (red) species and interfacial pH during the dissolution of a rhombohedral calcite single microcrystal in aqueous solution at pH =3.1 simulated for a surface flux, $J_i = k_{surf}[H^+]_{surf}$, where k_{surf} is (A, D) 6.4×10^{-5} m s^{-1}, (B, E) 6.4×10^{-4} m s^{-1} and (C, F) 6.4×10^{-3} m s^{-1}.

At steady-state, mass transport rates of reacting species diffusing towards or away from the crystal surface (eq. 5.9, where δ is the characteristic diffusion layer size) are necessarily equal to the surface reaction rate (eq. 5.10). This equality (eq. 5.11) is always true, independent of the kinetic regime, but the concentration of species near the crystal/solution interface and concentration profiles will depend on whether diffusion or surface reactions control the dissolution process.[45, 46]

$$J_{MT} = \frac{D}{\delta}([H^+]_{surf} - [H^+]_{bulk}) \qquad (5.9)$$

$$J_{SK} = k_{surf}[H^+]_{surf} \qquad (5.10)$$

$$J_{obs} = J_{MT} = J_{SK} = k_{surf}[H^+]_{surf} \qquad (5.11)$$

143

In eq. 5.9-5.11, J_{MT} is the transport flux, J_{SK} is the surface kinetic flux and J_{obs} is the experimentally observed (measured) flux. In the case of slow surface kinetic rates (small k_{surf}, larger contribution of surface kinetics to the dissolution process) the concentration of protons at the crystal/solution interface is close to that in bulk solutions (Figure 5.5D) and consequently the concentration gradient is small (Figure 5.5A). On the other hand, when the surface rates are fast (large k_{surf}) the concentration of protons at the crystal/solution interface is depleted significantly (Figure 5.5F) and approaches to zero,[4] so that the concentration gradient is steeper (Figure 5.5C). In an intermediate situation, (experimentally determined k_{surf}), the interfacial proton concentration acquires an intermediate value (Figure 5.5E), i.e. the kinetics is under mixed control and this should be used in models for the dissolution process in various applications highlighted earlier in the chapter.

4. Conclusions

The proton-promoted dissolution kinetics of rhombohedral calcite in aqueous solution has been investigated by optical microscopy coupled with numerical simulations. The experimental methodology, focused on monitoring the dissolution of isolated single microcrystal, enables the measurement of rapid surface processes via FEM models parameterized with experimental data. The simulations provide an accurate determination of the near-interface concentration of species during dissolution, as well as the intrinsic dissolution rate constant of the {104} faces.

In general, we have demonstrated that the approach described herein is an easy and versatile strategy to study the dissolution kinetics of entire single crystals. The methodology enables decoupling of mass transport and surface kinetic effects, such that the surface reaction rates can be measured for a system that is applicable to various natural systems and practical situations.

5.References

1.   R. G. Compton and P. R. Unwin, *Philos. Trans. R. Soc., A*, 1990, **330**, 1-45.

2.   J. W. Morse, R. S. Arvidson and A. Lüttge, *Chem. Rev.*, 2007, **107**, 342-381.

3.   R. S. Arvidson, I. E. Ertan, J. E. Amonette and A. Lüttge, *Geochim. Cosmochim. Acta*, 2003, **67**, 1623-1634.

4.   E. L. Sjoberg and D. T. Rickard, *Chem. Geol.*, 1984, **42**, 119-136.

5.   L. N. Plummer, T. M. L. Wigley and D. L. Parkhurst, *Am. J. Sci.*, 1978, **278**, 179-216.

6.   L. Chou, R. M. Garrels and R. Wollast, *Chem. Geol.*, 1989, **78**, 269-282.

7.   T. Arakaki and A. Mucci, *Aquat. Geochem.*, 1995, **1**, 105-130.

8.   M. Alkattan, E. H. Oelkers, J.-L. Dandurand and J. Schott, *Chem. Geol.*, 1998, **151**, 199-214.

9.   O. S. Pokrovsky, S. V. Golubev, J. Schott and A. Castillo, *Chem. Geol.*, 2009, **265**, 20-32.

10.   Z. Liu and W. Dreybrod, *Geochim. Cosmochim. Acta*, 1997, **61**, 2879-2889.

11.   C. N. Fredd and H. Scott Fogler, *Chem. Eng. Sci.*, 1998, **53**, 3863-3874.

12.   M. Alkattan, E. H. Oelkers, J.-L. Dandurand and J. Schott, *Chem. Geol.*, 2002, **190**, 291-302.

13.   E. Ruiz-Agudo, M. Kowacz, C. V. Putnis and A. Putnis, *Geochim. Cosmochim. Acta*, 2010, **74**, 1256-1267.

14.   G. Jordan and W. Rammensee, *Geochim. Cosmochim. Acta*, 1998, **62**, 941-947.

15.   Y. Liang, D. R. Baer, J. M. McCoy, J. E. Amonette and J. P. Lafemina, *Geochim. Cosmochim. Acta*, 1996, **60**, 4883-4887.

16.   C. E. Jones, P. R. Unwin and J. V. Macpherson, *ChemPhysChem*, 2003, **4**, 139-146.

17.   P. S. Dobson, L. A. Bindley, J. V. Macpherson and P. R. Unwin, *Langmuir*, 2005, **21**, 1255-1260.

18.   P. S. Dobson, L. A. Bindley, J. V. Macpherson and P. R. Unwin, *ChemPhysChem*, 2006, **7**, 1019-1021.

19.   K. Burns, Y.-T. Wu and C. S. Grant, *Langmuir*, 2003, **19**, 5669-5679.

20.   C. Peng, J. P. Crawshaw, G. C. Maitland and J. P. M. Trusler, *Chem. Geol.*, 2015, **403**, 74-85.

21.   R. G. Compton, K. L. Pritchard and P. R. Unwin, *Freshwater Biol.*, 1989, **22**, 285-288.

22.   B. A. Coles, R. G. Compton, J. Booth, Q. Hong and G. H. W. Sanders, *Chem. Commun.*, 1997, DOI: 10.1039/A608133I, 619-620.

23.   C.-A. McGeouch, M. Peruffo, M. A. Edwards, L. A. Bindley, R. A. Lazenby, M. M. Mbogoro, K. McKelvey and P. R. Unwin, *J. Phys. Chem. C*, 2012, **116**, 14892-14899.

24.   M. Adobes-Vidal, F. M. Maddar, D. Momotenko, L. P. Hughes, S. A. C. Wren, L. N. Poloni, M. D. Ward and P. R. Unwin, *Cryst. Growth Des.*, 2016, DOI: 10.1021/acs.cgd.6b00543, 4421-4429.

25.   A. R. Perry, M. Peruffo and P. R. Unwin, *Cryst. Growth Des.*, 2013, **13**, 614-622.

26.   M. Adobes-Vidal, A. G. Shtukenberg, M. D. Ward and P. R. Unwin, *Cryst. Growth Des.*, 2017, DOI: 10.1021/acs.cgd.6b01760.

27.   L. M. Mosley, P. Shand, P. Self and R. Fitzpatrick, *Appl. Geochem.*, 2014, **41**, 49-61.

28.   G. F. Fordham and C. T. Driscoll, *Can. J. Fish. Aquat. Sci.*, 1989, **46**, 306-314.

29.   Z. Amjad and P. G. Koutsoukos, *Desalination*, 2014, **335**, 55-63.

30.   A. A. Olajire, *J. Pet. Sci. Eng.*, 2015, **135**, 723-737.

31.   M. Crabtree, D. Eslinger, P. Fletcher, M. Miller, A. Johnson and G. King, *Oilfield Rev.*, 1999, **11**, 30-45.

32.   A. Morera-Chavarría, J. Griffioen and T. Behrends, *Chem. Geol.*, 2016, **443**, 146-157.

33.   A. Burgos-Cara, E. Ruiz-Agudo and C. Rodriguez-Navarro, *Mater. Des.*, 2017, **115**, 82-92.

34.   B. De Baere, S. Molins, K. U. Mayer and R. François, *Chem. Geol.*, 2016, **430**, 1-12.

35.   B. P. Nadappuram, K. McKelvey, R. Al Botros, A. W. Colburn and P. R. Unwin, *Anal. Chem.*, 2013, **85**, 8070-8074.

36.   *CRC Handbook of Chemistry and Physics*, CRC Press, Florida, US, 90th Edition (Internet Version 2010) edn., 2010.

37.   J. M. A. Grime, M. A. Edwards, N. C. Rudd and P. R. Unwin, *Proc. Natl. Acad. Sci. U. S. A.*, 2008, **105**, 14277-14282.

38. W. D. Schecher, *A Chemical Equilibrium Modelling System*, Hallowell, Maine, US, 2003.

39. F. M. Morel and J. G. Hering, *Principles and Applications of Aquatic Chemistry*, Wiley, New York, US, 1993.

40. W. Stumm and J. J. Morgan, *Aquatic Chemistry*, Wiley-Interscience, New York, UK, 3rd edn., 1996.

41. M. Takasaki, Y. Oaki and H. Imai, *CrystEngComm*, 2016, **18**, 8999-9002.

42. D. Aquilano, E. Costa, A. Genovese, F. Roberto Massaro, L. Pastero and M. Rubbo, *J. Cryst. Growth*, 2003, **247**, 516-522.

43. A. Lüttge, R. S. Arvidson and C. Fischer, *Elements*, 2013, **9**, 183-188.

44. J.-C. Chen, B. Reischl, P. Spijker, N. Holmberg, K. Laasonen and A. S. Foster, *Phys. Chem. Chem. Phys.*, 2014, **16**, 22545-22554.

45. A. C. Lasaga, *Kinetic Theory in the Earth Sciences*, Princeton University Press, 1998.

46. K. Sangwal, *Etching of Crystals: Theory, experiment, and application*, North-Holland Amsterdam, Amsterdam, NL, 1987.

Chapter VI | Conclusions

This thesis provides a detailed analysis of face-specific dissolution kinetics of single microcrystals using an innovative, yet simple, combination of microscopy techniques and FEM simulations. A key feature of the approach is the consideration of isolated crystals no larger than 50 μm across, in order to: (i) generate much higher diffusion rates than with any other technique available, including fast flow systems, thus allowing fast surface kinetics to be measured; (ii) maintain chemostatic control of the reaction conditions; (iii) simultaneously study all of the individual crystal faces and edges exposed to the solvent; and (iv) analyze interfacial fluxes and concentration distributions to elucidate the kinetic regime. Other advantages of this approach are that it does not require a flow system, supplementary sensors or additional ex-situ characterization of the crystal surface, and that the well-defined morphology of the microcrystal permits the rationalization of the results in terms of crystal structure and surface properties. In general, the approach presented in this thesis establishes a powerful and widely applicable method for studying dissolution processes; one that is demonstrated and validated with studies of a variety of different crystal structures herein.

Chapter II presented the first study of real-time dissolution kinetics at all of the individual faces of single crystals. An *in situ* multimicroscopy approach, in which SICM and optical microscopy are combined with FEM modeling to study dissolution processes, is described. The experimental approach allowed 3D visualization of crystal morphology during dissolution, from which a numerical model was developed to calculate the concentration distribution around the crystal, as well as the dissolution flux of solute molecules at the solid/liquid interface. This allowed the quantitative comparison of mass transport and surface kinetics. Results show that the (001) face of furosemide crystals is strongly influenced by surface kinetics and presents a mixed kinetic control, while the (010) and ($10\bar{1}$) faces are dominated by mass transport. However, dissolution rates were found to vary considerably from crystal to crystal and were time dependent at large dissolution times. This is due to the impact of a number of factors, including subtle effects from the size, shape, and apparent number

of defects (etch pits) in a particular crystal, as shown by complementary *ex situ* AFM measurements of partially dissolved microcrystals.

Informed by the results in chapter II, the impact of surface topography on dissolution kinetics was studied in more detail in chapter III. It was shown that *in situ* AFM can be used to visualize changes in the crystal morphology during dissolution, also allowing the surface processes that accompany dissolution to be monitored in real-time. Similar to the furosemide crystals studied in chapter II, different bicalutamide crystal faces exhibit different dissolution rates. Dissolution involves roughening and pit formation on all dissolving surfaces, and this has a strong influence on the overall dissolution rate. By incorporating AFM experimental data into four different steady state FEM models, each simulating the dissolution of the microcrystal at different dissolution times, it was possible to determine the relative contributions of surface kinetics and mass transport for each crystal face during the dissolution time-course. Simulations showed that the dissolution kinetics of all crystal faces are largely surface-kinetics-controlled, but the mass transport contribution increased as dissolution proceeded. This was attributed to the formation of microdomains of higher surface energy (higher dissolution rate constant, k_{int}) during surface pitting, though this value was not quantified.

The quantification of interfacial kinetics, and the intrinsic dissolution rate constant, k_{int} as a function of the crystal morphology during the dissolution time-course was addressed in chapter IV. Using the *in situ* multimicroscopy approach introduced in chapter II, the dissolution rates of the $\{0001\}$ and $\{10\bar{1}0\}$ faces of L-cystine crystals were determined. The experimental data allowed the elucidation of interfacial concentrations and concentration gradients, as well as the separation of kinetic and mass transport limiting regimes using FEM simulations, which in turn permitted the determination of k_{int}. Results revealed that k_{int} increased as the L-cystine crystal dissolved, concomitant with the reduction in crystal size and the formation of high index crystal faces, significantly impacting the kinetic regime and causing a change from a surface-kinetics-controlled dissolution to a mixed regime.

Chapter IV also described the investigation of the dissolution mechanism of the $\{0001\}$ surface of hexagonal L-cystine macrocrystals by *in situ* AFM in a flow cell system. The visualization of hexagonal spirals emerging from screw dislocations on

the {0001} face permitted the measurement of the dependence of step velocities on L-cystine concentration, from which kinetic information could be derived. Kinetic data obtained from OM-SICM and AFM, which provide alternative methods of measuring kinetics, were in good agreement when the different mass transport regimes of the two experimental configurations are accounted for. Collectively, these results suggest a roadmap for the quantitative analysis of single crystal dissolution across multiple lengthscales.

All of the crystals studied in the first three chapters were characterized by relatively slow or very slow dissolution rates, allowing the use of scanning probe microscopy to probe the dissolution. Chapter V aimed to prove that the approach developed in this thesis was also suitable for studying fast dissolution kinetics. Most techniques have shown that proton-promoted calcite dissolution rates are controlled by the diffusion of protons to the surface. The process is so fast that measuring the intrinsic surface dissolution kinetics has proved challenging, with only a few techniques having been able to measure the intrinsic dissolution rate constant of calcite in acid water. In this chapter, the investigation of the proton-promoted dissolution kinetics of rhombohedral calcite in aqueous solution, using optical microscopy coupled with numerical simulations, was described. The simulations allowed the accurate determination of the near-interface concentration of species during dissolution, as well as the intrinsic dissolution rate constant of the {104} faces, showing that surface kinetics play an important role in the dissolution of microcrystals.

In summary, the work presented in this thesis provides a significant advance in the analysis and understanding of crystal dissolution, with quantitative results that are consistent across different techniques from the nanoscale to macroscale. The proposed approach is widely applicable to a range of crystal types, encompassing organic and ionic crystals (see Appendix for a guide of the most adequate experimental approach depending on the crystal characteristics). The approach is attractive not only for the methodological reasons outlined at the start of this chapter, but also in revealing differences between different crystals in a population, which remain hidden in ensemble measurements. In this manner, the work herein expands the current growing trend in the physical sciences towards single entity measurements, which are valuable in revealing the distribution of activity in reactive systems.

Appendix

Guide for the selection of the most adequate experimental approach to study face-specific dissolution kinetics of single crystals

Objectives	Crystal dimensions	Dissolution time (min)	Imaging technique	Comments
Microscale:				
Dissolution kinetics of the individual crystal faces exposed to the solvent simultaneously	$d < \delta$ *	30 - 60	OM-SICM	• Optimize the number of hops per line scan in the SICM system (≥ 10).
			OM (If all crystal faces are equivalent)	• An initial measurement of the crystal height can be done by adjusting the focus of the OM, or more accurately by SICM.
		≥ 120	*In situ* AFM in quiescent solution	• Image the entire crystal. • Use of TM-AFM to minimize tip-crystal interactions.
Nanoscale:				
Dissolution kinetics and mechanism of a particular crystal face	>200 μm	≥ 120	*In situ* AFM in flow cell	• Crystal must be big enough to allow imaging during at least a couple of hours and a few regions have to be imaged to be sure the obtained data are representative of the entire face. • Optimize flow rate (v_{step} = constant) and scan rate (v_{step} can be measured). • Need for analysis of mass transport inside the cell.

* The crystal largest dimension (d) must be smaller than the diffusion layer thickness (δ), generally $d \leq 50$ μm. The diffusion layer thickness depends on the crystal size and the diffusion coefficient of the solute in the solvent (D).